ABSTRACT

EFFECTS OF IMPLANTATION OF DECABORANE IONS IN SILICON

by
Cheng Li

The next generations of Si microelectronic devices will require ultra shallow *p*-type junctions formed by implantation of B ions with energies below 1 keV, at which available beam currents are severely limited by space charge effects. To solve this problem, decaborane ($B_{10}H_{14}$) cluster ion implantation has been suggested as an attractive alternative to conventional B implants, because one decaborane ion implants ten B atoms simultaneously and each of the B atoms only carries approximately 1/11 of the total ion energy. Thus the same implantation depth and dose as with monomer B ions can be obtained using decaborane ions but with 10 times less charge and ten times higher energy. In this dissertation research, various effects of implantation of decaborane cluster ions in silicon were studied, using an experimental ion implanter in the Ion Beam and Thin Film Research Laboratory at NJIT.

Secondary Ion Mass Spectrometry (SIMS) depth profiles of boron and hydrogen in decaborane-implanted samples were measured before and after thermal activation annealing and compared to that in the control samples. Shallow p-type junction could be achieved with decaborane implantation. The co-implanted hydrogen diffused out almost entirely after annealing and hence is expected to have a negligible effect on the device performance.

Transient enhanced diffusion (TED) of B atoms in Si implanted with mass analyzed decaborane ions of three energies were measured and compared to that of B atoms in Si implanted with B^+ ions of equivalent B energy and dose. The results

demonstrated that implantation of B with decaborane cluster ions led to essentially the same amount of TED of B in Si as that in Si implanted with atomic B^+ ions of the equivalent energy and dose.

The sputtering yields of Si with B in the form of decaborane clusters were measured and compared to those for boron monomer ions, estimated using an empirical formula. The surface morphology of amorphous Si, crystalline Si and Ta film irradiated with energetic decaborane ions and argon ions were studied using Atomic Force Microscopy (AFM). Results of surface roughness and Power Spectral Density (PSD) analysis show that decaborane cluster ions smooth rather than roughen these surfaces.

Molecular Dynamics (MD) simulations have been performed to compare impact effects on Si target by B monomers and B_{10} clusters at the same energy per B atom. B depth profiles were found to be similar for B atoms implanted with B_{10} clusters and with B monomers. The crater formation, a unique feature of cluster impacts, was also observed on the Si surface impacted by a B_{10} cluster. The calculated sputtering yield of Si (the number of ejected Si atoms per incident B) was much larger with B_{10} clusters than with B monomers and also larger than the experimental values.

The results of this research confirm that decaborane implantation is a viable alternative to low energy B implantation for ultra shallow *p*-type junction formation. These results also contribute to the knowledge base of the technology of ultra shallow B doping in CMOS devices and will help to better understand cluster-solid interactions in general.

EFFECTS OF IMPLANTATION OF DECABORANE IONS IN SILICON

by
Cheng Li

A Dissertation
Submitted to the Faculty of
New Jersey Institute of Technology
in Partial Fulfillment of the Requirements for the Degree of
Doctor of Philosophy in Materials Science and Engineering

Interdisciplinary Program in Materials Science and Engineering

May 2003

APPROVAL PAGE

EFFECTS OF IMPLANTATION OF DECABORANE IONS IN SILICON

Cheng Li

Dr. Marek Sosnowski, Dissertation Advisor — Date
Associate Professor of Electrical and Computer Engineering, NJIT

Dr. Ken K. Chin, Committee Member — Date
Professor of Physics and Acting Director for Materials Science and Engineering Program, NJIT

Dr. Haim Grebel, Committee Member — Date
Professor of Electrical and Computer Engineering and Director for Electronic Imaging Center, NJIT

Dr. James K. Hirvonen, Committee Member — Date
U.S. Army Research Laboratory, Aberdeen, MD

Dr. Hans-Joachim L. Gossmann — Date
Axcelis Technologies, Beverly, MA

BIOGRAPHIC SKETCH

Author: Cheng Li

Degree: Doctor of Philosophy

Date: May 2003

Undergraduate and Graduate Education:

- Doctor of Philosophy in Materials Science and Engineering,
  New Jersey Institute of Technology, Newark, NJ, 2003
- Master of Science in Materials Science,
  Research Institute of Physical and Chemical Engineering of Nuclear Industry, Tianjin, P. R. China, 1990
- Bachelor of Science in Metallic Materials,
  Tianjin University, Tianjin, P. R. China, 1987

Major: Materials Science and Engineering

Presentations and Publications:

Cheng Li, Leszek Gladczuk, and Marek Sosnowski, "Characteristics of ultra shallow B implantation with decaborane", *Mat. Res. Soc. Symp. Proc.* Vol.745, N.6.3.1-N6.3.6, 2003.

Cheng Li, Leszek Gladezuk, Maria A. Albano, Marek Sosnowski, Hans-Joachim L. Gossmann, and Dale C. Jacobson, "Sputtering of Si with decaborane cluster ions", Presented at the 14th International Conference on Ion Implantation Technology, Taos, New Mexico, September 2002.

Marek Sosnowski, Maria A. Albano, Cheng Li, Hans-Joachim L. Gossmann, and Dale C. Jacobson, "Transient enhanced diffusion of B in Si implanted with decaborane cluster ions", *Journal of the Electrochemical Society* Vol.149, pp. G474-G476, June 2002.

Marek Sosnowski, Maria A. Albano, Cheng Li, Hans-Joachim L. Gossmann, and Dale C. Jacobson, "Sputtering of Si with decaborane cluster ions", *Applied Physics Letters* Vol.80, pp. 592-594, February 2002.

This dissertation is dedicated

To my beloved dad in heaven

To my lovely wife and daughter
for their love, support and encouragement

To all my family members

ACKNOWLEDGMENT

I would like to express my sincere gratitude to my dissertation advisor, Dr. Marek Sosnowski, for his constant direction, encouragement and support throughout the course of this work. Special thanks are extended to Dr. Hans-Joachim L. Gossmann who not only served as a committee member, but also helped with Si/C/Si sample preparation and TED sample and data analysis, to Dr. James K. Hirvonen for serving as a committee member and for the help on the RBS measurements. Furthermore, I wish to thank Dr. Ken K. Chin and Dr. Haim Grebel for serving as committee members.

Equipment donations from Axcelis and a decaborane delivery source from ATMI for the experimental implanter at NJIT are appreciated. This research was made possible by support from the National Science Foundation (GOALI program), the International Sematech, and the Semiconductor Research Corporation.

I wish to acknowledge Dr. Dale C. Jacobson for performing the NRA and the RBS measurements, Dr. Tony Fiory for assisting with the annealing of the samples, Dr. John Demaree for the RBS measurements at the Army Research Lab, Dr. Serguei Savrassov for providing computing facilities at NJIT, Christopher Santeufemio and Gene Degenkolb of Epion Corporation for helpful discussions and facilitating AFM measurements performed at Epion. Special thanks are extended to Dr. Zinetulla Insepov for his instruction and help on MD simulations. I would like to extend my special gratitude to Maria A. Albano for her great help in the research. I would also like to extend special thanks to my colleagues in the Ion Beam and Thin Film Research Laboratory for their encouragement and friendship: Leszek Gladczuk, Anamika Patel, Younes Abbassi, Chanranjee Sigh Paurl, Chirag A. Joshi, and Wenwen Luo.

TABLE OF CONTENTS

TABLE OF CONTENTS
(Continued)

TABLE OF CONTENTS
(Continued)

TABLE OF CONTENTS
(Continued)

Chapter **Page**

LIST OF TABLES

LIST OF FIGURES

LIST OF FIGURES
(Continued)

LIST OF FIGURES
(Continued)

LIST OF FIGURES
(Continued)

LIST OF FIGURES
(Continued)

LIST OF FIGURES
(Continued)

LIST OF FIGURES
(Continued)

CHAPTER 1

INTRODUCTION

1.1 Background

1.1.1 Challenges for Ultra Shallow Ion Implantation

Performance and speed of ULSI microelectronic circuit devices are improved by continuously scaling down device dimensions. As the size of the MOSFET transistor gate electrode is reduced, shrinking is needed of both the vertical and lateral dimensions of the doped regions in the Si substrate. For deep sub-micron MOSFET structures of high performance, formation of ultra shallow doped source/drain (S/D) extensions next to the gate is essential to obtain a high drive current and to suppress the short-channel effects, which cause excessive leakage current when the gate length becomes small. The 1999 Edition of the International Technology Roadmap for Semiconductors (ITRS) predicts the need for 20 ~ 33 nm deep junctions in the 0.1 μm line-width CMOS devices expected by the year 2005 [1]. The actual pace of scaling is even faster than predicted and a more rigorous requirement is projected especially for *p*-type drain extension junctions according to the latest ITRS roadmap [2] (See Table 1.1). Higher junction abruptness and lower sheet resistance as well as ultra-low thermal budgets are also required.

In the mass production of Si ULSI devices, ion implantation technology is currently the most widely used method for doping of Si, since the dopant dose and depth profile can be precisely and independently controlled and reproduced and the purity of implanted species can be ensured by mass separation [3].

Table 1.1 2001 ITRS Front-End Processes Roadmap (Selected Data) [2]

	Near-term			Long-term		
Year of Production	2002	2005	2007	2010	2013	2016
Technology node (nm)	115	80	65	45	32	22
MPU physical gate length (nm)	53	32	25	18	13	9
Wafer diameter (mm)	300	300	300	300	300	450
Tox (gate oxide thickness) for MPU/ASIC (nm)	1.2-1.5	*0.8-1.3*	*0.6-1.1*	*0.5-0.8*	*0.4-0.6*	*0.4-0.5*
Contact Xj (nm)	39-78	24-47	**18-37**	*13-26*	*10-19*	*7-13*
Contact Maximum resistivity $(\Omega\text{-cm}^2)$	3.20 E-07	**1.80 E-07**	*1.10 E-07*	*6.40 E-08*	*3.80 E-08*	*2.40 E-08*
Drain Extension Xj (nm)	22-36	*13-22*	*10-17*	*7-12*	*5-9*	*4-6*
Maximum drain extension Rs (PMOS) (Ω/sq))	460.0	770.0	760.0	*830.0*	*940.0*	*1210.0*
Extension lateral abruptness (nm/decade)	5.8	**3.5**	**2.8**	*2.0*	*1.4*	*1.0*

10	Solutions are known
10	Solutions exist and are being optimized
10	Solutions are NOT known

In the deep sub-micron regime, however, it is difficult to achieve very shallow junctions by conventional implantation technology, especially in *p*MOSFETs, in which source and drain junctions are formed by implantation of boron ions. Compared to heavier phosphorus and arsenic atoms of the same energy, light boron ions are implanted much deeper, and they also easily diffuse into the Si substrate during activation annealing. In order to produce ultra shallow *p*-type junctions, the energy of boron ions must be in the sub-keV range. At such low energies, the maximum obtainable beam current is severely limited due to space charge effects during extraction from an ion source and due to the beam expansion by the repulsive forces between ions during beam transport. Thus, the throughput is too low to meet ever increasing industry requirements.

Considerable effort has been made to extend the traditional ion implantation technology to the regime of shallow junction formation. Germanium pre-amorphization processing before actual B implantation could minimize ion projected range and eliminate ion channeling for implants above 0.5 keV [4]. Electrostatic deceleration of high energy ions in front of the target may be utilized to overcome the beam transport difficulty [5]. The Applied Materials xRLEAP ion implantation system has deceleration giving a final energy range of 0.2 to 80 keV [6]. However, in this technique a fraction of high energy ions may be neutralized before deceleration, causing the so-called "energy contamination", which results in deeper junctions.

In the Varian VIISta–810 system, the beam space charge is reduced by the use of a stationary ribbon ion beam with a single wafer mechanically scanned across the rectangular beam in one direction, perpendicular to the long axis of the beam [7]. The complexity of the ion optics of a ribbon beam implanter requires added tuning time and thus may reduce the throughput.

Recent Axcelis GSD Ultra and HC3 ULTRA high-current implanters were able to implant ions at energies as low as 0.2 keV by using unique source and extraction designs and a shortened beamline [8].

1.1.2 Other Shallow Doping Techniques

In addition to ion implantation, other techniques have been explored as possible solutions to solve the problem of achieving very shallow doping.

One solution is Plasma Immersion Ion Implantation (PIII) [9], in which the wafer is surrounded by the plasma containing the dopant ions, and implantation occurs when a pulse of negative bias is applied to the wafer holder, as shown in Figure 1.1. The most important advantage of PIII is that very low energy (around 50 eV or above) implantation can be done with very high current. Although PIII implant currents are also determined by the same Child-Langmuir law as that drawn from a conventional ion source, it does not experience the high loss of low energy ions in the beamline due to space charge effect. The total ion current in the PIII system is very close to the theoretical limit. The main disadvantages of PIII are wafer heating, difficult dose control, and uncertain dopant purity since there is no energy / mass analysis.

Another solution is Projection Gas Immersion Laser Doping (P-GILD) [10]. In the current P-GILD system, as schematically shown in Figure 1.2, the wafer is immersed in a dopant gas ambience and doping is achieved through liquid-phase diffusion. Initially, an ArF laser is used to induce deposition of dopants over the entire laser-exposed area. Then, a XeCl laser drives the deposited dopants into the substrate by melting it to a shallow depth. The second laser beam is scanned across a dielectric reticle that patterns the beam before it reaches the wafer surface. No subsequent annealing step is required, since the rapid regrowth of the melted Si layer occurs epitaxially, incorporating dopants into electrically active substitutional sites. The total heat cycle is on the order of nanoseconds. It can form shallow junctions with box-shaped depth profiles and acceptable activation levels.

Another technique is based on deposition of B-doped SiGe films. SiGe epitaxial layers exhibit a higher solid solubility of boron and a higher electron and hole mobility, as compared to Si. *In-situ* B-doped SiGe can be selectively deposited at low temperature (500~600°C) in the source/drain regions in order to realize ultra shallow p^+-n heterojunctions with low sheet resistance [11]. Since dopant atoms are highly activated during film deposition, no subsequent annealing is needed. However, an etching step is required to etch the deposited layer to the desired junction depth.

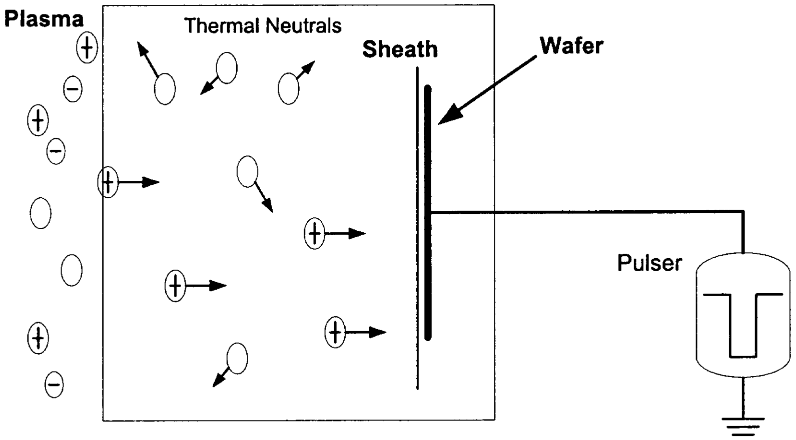

Figure 1.1 A schematic of the Plasma Immersion Ion Implantation process [9].

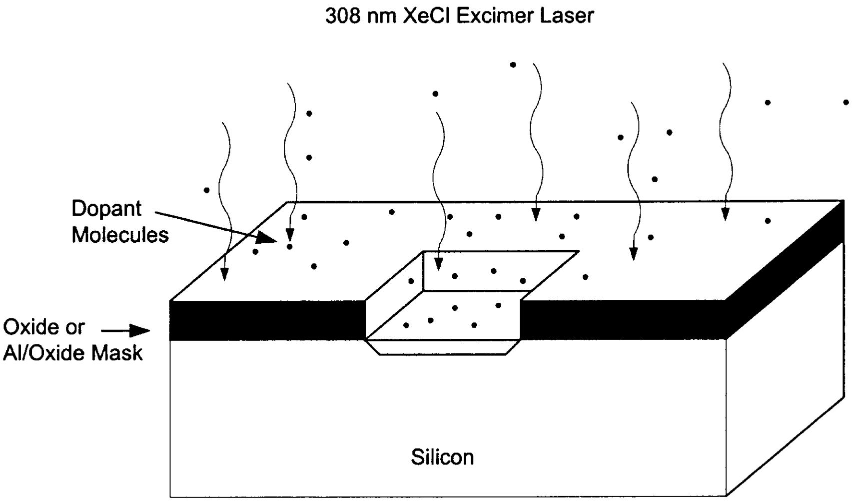

Figure 1.2 A sketch of the Projection Gas Immersion Laser Doping (P-GILD) System [9].

1.1.3 Decaborane Implantation as an Alternative Solution

An alternative approach to form shallow junctions is to employ ion implantation with polyatomic or cluster ions, where energy is partitioned between the atoms of a cluster in direct proportion to their mass. For example, BF_2^+ has been extensively used for *p* doping in the industry since B atom represent only about 1/5 of the ion mass and its energy is thus about 1/5 of the energy of the ion beam. However, the co-implanted fluorine in the poly-Si gate will enhance the boron diffusion through the gate oxide, resulting in fluctuation of the threshold voltage V_T [12].

The decaborane ($B_{10}H_{14}$) cluster is a more attractive candidate because of its larger number of B atoms per cluster. As shown in Figure 1.3, a decaborane molecule consists of 10 boron atoms and 14 hydrogen atoms. The molecular weight of a decaborane cluster (122 AMU) is approximately 11 times that of a boron atom. Since each of the B atoms in the cluster carries only approximately 1/11th of the total cluster kinetic energy, decaborane can be implanted at an acceleration voltage about 11 times higher than that of B^+ for equivalent B projected range. The maximum beam current density that can possibly expected for any charged particles accelerated by an electric field under space-charge limited conditions follows the Child-Langmuir law [13]:

$$J = \frac{4\sqrt{2e\epsilon_0}}{9d^2} \frac{(V_a)^{3/2}}{(m)^{1/2}} \tag{1.1}$$

where V_a is the acceleration voltage, m is the ion mass, e is the charge of the ion, and d is the distance from the edge of the plasma to the extraction electrode.

Since both the acceleration voltage and mass of $B_{10}H_{14}^+$ are 11 times that of B^+, the current density from $B_{10}H_{14}$ beam is 11 times larger. Also, considering that one decaborane cluster delivers 10 boron atoms to the target, the dose rate with decaborane ions is:

$$\phi_{B_{10}H_x^+} = 110 \times \phi_{B^+} \tag{1.2}$$

Theoretically, implantation with decaborane ions gives rise to approximately 110 times higher throughput than with monomer B ions. In practice, this number is somewhat lower as some hydrogen atoms are lost in the ionization process.

In earlier research at NJIT, performed in collaboration with Bell Laboratories, it was shown that decaborane is suitable as an ion source material [14]. Decaborane implantation may be incorporated into the current CMOS fabrication process without need for major changes to the implanter design. Extensive studies have been performed in recent years to evaluate the feasibility of decaborane for ultra shallow *p*-type junction formation and the work reported in this dissertation makes contributions to this effort.

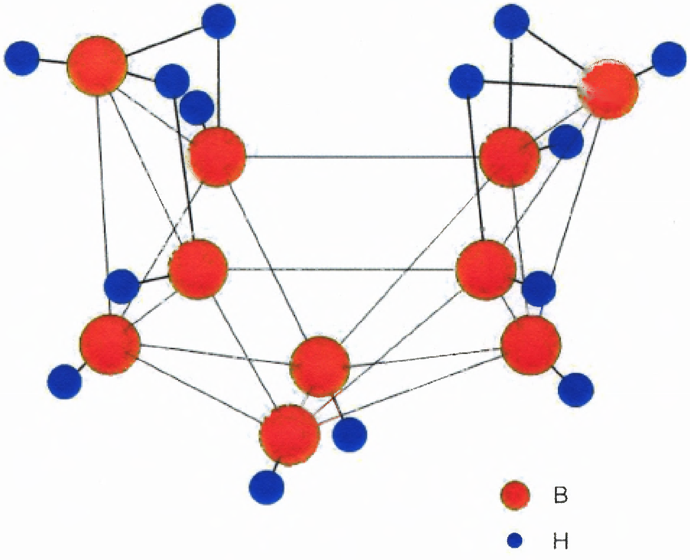

Figure 1.3 Structure of a decaborane molecule consisting of 10 boron atoms and 14 hydrogen atoms. The boron atoms are covalently bonded with a hydrogen atom bonded to each of them. The remaining four hydrogen atoms form single-atom bridges between four pairs of boron atoms.

1.2 Previous Study on Decaborane Implantation

1.2.1 Ultra Shallow p^+-n Junction Formation

Application of decaborane cluster ions for ultra-shallow *p*-type junction formation was first time demonstrated in 1996 by Fujitsu Corporation in collaboration with Kyoto University [15]. The experimental apparatus was originally designed for surface modification with large cluster ions, generated by adiabatic gas expansion through a very small nozzle into vacuum. In order to perform decaborane implantation experiments, the nozzle was removed (See Figure 1.4). Decaborane molecules in a low-pressure vapor were ionized by electron impact and the ionized species were then accelerated toward Si wafers without any mass selection. PMOSFETs of 0.15 μm line-width were fabricated with 34 nm shallow Source/Drain extensions by using 5 keV $B_{10}H_{14}^+$ implantation and 10 seconds rapid thermal annealing (RTA) at 1000°C. In the following year, the same group fabricated a 50 nm PMOSFET having 7 nm junction depth by 2 keV $B_{10}H_{14}^+$ implantation and using a 2-step activation annealing [16]. The fabricated device demonstrated very attractive electric performances such as a high drive current of 0.40 mA/um (at Ioff = 1 na/um and Vd = -1.8 V) and a low S/D series resistance (760 ohm-cm). It was also claimed in these studies that boron transient enhanced diffusion (TED) was suppressed. However, the ion beam was not mass analyzed and the exact implanted species were not known.

Great interest has been aroused in the study of decaborane implantation in the following years. Both experiments and computer simulations have been performed to investigate various aspects of decaborane implantation technology, which are described in the following sections.

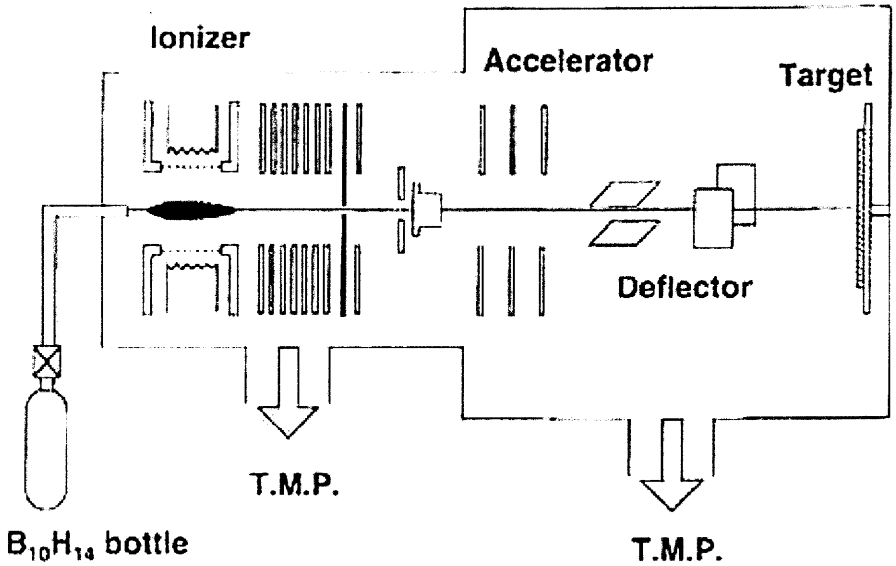

Figure 1.4 Cluster ion impact apparatus modified for decaborane implantation at Kyoto University, Japan [25]

1.2.2 Ionization Properties of Decaborane and Ion Source Design

To evaluate the feasibility of using decaborane as an ion source material for boron implantation, the ionization and breakup properties of decaborane molecules subjected to energetic electron bombardment were studied. Sosnowski *et al.* [14, 17] measured the mass spectra of decaborane ions generated by the impact of electrons in the energy range from 25 to 250 eV and source temperatures up to 350°C, using a quadrupole mass spectrometer. It was found that cluster ions containing 10 B atoms were the predominant component in the ion mass spectra (70~95%), even at elevated temperature (250 ~ 350°C). The data showed that B clusters were more stable than might have been expected, which was promising for the prospect of using decaborane in ion sources for shallow boron implantation. Subsequently, the results were confirmed using a research ion implanter built at NJIT with an electron impact ionization source.

Foad *et al.* pointed out that, the fragile decaborane molecules would not survive in a conventional hot cathode ion source where the temperature is typically up to 1000°C [18]. A suitable high current decaborane ion source is critical to the commercialization of decaborane implantation. Perel *et al.* at Axcelis Technologies reported on the design of an ion source capable of ionizing decaborane without significant fragmentation and generating low energy beam currents that were competitive with available high current ion implanters [19]. The ion source design was based on modification of an existing ion source by maintaining a source temperature below 300°C. Independently, Vella *et al.* reported on a 2.3 mA decaborane beam current at 50 kV on a high-current implanter using an ion source modified from a Bernas-type ion source [20].

Axcelis Technologies announced an industry first by integrating their patented decaborane source technology with a conventional ion implantation system and successfully implanting device wafers in collaboration with Agere Systems (formally Lucent Technologies). The performance data of commercially manufactured devices and those made with decaborane source and drain implants showed identical characteristic [19, 21], as described in section 1.2.3.

Sources that produce negative decaborane ions have also been demonstrated. A new style of ion source was recently presented by SemiEquip Inc. (Billerica, MA) that generates production worthy beam currents of As^+ and P^+ as well as decaborane ions [22]. Researchers at University of Houston investigated the delivery of B-containing cluster ions using a source of negative ions by cesium sputtering [23].

1.2.3 Physical Effects of Implanted Decaborane Ions

Dirks *et al.* [24] at Philips Research Labs compared the effects of implantation of Si with decaborane ions and with B^+ ions over a wide range of equivalent energies, using a high-voltage research implanter with a microwave ion source. The results showed that the effects of decaborane ions, such as B depth profile, were essentially the same as those of monomer B^+ ions except for larger crystal damage in Si implanted with decaborane. This is in agreement with an earlier investigation in which it was demonstrated that B SIMS profiles in Si implanted with 20 keV decaborane ions was quite similar to that from 2 keV B implants [25]. Although high energy (440keV) decaborane implantation results in hydrogen incorporation in Si, no hydrogen was detected by Secondary Ion Mass Spectrometry (SIMS) after RTA at temperature of 800°C or above. The lowest implant energy (2.8 keV) results in a damage depth of ~2 nm as calculated from the as-implanted RBS spectra. After low energy (2.8 keV) decaborane implantation, there is still significant TED during a 10s 950°C anneal, but it was not detected at higher annealing temperatures of 1000 and 1050°C.

To verify the claim of reduced TED by decaborane implantation [16, 26], Agarwal *et al.* quantified and compared the TED from implantation of decaborane cluster ions and B monomer ions of equivalent energy and dose [27]. Samples with embedded boron marker layers were implanted with 5 keV $B_{10}H_{14}$ and 0.5 keV B ions to equivalent boron dose ($1x10^{15}$ B/cm^2). Decaborane implantations were performed on the Kyoto University apparatus. An unimplanted sample was also included as a control. Boron depth profiles were analyzed on all samples by SIMS before and after annealing at 950 for 30s. The boron diffusivity enhancements were extracted based on the spreading of the marker layers using the method described in [28]. Comparable enhancements were observed for both ions, consistent with the "+1" model [29]. Since the ion beam used in these experiments likely contained various species, TED measurements were repeated with mass analyzed decaborane beams as part of the current work.

At low energy implantation, the phenomenon of dopant self-sputtering is of much concern since it causes loss of implanted species and may limit the highest obtainable boron dose in Si wafers. Retained B dose in Si samples implanted with decaborane ions was measured by Nuclear Reaction Analysis and compared with the dose calculated from the integrated ion beam current [30, 31]. It was observed that the boron loss increased with increasing nominal dose and the retained dose tended to saturate at higher dose level, a behavior characteristic of sputter limited implantation. For a given nominal dose, more boron atoms were retained at higher cluster ion energy. In addition, comparison with similar results after B^+ implantation of equivalent energy showed that decaborane implants might have higher implantation efficiency (retained dose ratio) than the monomers.

To ascertain the feasibility of decaborane ions for device manufacturing, a split lot production test was performed on a Lucent standard 0.16 μm technology process [30]. Some wafers were processed with the standard source/drain extension implant (6 keV BF_2, $\sim 5\times 10^{14}/cm^2$), while others were subjected to the equivalent $B_{10}H_{14}$ implant (15 keV, $\sim 5 \times 10^{13}/cm^2$). All other process steps were the same on the test MOS transistors. The electrical characteristics measured on test MOS transistors fabricated using implantation with decaborane ions and B^+ ions of equivalent energy were found to be identical. Another series of tests was carried out on short-channel p-MOSFETs fabricated at MIT [19]. Both decaborane implants (5.6 keV, $5\times10^{13}/cm^2$) and conventional boron implants (^{11}B 0.5 keV, $5\times10^{14}/cm^2$) were used for the shallow source and drain extensions. Conventional ^{11}B (2 keV, $5 \times 10^{13}/cm^2$) was used for the deep source and drains and for doping of the gates. The mask sequence was modified so that both decaborane and conventional boron devices were fabricated on the same wafer, with all other process steps being common. The differences in B depth profiles from decaborane and ^{11}B implants into 200 mm crystalline wafers were within the uncertainty of the SIMS measurements indicating that the two implants are equivalent. The characteristic data indicated that the devices were performing equally well both with the decaborane and ^{11}B shallow source and drain. Low off-currents and reasonable sub-threshold slopes (<85 mV/decade) were observed.

1.2.4 Computer Simulations

Computer simulations can predict the results of ion implantation and help to better understand the physical processes involved in the ion-solid interactions. The TRIM program, a binary collision Monte Carlo approach, has been successful in predicting the stopping range, damage production and even sputtering associated with atomic ion impacts [32]. However, the binary collision approximation breaks down at very low ion energy when the ion mean-free-path approaches the average atomic spacing in the target [33]. Since decaborane cluster ions are intended for ultra shallow junction formation, their impacts involve low energy atomic collisions. In addition, cluster ion impact means simultaneous striking of many projectiles at a local region of the substrate, while in a TRIM simulation only one projectile and one target atom are considered in one collision event. Therefore, the TRIM program built on binary collision model is not suitable to fully describe the decaborane implantation process. Molecular Dynamics (MD) simulation, which solves equations of motion for many particles of both the projectile and the target, is more suitable for studying the physics in cluster-solid interactions.

Smith *et al.* studied the irradiation effect on Si surface from decaborane cluster at 1, 2 and 4 keV by means of MD simulations up to 7 ps [34]. The implantation profiles of B atoms, the whereabouts of the H from the impacted molecule and the damage to the lattice were investigated. The simulation showed that if a small binding energy of the B atom in the Si lattice was assumed then most of the B from the cluster was implanted.

Insepov *et al.* carried out simulations for the cluster energy from 3.5 keV to 15 keV. The results revealed the formation of a large amorphized area in a subsurface region, which is a major difference between monomer B and decaborane ion implantation

[35, 36]. The computed sputtering yield of Si was found to increase with cluster energy and agreed well with the experimental value for 12 keV decaborane. Boron monomers and small clusters (B_4 and B_{10}) of the equivalent incident energy (230 eV/atom) showed similar implant depth and efficiency, but different damage structure [37].

1.3 Previous Research Results on Cluster Ion Impacts

The phenomena of solid impact by other cluster ions have been extensively studied in recent years. Various cluster ion – target combinations have been investigated in the following effects

- Sputtering and sputter yield
- Surface damage or defect production
- Effects on surface morphology
- Modification of other properties
- Other potential applications such as etching, thin film deposition, etc.

M. Dobeli *et al.* [38] studied the irradiation of single crystal Si with Au_n cluster at energies of 6 keV/atom (n=1…5) or 10 keV/atom (n=1,2,3). The number of surface defects caused by cluster bombardment was measured by Thermal Wave Analysis (TWA). In a TWA measurement, the propagation of the charge carriers and the temperature field produced by an amplitude-modulated focused laser beam was influenced by the defect density in the sample. By measuring the modulated reflectivity, which depends on the local temperature and charge carrier concentration, the defect concentration in the sample surface could be obtained. No obvious dependence of the defect concentration on cluster size *n* can be observed. For sputtering yield analysis, squares of 6 μm x 6 μm were irradiated at 10 keV/atom (n =1, 2, 3) to 5×10^{17} atoms/cm^2. The sputtered depths were then measured by Atomic Force Microscopy (AFM). Nonlinear effects were found with the Si sputtering yields, that is, the Si sputtering yield per incident Au atom increased with cluster size ($Y_1 = 3.73$, $Y_2 = 4.04$, $Y_3 = 4.57$).

Liu *et al.* [39, 40] investigated the defect production in single crystal Si irradiated with C_n (n = 1 ~ 10) and Au_n (n=1 ~ 4) cluster at 6 keV/atom energies. The cluster-induced damage in the samples was measured by glancing-angle RBS/channeling. It was suggested that the damage measurement by TWA was either wrong or insensitive to the thin implanted damage layer. The damage was defined as displaced Si atoms per incident atom (DPA). In both cases, significant non-linear effects in defect production were shown for different cluster sizes. For example, when the Au cluster size changed from n = 1 to n = 4, the DPA increased by 80%. An "overlapping model" was proposed for qualitatively explaining the observed results. The same group recently reported the observation of non-linear effects for Cu cluster ion induced damage in Si [41]. Negative copper cluster ions Cu_n (n = 1, 2 ... 7) were produced by Cs^+ sputtering of solid Cu targets and were used to bombard *p*-type Si wafer. DPA levels were found to increase with increased cluster size and for Cu_7 were 13.5 times larger than for Cu_1.

Effects of cluster ion impact on surface morphology have also been studied. Scanning tunneling microscopy (STM) imaging revealed traces of large crater shapes on HOPG surfaces irradiated by 150 keV Ar_{100} ions, while small hillocks with the height of 0.2 ~ 0.3 nm were observed on HOPG surfaces irradiated by 1.5 keV Ar monomer ions [42]. Atomic force microscopy (AFM) and high-resolution transmission electron microscope (HRTEM) cross section imaging have been used to examine craters on

Si(100) and Si(111) surfaces subjected to individual Ar gas cluster ion impacts [43]. Craters on a Si(100) surface are nearly triangular in cross section, while the Si(111) craters exhibit four-side symmetry. $(CO_2)_{750}$ at the acceleration voltage of 40-60 kV created hillocks of a few nm height on different solid surfaces such as HOPG, Si with native oxide and sputter deposited Cu/Si and TiO_2/Si films, which were identified by AFM imaging. After prolonged irradiation, the density of hillocks was increased and the surface roughness seems to be smoothed due to filling the gap between the hillocks [44].

The MD simulated and experimental sputtering yields of metal surfaces (Cu, Ag and Au) due to Ar_n (n = 200~800) bombardment were presented as a function of total cluster energy (6 ~ 20 keV) [45]. A power dependence of the sputtering yield on total cluster energy ($Y \sim E^{1.4}$) was proposed. The angular dependence of sputter ejection was studied experimentally and by simulation (normal incidence of 20 keV Ar_{3000} cluster on Cu surface). “Lateral sputtering” is clearly evident in the experimental data and even more evident in the MD simulations. Oblique incidence at 60° off-normal direction shows strongly forward-directed sputtering. Monte Carlo simulation of 20 keV Ar_{1000} clusters impacting on a rough Si surface predicts smoothing at normal incidence and roughening at oblique incidence.

The smoothing effect of large gas cluster ions has been demonstrated on various material surfaces [46-48]. The gas cluster ions, which consist of tens to a few thousands of atoms or molecules of gaseous materials, are generated through the adiabatic expansion of source gas through a narrow nozzle. The so-called Gas Cluster Ion Beam (GCIB) processing equipment is commercially available from Epion Corporation, Billerica, MA.

The possible application of cluster ion in advanced SIMS metrology has been of high interest in recent years [49, 50]. It was found that there was a significant enhancement of secondary ion yields when clusters are used in place of single ions. This is likely to be exploited in SIMS measurements of biological materials [49]. Using cluster ions, one may enhance the yield of secondary ions emitted from near-surface region of the sample. For organic surface characterization by SIMS, the use of small cluster primary ion beams, such as C-8, can enhance molecular secondary ion signals by several orders of magnitude. In addition, accumulation of beam-induced damage can be substantially reduced. Large Ar cluster ions have also been proposed as primary ions in SIMS technology [50].

1.4 The Objectives and the Scope of the Dissertation

The main objectives of this dissertation work include evaluating the effects of implantation of decaborane ions in silicon and understanding the physical phenomena involved in the process. The goals are to expand the knowledge base of the technology of ultra shallow *p*-doping in CMOS devices and to advance the science of cluster ion beam in general.

To study the properties of decaborane ion beams and investigate the implantation process of B into Si with decaborane cluster ions, a full-scale research implanter with acceleration energy up to 20 keV was constructed at the Ion Beam and Thin Film Research Lab of NJIT. $B_{10}H_x^+$ ions and B^+ ions were generated by energetic electron bombardment of $B_{10}H_{14}$ vapor or BF_3 gas, magnetically mass analyzed, and implanted into Si samples. Ar^+ ions were used for system calibration and as a reference for surface modification studies. The implanted doses were determined by Nuclear Reaction Analysis (NRA) and compared to the nominal doses calculated from the ion beam current integration. Chapter 2 describes details of the research implantation system. Described in Chapter 3 is the work that has been carried out for the purpose of continuing system improvements, including design and implementation of a new ion source and a beam profiler. Chapter 4 introduces the characterization techniques employed in the research, including Secondary Ion Mass Spectrometry (SIMS), Rutherford Backscattering Spectroscopy (RBS), and Atomic Force Microscopy (AFM).

Transient Enhanced Diffusion (TED) of B in Si implanted with $B_{10}H_x^+$ ions at various incident energies was studied and compared with TED after B^+ implantation at an equivalent energy, as described in Chapter 5. Si samples with B marker layers were used for TED studies. The results show that cluster ions and monomer B ions lead to the same amount of enhanced diffusion of the dopants. Depth distributions of B and H in Si implanted with energetic ions were obtained by SIMS analysis. Results show that shallow junction depth can be achieved with decaborane implantation and the co-implanted hydrogen atoms almost entirely diffuse out after activation annealing, leaving no significant effect on the device properties.

The study of the effects of decaborane bombardment on the surface of Si is described in Chapter 6. The sputtering yields of Si by decaborane cluster impact were measured by RBS on special Si/C/Si samples. Atomic Force Microscopy was used to reveal the surface morphology of implanted samples before and after energetic cluster ion irradiation.

Computer simulations with Molecular Dynamics (MD) technique were performed and the results are presented in Chapter 7. Depth distribution of B implanted with B_{10} clusters was obtained from MD simulations and was compared with that of B implanted with B monomers obtained from both MD simulations and a TRIM simulation. The simulations also provide information on the crystal damage and sputtering of Si impacted by B monomers and B_{10} clusters. The simulation study helps to better understand the physical process involved in the cluster-solid interaction and distinguishes between the collision events caused by cluster ions and that caused by monomer ions.

CHAPTER 2

EXPERIMENTAL SYSTEM

2.1 System Overview

To study the properties of decaborane ion beams and investigate the implantation process with molecular ions, a full-scale research implanter was built in 1998 and subsequently improved, at the Ion Beam and Thin Film Research Lab of NJIT. The ions generated in this system can be accelerated up to 20 keV. All implantation experiments for the reported dissertation work were performed on this research implanter. A schematic of the system is shown in Figure 2.1. The system consists of three major sections:

1. The ion source section includes the ion source, source chamber, and gas delivery system.
2. The magnet section holds an analyzer magnet used to select ion species with the desired mass.
3. The end station consists of the beam scanning plates, beam profiler, and the sample chamber that contains the sample holder and the Faraday cage structure.

The overall length of the beam path from the source to the sample holder is approximately 2.5 m. The beamline was constructed of 4″ diameter vacuum plumbing tubes and crosses (Dependex^{TM}). Special transition flanges were fabricated to accommodate the magnet chamber and the source high-voltage bushing. Details of each section are described in the following sections.

The vacuum and gas delivery system is shown in Figure 2.2. The three major sections of the implantation system can be separately evacuated to pressure levels as low as $\sim 10^{-7}$ Torr by three turbo-molecular pumps and can be separated by two gate valves (GV1 and GV2). These turbo-molecular pumps shared a common foreline backed up by a mechanical rotary pump (Edwards model E2M-12). Since decaborane and BF_3 are toxic, an active carbon filter followed by an absorption filter was installed to the inlet side of the rotary pump to limit the potential contamination of the pump oil and the exhaust. An oil mist filter and another active carbon filter were connected to the pump outlet to further clean the exhaust gas before it was vented out of the laboratory.

The gas manifold was constructed of 1/4″ stainless steel tubes and connected to the source gas inlet of the ion source via a flexible stainless steel tube. Decaborane powder was stored in a container provided by ATMI (Advanced Technology Materials Inc., Danbury, CT). The decaborane vapor was obtained by sublimation at room temperature (vapor pressure = 0.15 Torr at 20°C). Ultra-high-purity argon gas was used to test the source operation and to calibrate the magnet setting. BF_3 gas was used to generate monomer B ions. Each gas container has a separate shut-off valve. Argon and BF_3 shared a common metering valve for precise flow control while decaborane vapor is extracted at full valve opening. The decaborane and BF_3 containers were connected to the gas manifold that was at high voltage during the source operation and was mounted onto a thick insulation plate bolted to the supporting frame of the apparatus. The argon cylinder was at ground potential and was connected to the manifold through polyethylene tubing.

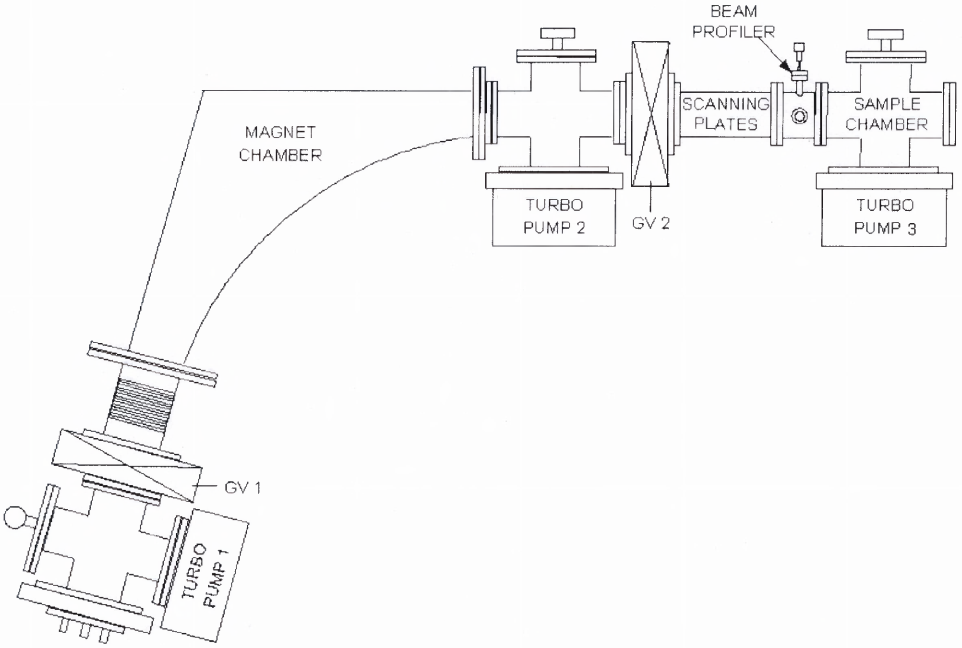

Figure 2.1 Research ion implantation system at NJIT. The System consists of three major sections: 1) ion source, 2) analyzer magnet, and 3) end station.

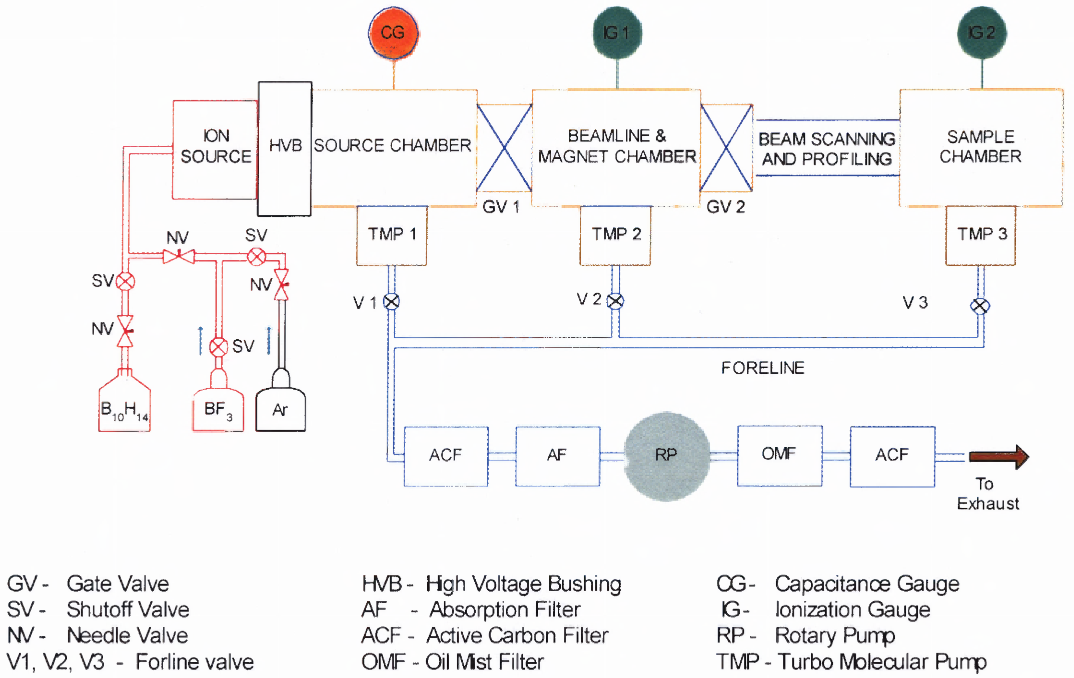

Figure 2.2 Vacuum and gas delivery system for the research ion implantation system.

2.2 Initial Electron Impact Ion Source

The electron impact ion source was initially designed and built as part of a Master thesis of Mr. Gurudath [51]. The design was based on a Bayard-Alpert ionization gauge. The source consists of an ionizer assembly (hot filament cathode, spiral-shaped anode and a gas inlet) and electrode assembly (extraction, focusing and acceleration electrodes). Figure 2.3 shows the ion source and its schematic with power supply connections.

Inside the ionizer, electrons emitted by the hot tungsten filament were accelerated toward the anode by the electric potential difference and passed multiple times through the volume enclosed by the spiral anode. The source gas was supplied through the gas inlet and ionized by the energetic electron bombardment. The ionization efficiency was controlled by adjusting the electron energy and the abundance of the ions reached a maximum at about 70 eV electron energy. The generated positive ions were extracted and focused by the electrostatic fields formed by applying appropriate electrostatic potentials to the extraction and focusing electrodes. The potential difference between the ionizer and the grounded acceleration electrode determined the final ion beam energy.

Although this initial ion source could supply satisfactory decaborane or argon beam currents, it had several major problems including poor structure rigidity, low vapor pressure in the ionizer area, arcing at high acceleration voltage and difficulties in handling and filament replacement. An improved ion source, which is described in section 3.1, was constructed as part of the work of this dissertation.

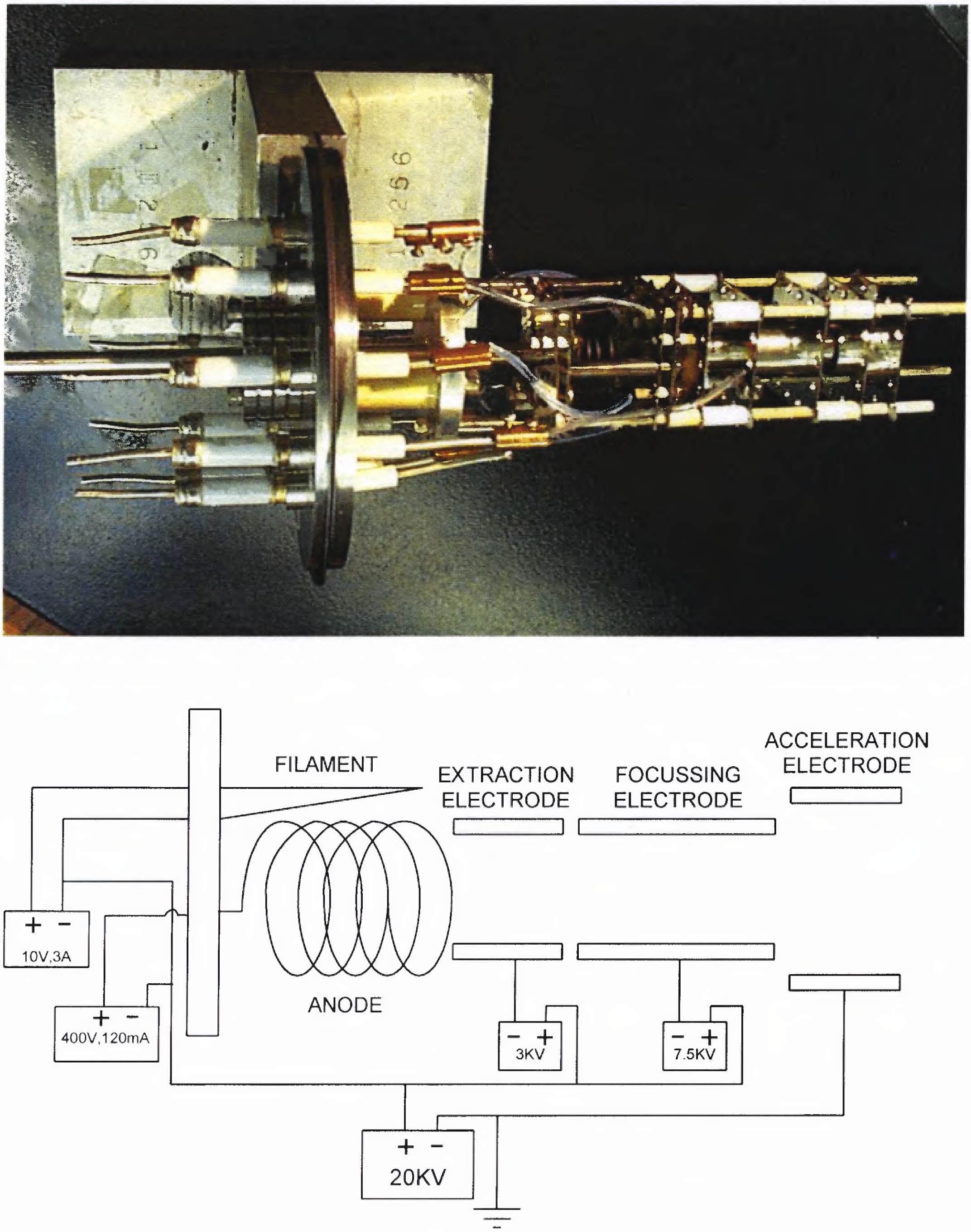

Figure 2.3 The initial ion source and its electrical connections.

2.3 Mass Analyzing Magnet

2.3.1 Fundamentals and Specifications of the Magnet

A mass analyzing magnet is a key component in any commercial ion implanter. The desired ion species can be precisely selected to pass through the magnet and then be implanted into the target, which is one of the major advantages of ion implantation over other doping techniques such as diffusion and PIII. To reliably evaluate the effects of implanted decaborane ions in silicon, all decaborane implantation experiments reported in this dissertation were carried out with mass analyzed ions. The magnet used in the research implanter has a 53.8 cm nominal radius *R* of the ion trajectory and deflects the beam by 70°. The magnet chamber has a rectangular cross section in which the field is not uniformly distributed. There is a stronger field on the outer side and a weaker field on the inner side so that the ion beam is focused in the horizontal plane into a thin ribbon. The object distance is 26.7 cm and the image distance is 36.8 cm. The magnet was a component of an Eaton NV-10 high-current implanter before it was donated to NJIT by Eaton Corporation (now Axcelis Technologies).

As shown in Figure 2.4, when ions travel through the magnetic field, the magnetic forces perpendicular to their velocity cause them to follow a circular trajectory [52]. The magnetostatic field does not change the kinetic energy of the particle, but only changes the direction of its velocity. The radius *r* of the circular path is proportional to the velocity of the particle and is calculated using the following equation:

$$r = \frac{mv}{Bq} = \frac{1}{B}\sqrt{\frac{2mV_a}{q}} \tag{2.1}$$

where, r - radius of curvature of the ion trajectory in the magnet

m - mass of the ion

v - ion velocity

B - magnetic field

q - charge of the ion

V_a - acceleration voltage at the ion source

The magnetic field can be adjusted to obtain ions of desired mass-to-charge ratio (m/q) for a given acceleration voltage V_a. As ions enter the analyzer magnet, heavier ions strike on the outer wall and lighter ions strike the inner wall. Only those ions whose radiuses of circular path are close to the nominal radius R of the magnet can pass the magnet. It is possible, however, that other ions may be accepted if they have a similar value of m/q. The spread of the radius of the accepted ion trajectories is defined by the width of the exit aperture of the magnet.

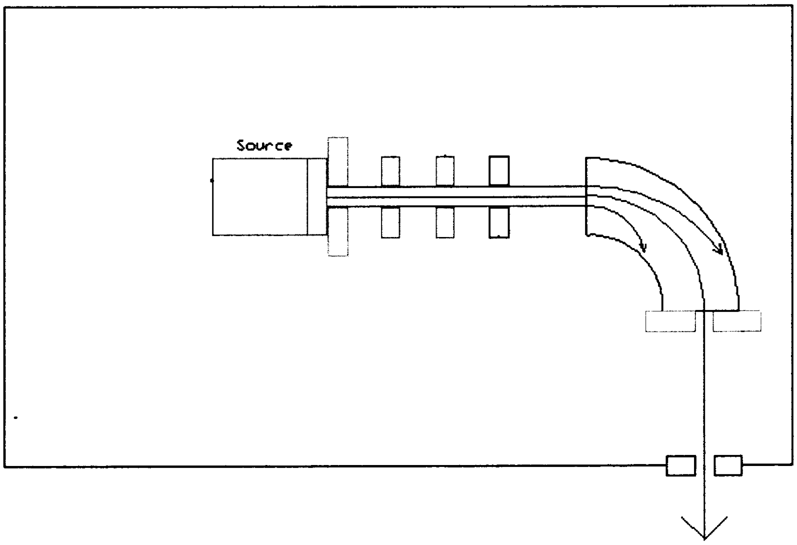

Figure 2.4 Illustration of the analyzer magnet operation.

Mass resolution Δm is defined by the exit aperture width. If a singly charged ion of mass m is selected to travel through the magnet along the nominal radius of the magnet, then at the magnet exit, an ion of mass $m + \Delta m$ will be separated from the first ion by a distance Δx given by:

$$\Delta x = \frac{r\Delta m}{2m}\left[1 - \cos\phi + \frac{L}{r}\sin\phi\right] \tag{2.2}$$

where,

r - radius of the ion path (53.8 cm)

L - image distance of the magnet (36.8 cm)

m - mass of the ion

ϕ - deflection angle of the magnet (70°)

Since Δm is proportional to mass m for a given Δx and proportional to Δx for a given ion specie of mass m, the mass resolution is lower for an ion specie of higher mass (like $B_{10}H_x^+$) than for an ion specie of lower mass (like Ar^+). Experiments were performed to determine the conditions for mass resolution with these ions, as reported in a recent NJIT PhD thesis [31].

2.3.2 Magnet Control and Calibration

The magnet is rated at 8,500 gauss for a current of 150 amperes and is cooled by circulating water. The block diagram of the magnet control is illustrated in Figure 2.5.

A HP 6269B power supply, operating under constant-current mode, was used to supply voltage to the magnet. Control of the magnet was achieved with the help of a circuit providing a control voltage to the magnet power supply, as shown in Figure 2.6. A Motorola 12 V (0.13 A)/ +5 V (0.5 A) DC power supply was used to power the control circuit. For system adjustment before the implantation process, the control voltage was manually adjusted until the beam current measured on a wire probe in front of the sample was maximized (for details on ion current measurement, see section 2.2.4). The adjustment was realized by using a coarse 0-25 kΩ, 10-turn potentiometer and a 240 Ω, 10-turn potentiometer for fine tuning. The magnet setting was represented by a "magnet reading", which was the voltage across a 0.33 mΩ high-power resistor connected in series with the magnet coils and was displayed on a FLUKE 8840 multimeter equipped with an IEEE 488 interface. All components of the control circuit were mounted in a grounded aluminum case. For the safe operation of the magnet, a water flow switch (Model 0100B110, Proteus Industries Inc.) was mounted in the cooling water piping and set to the specified cooling water flow of the magnet. When the water flow dropped below the specified value, the switch cut off the power supply to the control circuit and thus stopped the magnet operation. At the same time, an LED was lighting and an alarm was activated.

In order to facilitate the recording of an ion current spectrum, the control voltage could be controlled by a PC equipped with a National Instrument Data Acquisition (DAQ) board and a General Purpose Interface Bus (GPIB) board. A LabVIEW program was written for this purpose, as part of a Master's Thesis [53]. This program obtains data on ion currents and supplies a signal for control voltage via the DAQ board. It communicates with the FLUKE 8840 multimeter through the GPIB card to obtain the magnet reading (voltage across the high-power resistor in mV) which is the x-axis of an ion beam spectrum, as shown in Figure 2.6. A digital current integrator (EG&G ORTEC model 439) was used to provide a digital output (pulse frequency) that is proportional to the input ion current. The frequency was read by the DAQ board and converted in the program into ion current which gives the y-axis of the spectrum. The obtained data were also stored in a spreadsheet file, which later could be used to plot ion beam spectrum versus mass, using the method described below.

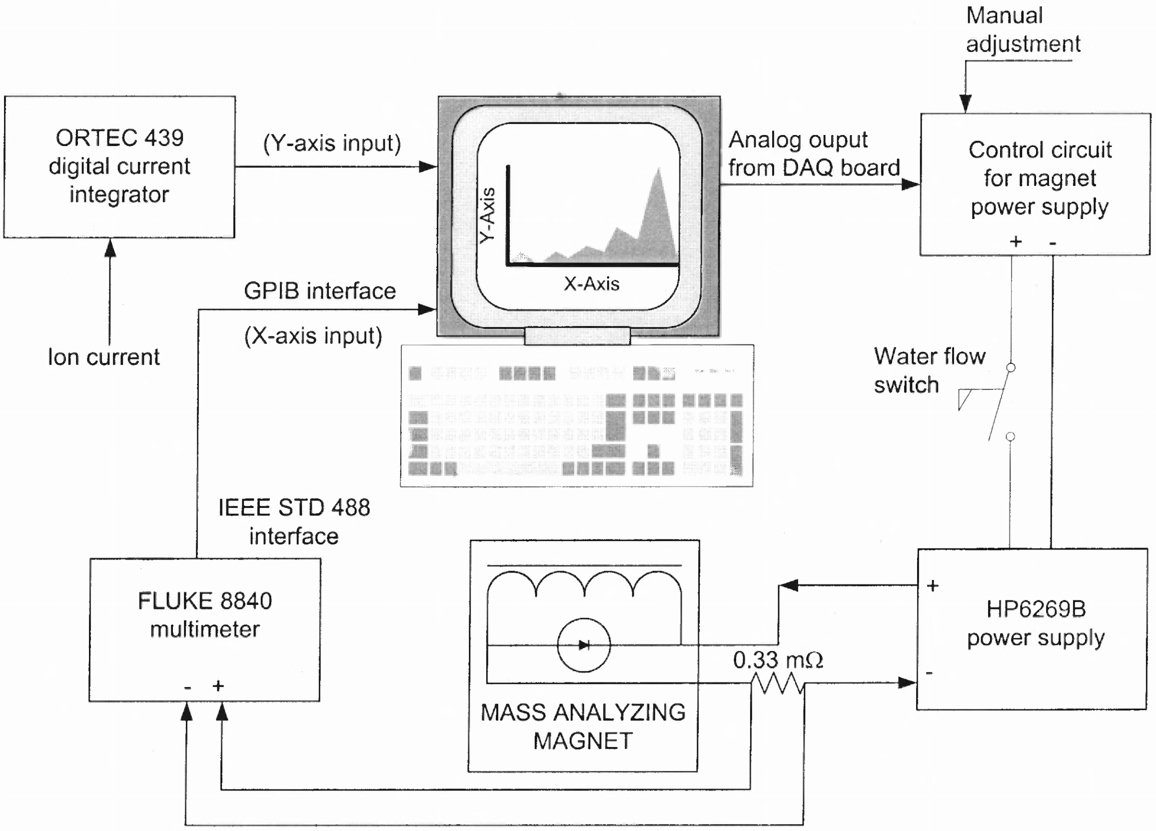

Figure 2.5 A block diagram of magnet control. Manual adjustment was used for the purpose of system adjustment before implantation. When it was needed to take an ion current spectrum, the control voltage could be adjusted from a PC running a LabVIEW program.

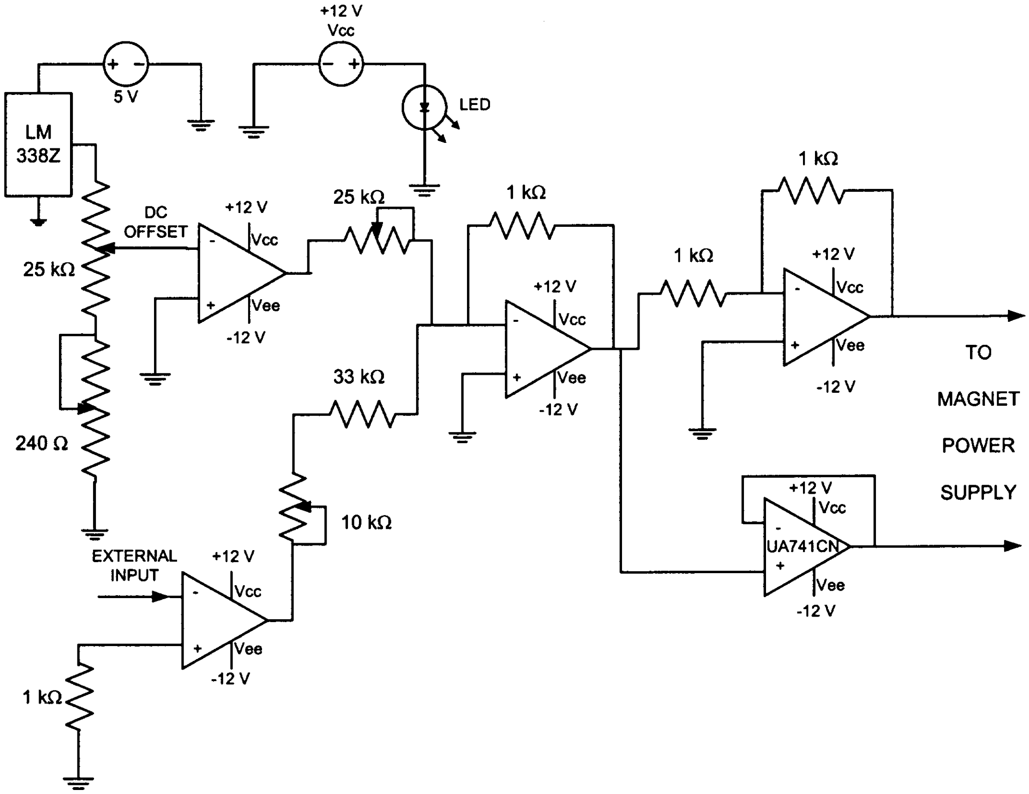

Figure 2.6 Control circuit for the magnet power supply.

The relation between the magnet reading and ion mass was established by a calibration procedure using argon ions [31]. Argon is suitable for calibration of the magnet since its natural form consists practically of a single isotope ^{40}Ar (^{40}Ar = 99.600%, ^{38}Ar = 0.063% and ^{35}Ar = 0.337%). There are two prominent charge state peaks in an argon ion beam spectrum, Ar^+ and Ar^{++}. According to Eq. (2.1), the doubly charged Ar^{++} ions are selected at a magnet reading (mV) that is $1/\sqrt{2}$ times that for Ar^+. This was observed on the graph of ion current vs. magnet reading (Figure 2.7). The highest peak corresponds to the most abundant Ar^+ and appeared at a magnet reading that is $\sqrt{2}$ times that for Ar^{++}, since the magnet reading is proportional to the magnet field B. A plot of the square root of ion mass in AMU vs. magnet reading for the two argon peaks forms a straight line, as shown in Figure 2.8. By converting the magnet reading to ion mass based on the calibration curve, an ion current spectrum could be plotted versus ion mass (Figure 2.9). For each of the acceleration energies used in the experiments, a separate calibration curve was measured.

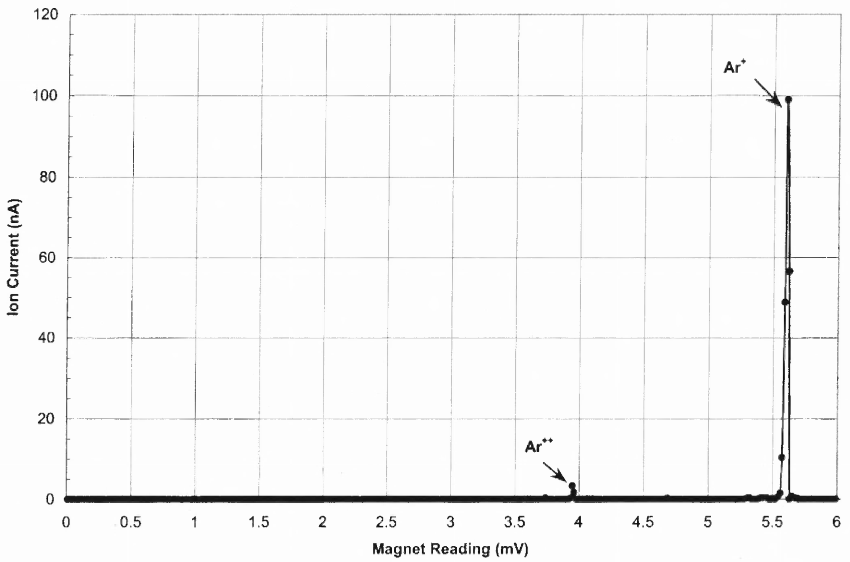

Figure 2.7 Typical ion beam spectrum measured with the LabVIEW program.

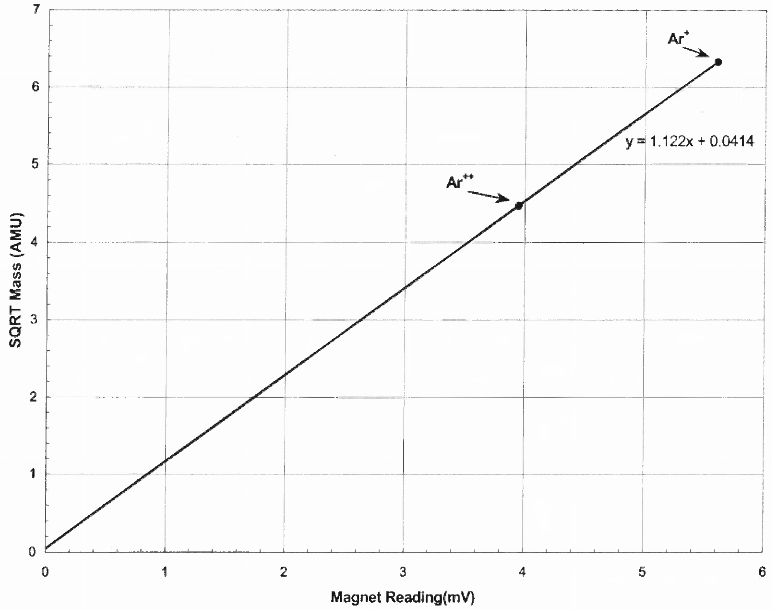

Figure 2.8 Magnet calibration curve obtained with 4 keV Ar ion beam.

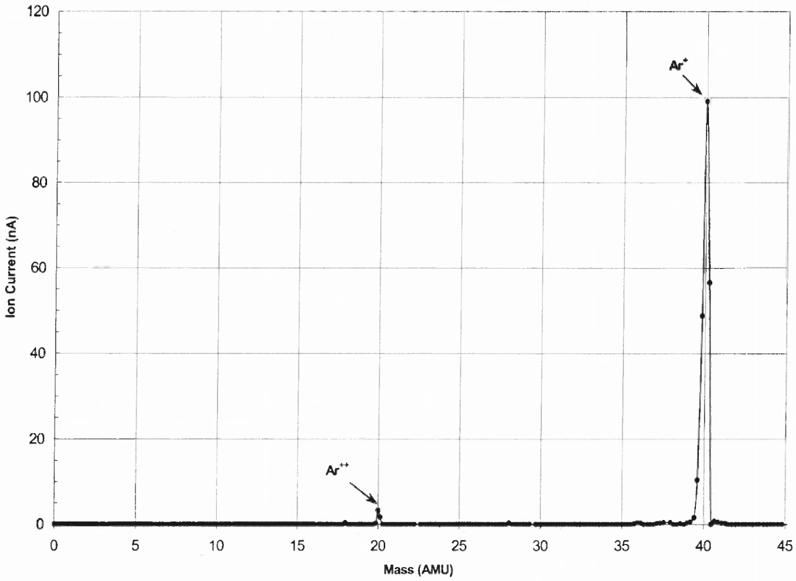

Figure 2.9 Ion mass spectrum for a 4 keV Ar ion beam.

2.4 End Station

The end station of the implantation system was connected to the magnet section by a gate valve (GV2) and consisted of deflection plates for beam scanning, apertures to define the beam size, a Faraday cage for secondary electron suppression, and a sample holder for sample installation. The design of each part of the end station is described in the sections below.

2.4.1 Sample Chamber

As shown in Figure 2.10, a 6-way 4″ cross (Dependex^{TM}) serves as the sample chamber,. A Pfeiffer & Blazers TPU 170 turbo-molecular pump was attached to one side opening of the cross. An aluminum sample holder in the form of a block (66 mm × 29 mm × 29 mm) was attached to the chamber top flange through a vacuum feedthrough. The sample block can be moved in three directions up to 12.7 mm by using three micrometer screws, and can be rotated 360° around its axis. It can also be moved vertically in its longer direction in five 10 mm steps defined by five notches on the shaft of the feedthrough. Each of these notches corresponds to a horizontal marking line on the sample block. The sample was normally mounted with its vertical center aligned with a marker line. When the shaft was moved vertically and locked at a specific notch position, the sample aligned with the corresponding marker line was exposed to the ion beam. By rotating the shaft, samples on three sides of the block could be exposed to the ion beam. A total of nine samples (approximately 15.2 mm × 12.7 mm) were usually mounted at one time on the sample block for implantation experiments. Vertical and horizontal wire probes (1.6 mm in diameter) for beam tuning were mounted on the fourth side of the block. Before implantation experiments, the ion beam was focused on the vertical wire. The horizontal wire was used to manually profile the beam in the vertical direction before implantation for beam uniformity check. This wire was removed after a beam profiler, described in section 3.2, was installed for automatic beam profiling.

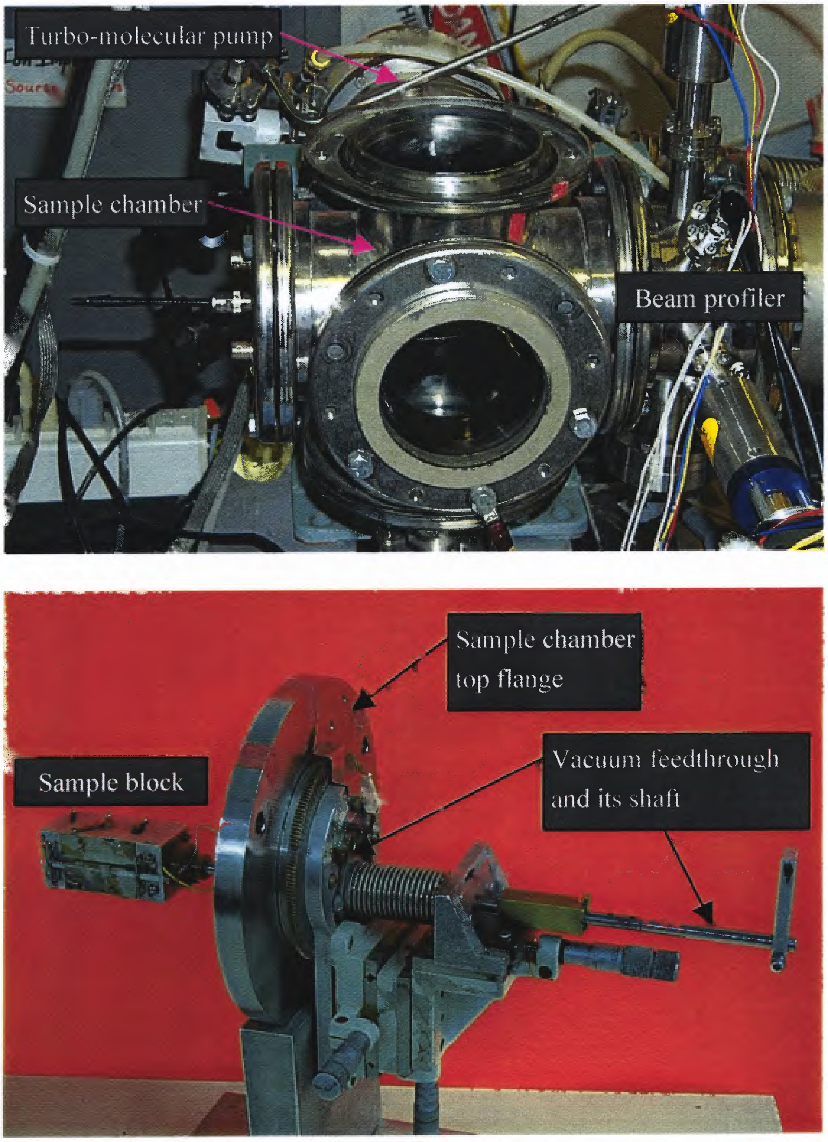

Figure 2.10 A 6-way 4″ cross serves as the sample chamber at the end station (top). The sample holder was attached to the chamber top flange through a vacuum feedthrough (below).

2.4.2 Ion Current and Dose Measurements

Due to the presence of beam defining apertures in front of the sample (see section 2.4.4 for details), only the sample surface rather than the whole block surface was exposed to the ion beam. The sample block and the vertical wire probe were connected inside the chamber with insulated wires to two BNC feedthroughs mounted on the top flange. During system adjustment, two current meters (Keithley picoammeter, model 485) were connected to the feedthroughs via coaxial cables. During the implantation process, the "Block" BNC connector was connected to the input of a digital current integrator (EG&G ORTEC, model 439). The digital current integrator generated a pulse when a specified amount of charge accumulated at the input, depending on the position of a selection switch (10^{-10}, 10^{-8}, or 10^{-6} coulomb/pulse) [54]. For a given setting, the beam current was determined by the pulse frequency, and the total accumulated charge was determined by the number of recorded pulses. This instrument was normally put in "standby" and only set to "operate" position during measurement with its output connected to a counter (EG&G ORTEC, model 871). The counter counted the output pulses from the current integrator. The maximum number of pulses to be counted was set by using the "INC M" and "INC N" pushbuttons for a preset value of $M \times 10^N$. If the actual count exceeded the preset limit, the counter would start over from zero. The time base select switch was set to "EXT" for this mode. The display could also be switched to display the elapsed time counted by the built-in timer by using the mode selection pushbutton.

The current integrator was calibrated and set to 10^{-10} coulomb/pulse for ion current of the order of hundreds of nanoamperes and to 10^{-8} coulomb/pulse for ion current of the order of tens of microamperes. For a given dose and implanted area, the number of counts needed is given by:

$$c = \frac{nq\phi A}{s} \tag{2.3}$$

where, c - number of counts

n - charge state of the ions

q - electron charge (1.6×10^{-19} coulombs)

ϕ - ion dose (ions/cm^2)

A - implanted area (cm^2)

s - Coulomb/pulse setting on the current integrator

The nominal ion dose from an implantation was calculated based on the actual number of counts. The time needed to obtain a given dose can be calculated by using the following formula:

$$t = \frac{nq\phi A}{I} \tag{2.4}$$

where, t - time of implantation (seconds)

I - ion current (amperes)

The actual boron dose in a sample implanted with $B_{10}H_x^+$ or B^+ ions was measured with Nuclear Reaction Analysis (NRA) using a National Electrostatics 5SDH-4 tandem accelerator at Bell Labs, Lucent Technologies. The principle of the NRA system is shown in Figure 2.11. When a 650 keV proton beam of 1 mm in diameter bombards the sample, energetic α particles emitted due to the exoergic nuclear reaction:

$$^{11}\mathrm{B} + {}^{1}\mathrm{p} \rightarrow {}^{8}\mathrm{Be} + {}^{4}\alpha \tag{2.5}$$

are counted by a solid state detector at a 170° back angle. A thin Mylar foil, mounted in front of the detector, stops the more abundant elastically scattered protons but allows the higher-energy α particles to pass and enter into the detector. The number of α particles emitted is proportional to the ^{11}B area concentration in the sample. A standard sample with a known boron area concentration (boron dose) was used to calibrate the system for the proportionality factor of born dose vs. number of α particles detected.

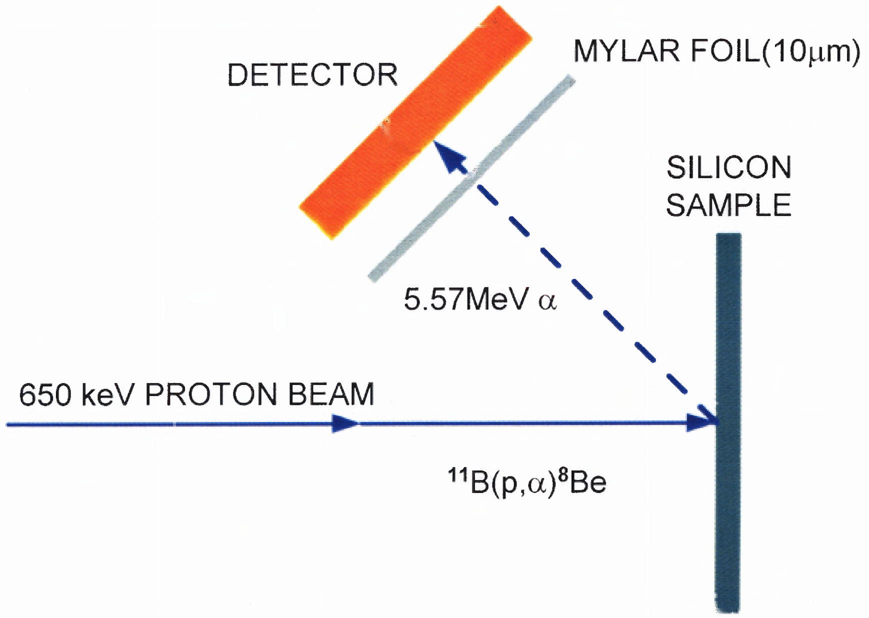

Figure 2.11 A schematic of the Nuclear Reaction Analysis system for measurement of boron dose in a sample implanted with $B_{10}H_x^+$ or B^+ ions. Mylar foil stops more abundant backscattered proton beam allowing α particles from (p, α) reaction to strike the detector and be used to quantify ^{11}B concentrations in near surface of the sample.

2.4.3 Beam Deflection and Beam Profiling

The ion beam at the exit of the magnet was observed to have a ribbon-like shape that could be made uniform in the vertical direction by using appropriate operation conditions of the ion source. To ensure a uniform B dose distribution over the sample, a pair of deflection plates was used for horizontal scanning of the ion beam. The dimensions of the stainless steel deflection plates are 147 mm × 38 mm × 5 mm. The deflection plates were mounted vertically inside the beamline tube (102 mm in diameter) between the magnet exit and the sample chamber. The plates are 38 mm apart and are symmetric to the axis of the beamline. The distance from the exit of the deflection plates to the sample is 117 mm (see Figure 2.12). When the two plates are supplied with a potential difference V_d, the ion beam is deflected on the sample by a distance s that is given by:

$$s = \frac{LV_d(x + \frac{L}{2})}{2dV_a} \tag{2.6}$$

where: s - deflection distance of the beam on the sample (m)

L - length of the deflection plates (m)

V_d - deflection voltage (V)

x - distance from the exit of the deflection plates to the sample (m)

d - distance between the deflection plates (m)

V_a - beam acceleration voltage (V)

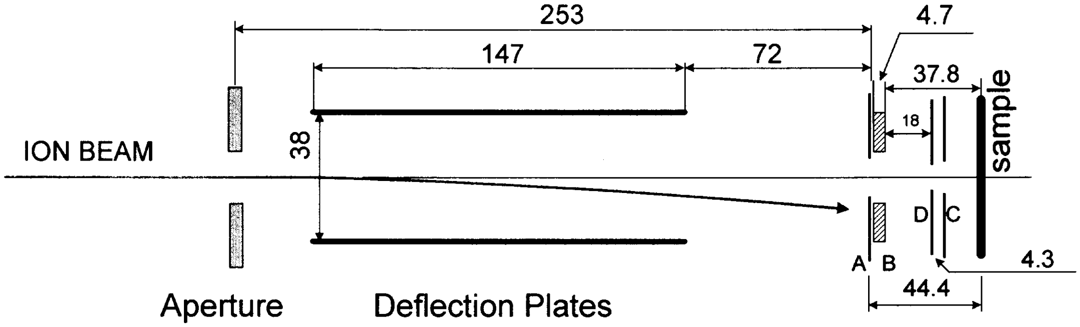

Figure 2.12 Geometry of the deflection plates (all dimensions are in the unit of mm).

The deflection voltage was supplied by a home-made beam sweep generator that generated a triangle-shaped alternate voltage output. The two deflection plates were connected via electrical feedthroughs to the output terminals of the beam sweep generator and also to the two input channels of an oscilloscope (PHILIPS model PM 3207) that was set to display the difference between the two inputs. When an appropriate alternate voltage was applied across the two plates, the ion beam was scanned over the sample surface. The required amplitude of the scanning voltage was determined by using the following procedures,

1) While the ion beam is "ON", tune the source and magnet parameters until the beam current is maximized on the vertical wire probe described in Section 2.4.1.
2) When the electric potentials on the deflection plates are both zero, position the two input signal lines at the center of the oscilloscope.
3) By turning clockwise the "OFFSET" knob on the beam sweep generator, supply positive potential to one deflection plate and negative potential to the

other plate. This bends the beam towards one side and cause the signal line to move upward on the oscilloscope. When the ion current measured on the sample block just drops below zero, stop turning the knob and record the position of the line on the oscilloscope.

4) Then turn the "OFFSET" knob counter-clockwise to make the signal line move downwards. Similarly, record the line position when the ion current just drops below zero.
5) Set the "OFFSET" knob to zero position and set the scanning frequency using the "FREQUENCY" knob. Increase the amplitude using "AMPLITUDE" knob until the peak/valley on the triangle waveform is beyond the Up/Low position obtained in step 2) and 3).

Originally, the ion beam distribution along the vertical or horizontal direction was obtained manually. A metal strip, which is 5 mm in width and 57 mm in height, was attached to the sample block and was moved by turning a micrometer screw. The horizontal beam profile was measured by traversing the metal strip in discrete steps. A plot of ion current on the strip vs. micrometer reading was used to evaluate the beam distribution along horizontal direction. The vertical beam profile was obtained in a similar way by traversing a horizontal probe wire (1.6 mm in diameter) in the vertical direction. Figure 2.13 shows an example of the beam profile obtained by this method.

It was obvious that manual profiling took a long time and sometimes resulted in inaccurate measurements. In the vertical beam profile, for example, a discontinuity at the zero position was caused by the necessity to move the probe position by one notch on the shaft so that the probe could profile the whole range of the beam that was larger than the micrometer motion range (12.7 mm). In order to obtain the beam profiles in a faster and more accurate way, a beam profiler for automatic beam profiling was designed and mounted between the deflection section and the sample chamber. Details of the beam profiler are described in section 3.2.

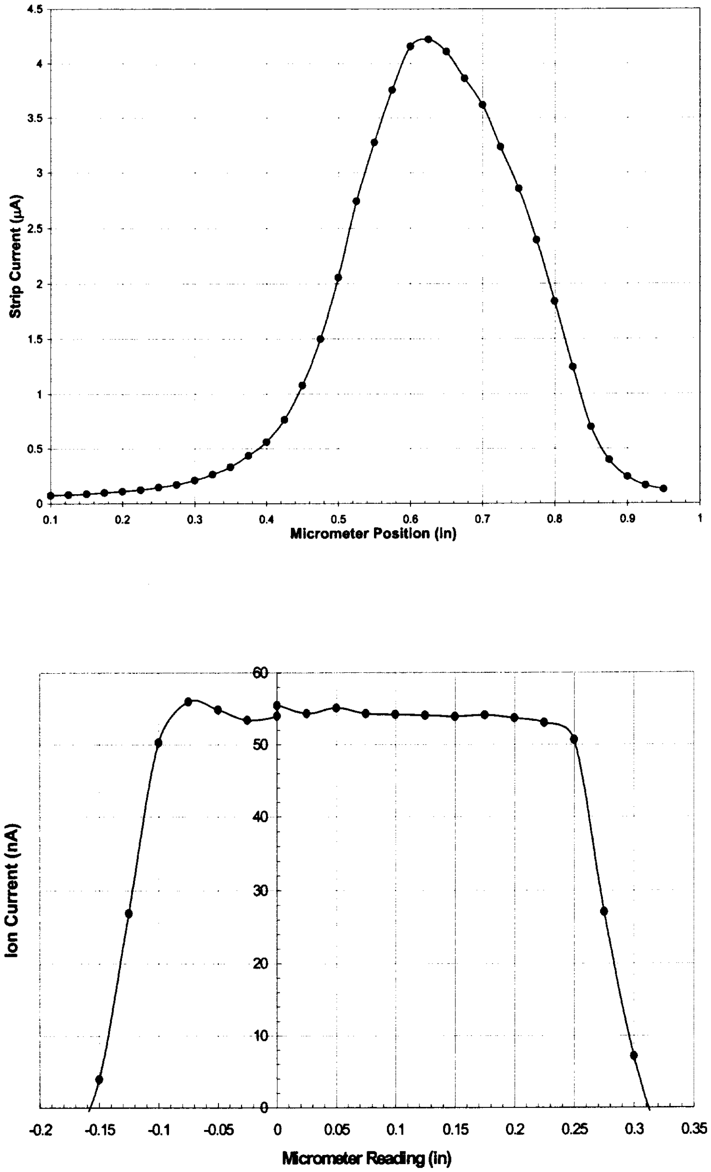

Figure 2.13 Profiles of a 5 keV Ar^+ beam along a) horizontal direction, and b) vertical direction. These profiles were measured by traversing a metal strip or wire probe in discrete steps while monitoring the ion current displayed on the picoammeter.

2.4.4 Beam Defining and Secondary Electron Suppression

When an energetic ion beam impacts on the sample, secondary electrons are emitted from its surface. If these electrons were allowed to freely escape, the current integrator would count them as equivalent positive charges. Secondary electrons are also generated when the high-energy ion beam strikes the edges of apertures or other beam line fixtures. If these electrons were collected by the sample, they would reduce the measured current of positive ions. Both phenomena will cause dose errors. To minimize these errors, an elaborate structure of a Faraday cage and apertures was designed and mounted inside the sample chamber.

After the samples were mounted onto the sample holder, a Faraday cage was attached to the top flange with two plastic screws and enclosed the sample holder inside, as shown in Figure 2.14. The Faraday cage was constructed by attaching a stainless steel mesh around a cylindrical supporting frame fabricated from aluminum. The dimensions of the cage are 8.8 cm in diameter and 16.7 cm in height. The bottom end of the cage was also cover with a round piece of stainless steel mesh.

Figure 2.15 shows the schematic configuration of the apertures and electrical connections for the apertures and the cage. On the front plate of the aluminum frame, a circular opening A (18.8 mm in diameter) was fabricated to allow the ion beam to enter into the cage space. A 38 mm × 38 mm square eV plate (Kimball Physics) with a round aperture B (16 mm in diameter) was positioned 1.3 mm on top of the outside of the cage. It was intended to prevent ions from directly hitting on the edge of the cage opening A. Two pieces of stainless steel foil, which can be seen in Figure 2.14, are mounted above the mesh and used to protect the front of the cage from impact by ions. Both the foils and aperture B are set to ground potential. Other two 38 mm × 38 mm square eV plates different in aperture shape or size were mounted from inside of the cage. All three eV plates were mounted to the cage structure and insulated from each other by using four ceramic rods. Aperture C (10.4 mm × 10.4 mm square) was used to define the beam spot size on the sample. It was set to ground potential by using a wire connected to the top flange. In front of the sample was the suppression aperture D that is also in square shape (13.3 mm × 13.3 mm). Both the suppression aperture and the Faraday cage were negatively biased to the same potential with respect to the ground by a 0-500 V, 0-200 mA DC power supply (Lambda Electronics Corp., model 71). The electrical connections were achieved through BNC connectors on a Dependex type flange that was mounted to the back port of the sample chamber, and the actual voltage was monitored on a HP 6465B digital multimeter.

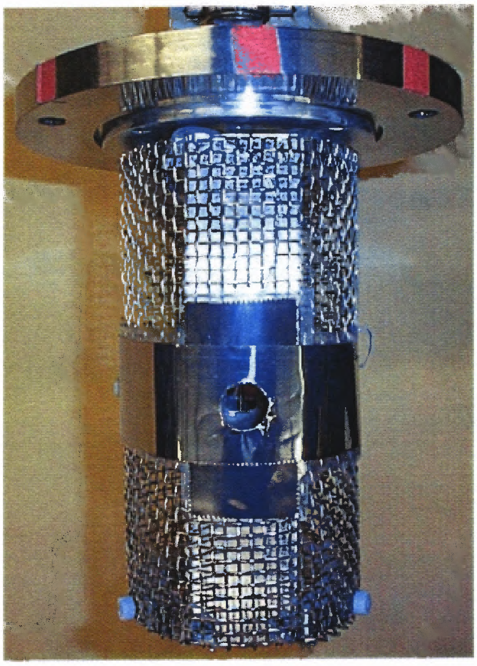

Figure 2.14 The Faraday cage mounted to the top flange of the sample chamber encloses the sample block.

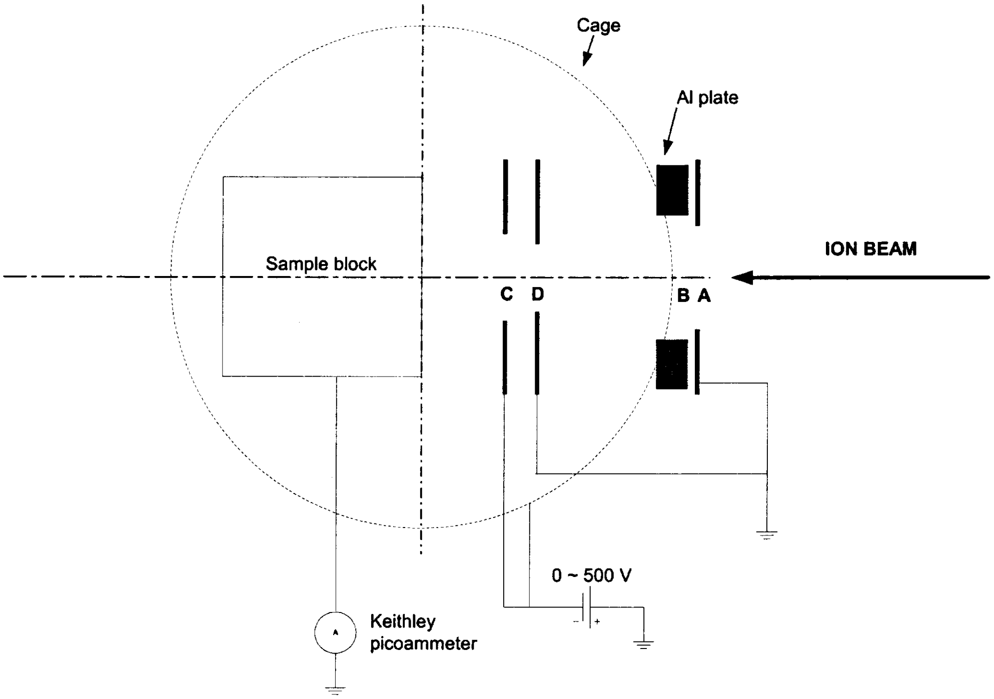

Figure 2.15 Configuration of the apertures mounted on the Faraday cage and their electrical connections.

Since the sample block (or the wire probe) was grounded via the Keithley picoammeter or the current integrator, the negative bias voltage on the cage and the suppression aperture C served to repel secondary electrons that could escape from the sample surface. In addition, the negative potential difference between the suppression aperture C and the defining aperture D prevented those secondary electrons that were generated by ion beam impact on the edge of aperture D from hitting the sample. When a bias voltage was applied, the apparent ion current measured on the sample decreased due to the suppression effect on secondary electrons.

The bias voltage required for full suppression of secondary electrons can be experimentally obtained. For an ion beam of specific ion species and acceleration energy, the bias voltage (up to 400 V) was increased in steps while the ion current was measured on the sample block, until the change of current reading between two steps became negligible. A current vs. suppression voltage curves was then plotted. Figure 2.16 shows a series of such suppression curves obtained for Ar^+ ion beams at energies ranging from 2 keV to 12 keV [31]. As can be seen from these curves, the ion current initially decreased quickly with increased suppression voltage. This might be because most of the secondary electrons were immediately repelled back to the sample block. When the suppression voltage was increased to certain levels, almost all secondary electrons were confined in the sample block and the current reading was not significantly affected by the continued increase in voltage, as shown by the flat region on the curve. The stable ion current measured in the flat region was considered to be the true ion current. Usually, the suppression voltage was set to –200 volts to ensure the full suppression of secondary electrons.

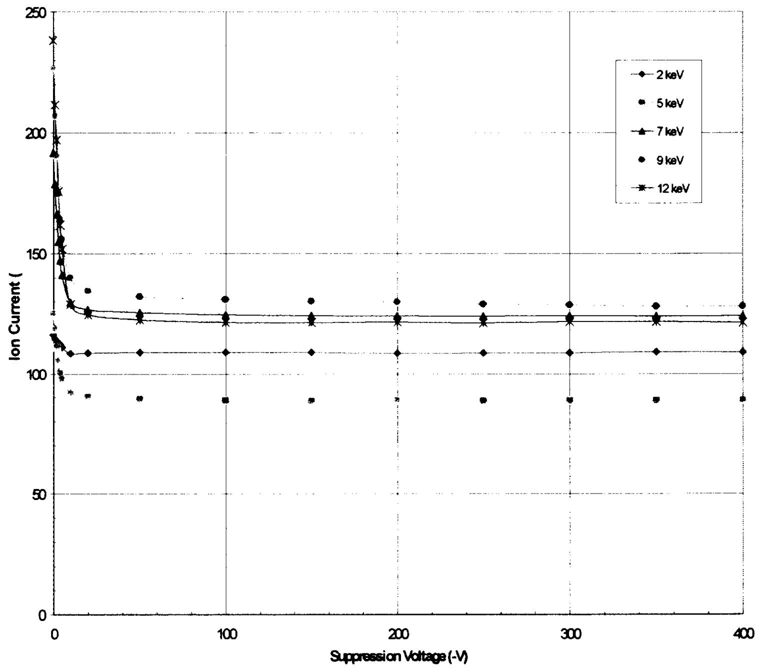

Figure 2.16 Suppression curves for Ar^+ ion beams at different acceleration energies (2 keV – 12 keV). [31]

CHAPTER 3

IMPROVEMENTS TO THE SYSTEM

The research ion implantation system at NJIT was originally constructed in 1998 and has since been improved by students working on the decaborane implantation project [31, 49, 51]. Described in this chapter is the work that has been carried out as part of this dissertation study for the purpose of continuing system improvements.

3.1 New Ion Source

3.1.1 Structure of the New Ion Source

A modified version-2 ion source was designed to solve the problems associated with the initial ion source, as described in section 2.2. The working principles of the new ion source are the same as for the initial source. It consists of three portions: a) an ionizer, b) an ionization compartment, and c) an electrode assembly. Figure 3.1 shows a picture of the new source and its sectioned schematic drawing without the ionizer attached.

The ionizer consisted of an anode, two hot filaments and a gas inlet, and was built from components of a nude ionization gauge, as shown in Figure 3.2. The thin wire in the center of the gauge was removed and a hole was drilled through the 2¾″ Conflat® base flange. A 1/4″ stainless pipe with shoulder was welded to the hole, serving as the gas inlet. This pipe was connected to the gas manifold through a flexible pipe. The spiral-shaped anode was made up of 7 ~ 8 turns of 0.4 mm diameter tungsten wire. The opening of the anode is 20 mm at the top end that faces the extraction electrode. In order to prevent ions from travelling toward the ionizer flange instead of the extraction electrode, the anode was made in a cone shape with gradually decreased diameters at the bottom end. Two tungsten filaments, 0.25 mm in diameter, were mounted to a supporting wire frame. One of them was used as a spare when the other was in use. The potential to the anode and the voltage to the filament were supplied through electric feedthroughs on the base flange.

The ionization compartment consists of two flanges welded onto two ends of a stainless steel tube of 34.5 mm inner diameter. The end flange (the smaller Conflat flange of 2 ¾″ nominal size) is used to attach the ionizer. The front flange holds the electrode assembly and is attached to a Dependex^{TM} type transition flange that is permanently bolted to the source chamber. Two electrical feedthroughs, mounted on the front flange, are used to supply voltages to the extraction electrode (EXT) and to the focussing electrode (FOC), respectively. After the ionizer is attached to the end flange, its major components are all confined inside the ionization compartment. The space confinement design in the new source, in contrast to the open structure of the initial source, allows electrons emitted from the hot filament to have more chances to impact the gas molecules, thus enhancing the ionization efficiency.

The electrode assembly included three electrodes for beam extraction, focussing and acceleration. Each of the electrodes consists of a round stainless steel disc and a cylindrical insert with properly profiled cross-sections. Figure 3.3 shows the disc and insert for the extraction electrode. The edges of the discs were rounded so as to reduce arcing. The insert was tightly fit into the circular opening of the disc and was locked with a set screw from the periphery of the disc. The insert could be easily replaced with one of a different inner diameter or inside profile for optimized performance. The electrodes were assembled by using three 3.2 mm diameter ceramic rods and stainless retaining rings around the ceramic rods. The distance between electrodes could be adjusted by using different spacers. Based on an optimized design obtained with SIMION simulations described below, the entire assembly was constructed and mounted onto the front flange of the ionization compartment by passing three screws through the holes on the extractor disc and securing them onto the flange. Insulating sleeves mounted around the screws were used to insulate the screws from the extraction electrode. As shown in Figure 3.1, one end of the extractor insert was positioned inside the ionization compartment and was very close to the anode and the filament frame. This allowed the ions generated inside the anode space to be extracted more efficiently. Two stainless steel wires inserted through hollow plastic bushings were used to connect the extraction and focusing electrodes to the feedthroughs on the front flange that were labeled with "EXT" and "FOC", respectively. The acceleration electrode was grounded with a third wire connected to the source chamber housing. The potential difference between the anode and the acceleration electrode determined the acceleration voltage of the ion beam.

The distance between the front flange and the extraction electrode was set to be 3 mm by thee ceramic spacers. There was an O-ring compressed in between the flange and the EXT electrode, which was used to tightly seal the space between them in order to prevent the source gas from easily escaping into the open space of the source chamber. This way, a higher vapor pressure was achieved within the ionization compartment for a given gas flow, compared to the situation in the initial source. This not only enhanced the ionization, but also reduced the source gas consumption. This was especially important in this study because of the limited supply and the toxicity of decaborane.

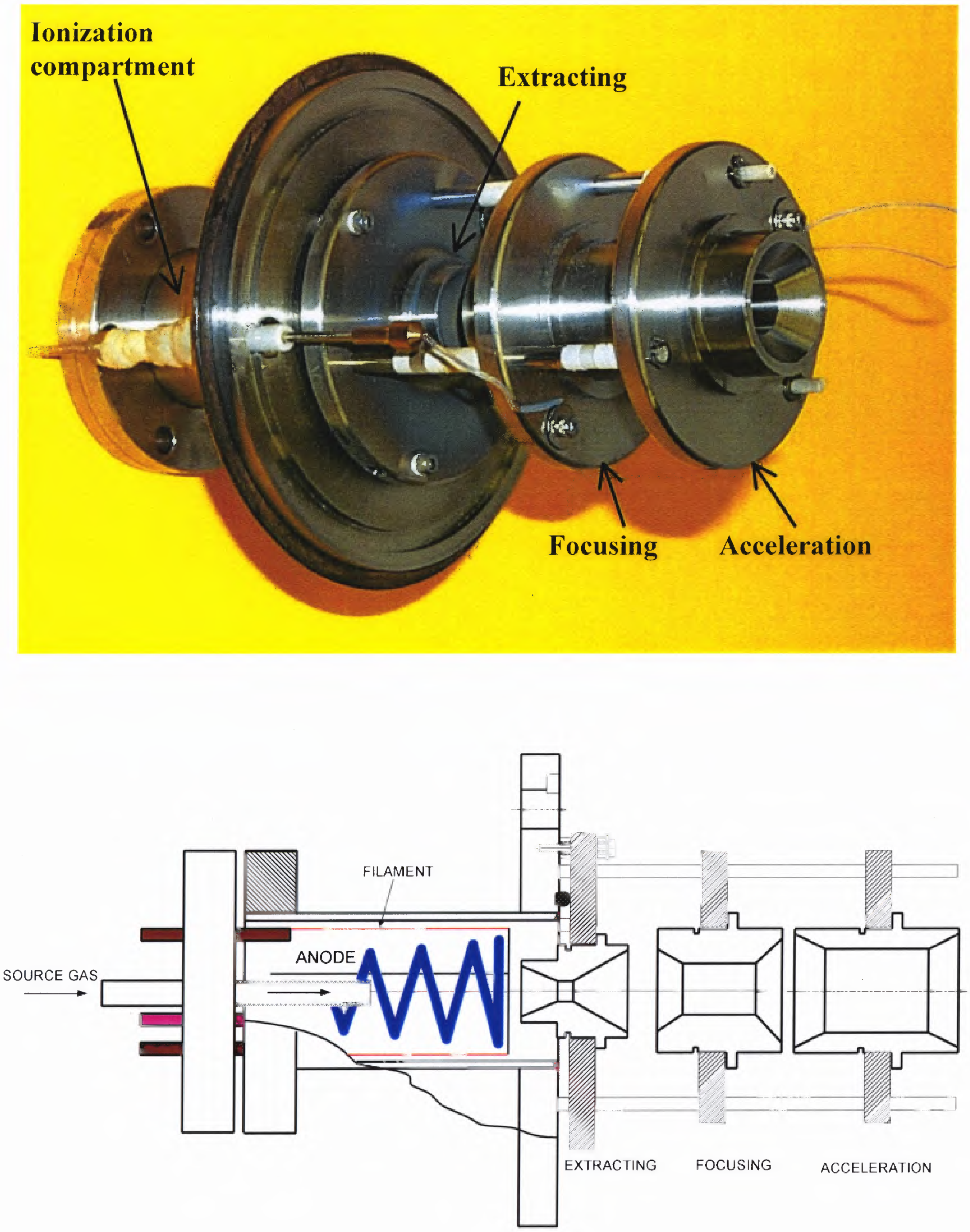

Figure 3.1 A modified ion source was designed to solve the problems associated with the initial one. The constructed source is shown in the top and its schematic drawing is shown below.

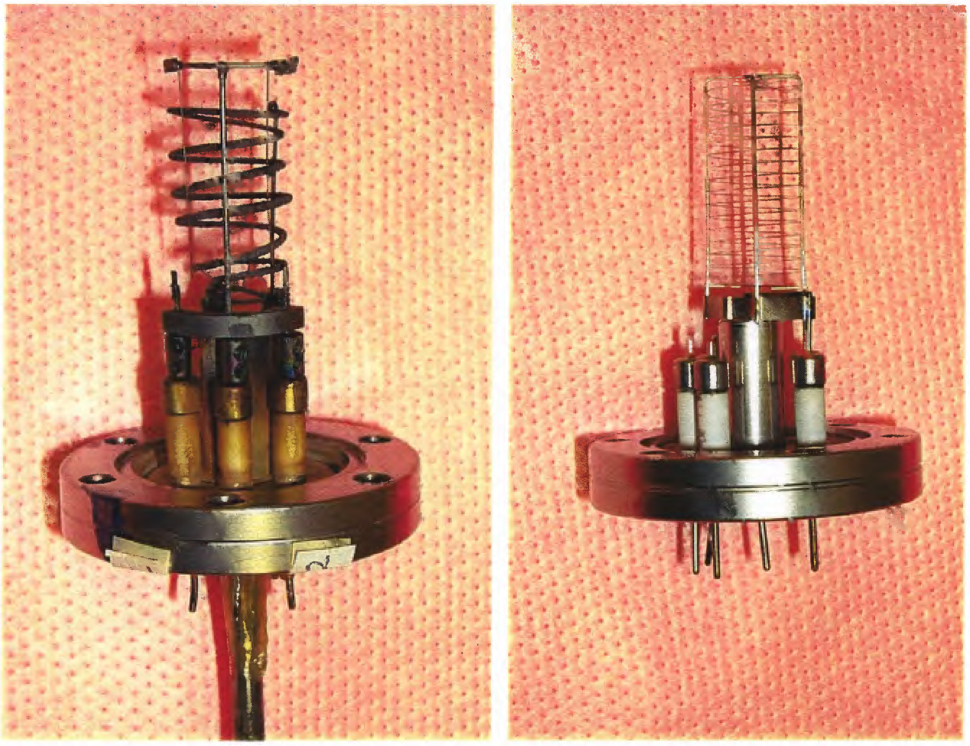

Figure 3.2 The ionizer consisted of an anode, two hot filaments and a gas inlet (left). It was built from components of a commercial nude ionization vacuum gauge (right).

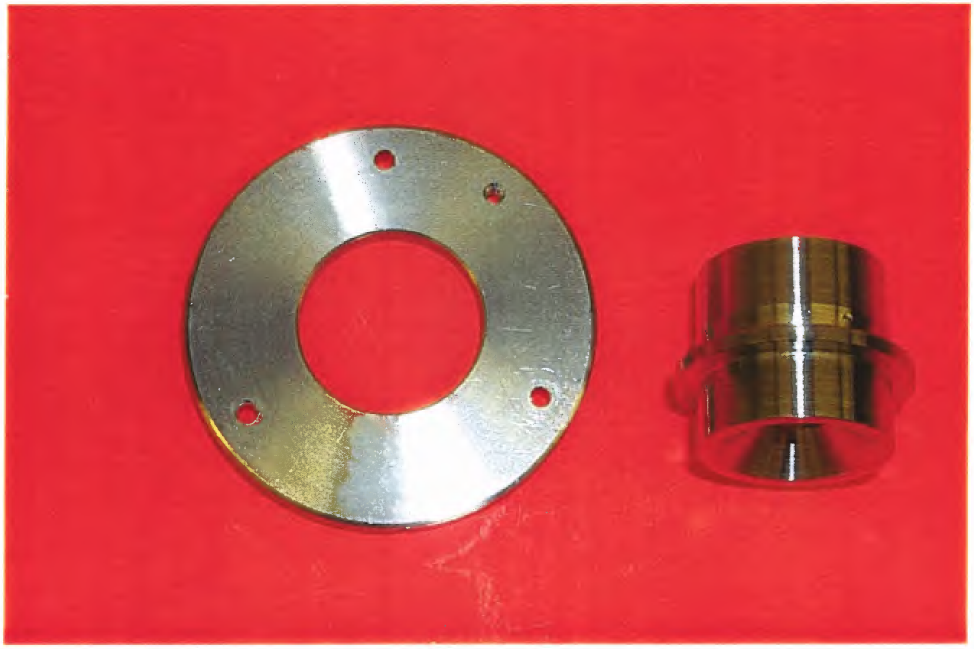

Figure 3.3 Each of the electrodes consists of a round stainless steel disc and a cylindrical insert with properly profiled cross-sections. Shown here are the disc and the insert for the acceleration electrode.

3.1.2 Simulation with SIMION

Computer simulations were carried out for design and optimization of shapes and dimensions of the components of the new ion source and distances between them. For example, the shape and size of the opening and the relative position of the extraction-electrode insert are critical for efficient extraction of ion beams.

The design work was initially based on SIMION 6.0 [55], a program running under the DOS environment, and later transferred into SIMION 3D 7.0 [56], which is an enhanced version operating under Windows (Win32). SIMION is an ion optics simulation program that models ion optics problems with 2D symmetrical or 3D asymmetrical electrostatic and/or magnetic potential arrays. It incorporates an ion optics workbench module for sizing, orientation and positioning of up to 200 instances (3D images) within a workbench volume that can be scaled up to 8 km^3. Arrays can have up to 50,000,000 points. Complex systems or even entire instruments can be modeled. Ions can be flown singly or in groups, displayed as lines or dots, and automatically re-flown to create movie effects. The program can model a wide range of problems including ion source and detector optics, time-of-flight instruments, ion traps, and quadrupoles, etc [56].

SIMION makes use of potential arrays that define the geometry and potentials of the electrodes or, in case of magnetic field, magnetic poles. A potential array is an array of points organized so the points form equally-spaced square (2D) or cubic (3D) grids. The potentials of points outside electrodes and poles are determined through an " array refining" process in which the Laplace equation is solved by finite difference methods. The Laplace equation constrains all electrostatic and static magnetic potential fields to conform to a zero charge volume density. This means no space charge effect is considered in the program. Refined arrays can then be projected as instances into an ion optics workbench volume. Trajectories of ions flowing within the workbench volume are defined by the electrostatic and magnetic fields of the potential array instances.

The following procedures were followed to perform simulations for the new ion source design:

1. Create a potential array with 2D cylindrical symmetry and specified X and Y dimensions. The total number of points within the array is the product of the X value and Y value. In SIMION, if a 2D array has a cylindrical symmetry it will be projected to create a volume that conforms to the cylindrical symmetry around its x-axis, such as the axis of the new ion source.
2. Use the "Modify" function to draw the top half of the X-Y section of the first object. An "object" in the potential array corresponds to a part in the ion source that has a defined electrostatic potential. The anode in the new ion source, for example, is represented by a set of rings with each of the rings being treated as an object. Set the voltage to 1 volt for the first object and to 2 volts for the second object, and so on for other objects. Each of the objects was drawn in scale to the corresponding part in the ion source.
3. Use the "Refine" function to refine the potential array created in step 2. SIMION will scan the array, determine the number of adjustable objects, create a sub-array for each of the objects, and refine and save them as separate files. Use the "Fast adjusting" function to set the desired voltage to each of the objects.

4. Click the "View" button to view the 2D configuration or the potential energy view of the generated potential array. The voltages on the objects can also be fast adjusted from within the View window. Figure 3.4 shows a constructed potential array where the equipotential curves are also displayed as red lines.
5. Define the starting locations, angles, initial kinetic energies and feature colors for ion(s) to be flown through the source (workbench volume). Ions can be defined individually or in groups. Then "fly" the defined ions through the workbench volume. As trajectories of flying ions are displayed as color lines on the screen, different ions or ion groups can be distinguished from each other by means of their line color.

Whenever the dimensions and/or positions of one or more objects are changed, Step 2 ~ 5 must be repeated to generate a new potential array.

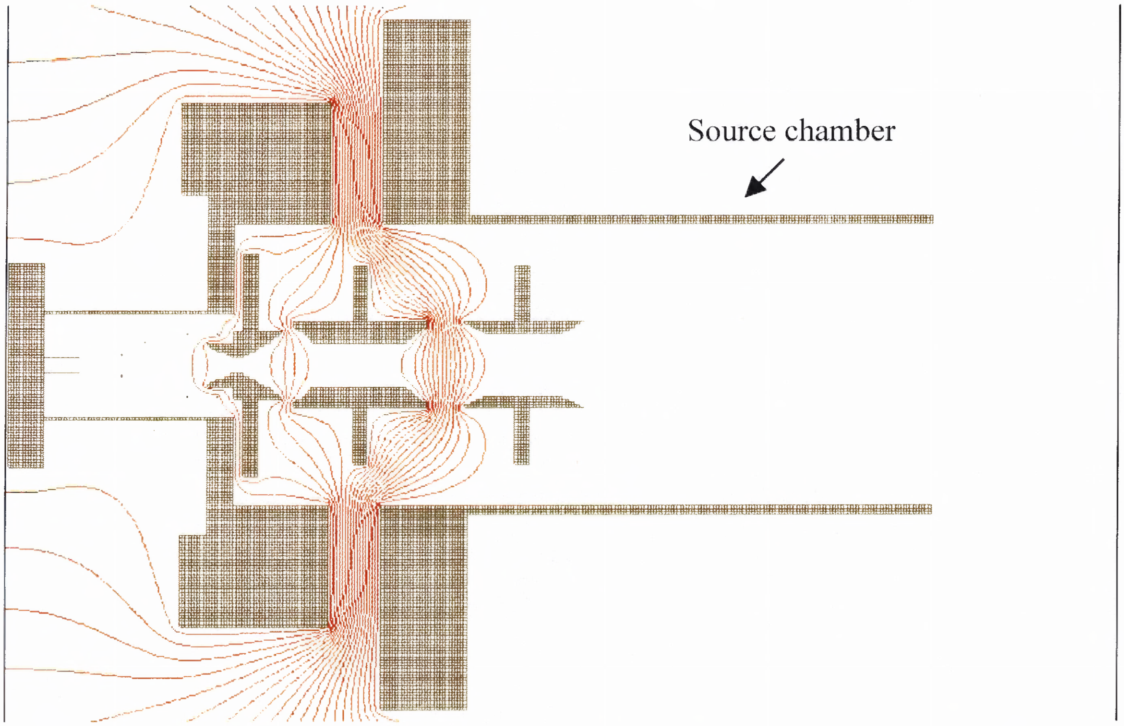

Figure 3.4 2-D view of a constructed potential array for the simulation of the new ion source. The red lines are equipotential curves.

One of the major considerations when modeling the ion source was to have the ion beam focused at a spot 26.7 cm distant before the magnet entrance. This point is seen as the object according to the ion optics design of the NV-10 analyzer magnet. If an ion beam is focused at this object point before entering into the magnet, it will then be focused at a spot 36.8 cm after the magnet exit. For a given electrode configuration and a given acceleration voltage, a series of simulations were carried out to determine the optimized voltages to be applied to the extraction and focusing electrode. In these simulations, three groups of ions (11 ions each group) were defined starting from three different X coordinates. Ions in the same group had the same X coordinate, same initial kinetic energy (0.1 eV) and were equally spaced along the Y direction. Figure 3.5 shows a 2D view of a typical simulation obtained for ions accelerated at 5 keV. The extraction (or focusing) voltage labeled in the graph is the potential of the extraction (focusing) electrode with respect to that of the anode. The simulation shows that the beam formed by ions form one group will have a spot size that is different from that of the beams formed by ions of other groups when reaching at the object point of the magnet. A combination of the electrode voltages that focuses ions of one group may not focus the other two groups. The final selection was made based on comprehensive analysis of several factors, including the beam spot size and divergence of all three groups and the number of ions lost due to collision with the electrodes. In Figure 3.5, the extraction voltage is $V_{EXT} = -100$ V and the focusing voltage is $V_{FOC} = -850$ V, and the beam spot size at the object point is ~ 3 mm. Figure 3.6 is a 3D cutaway view of the same simulation.

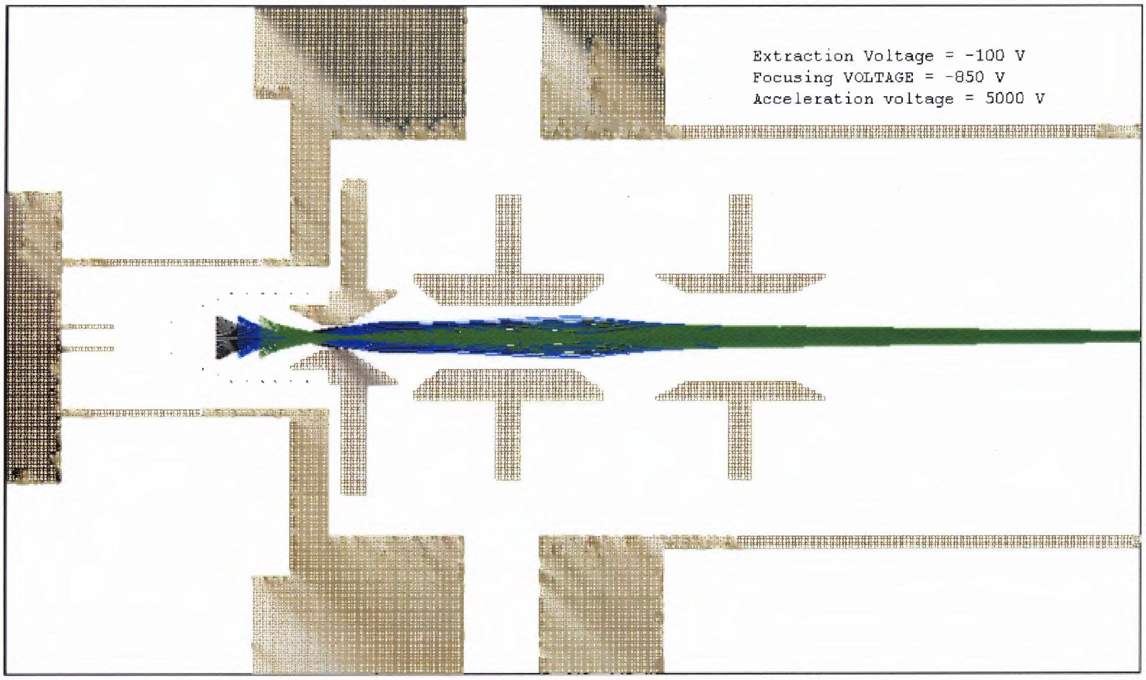

Figure 3.5 2-D view of a SIMION simulation for an ion beam accelerated at 5 keV.

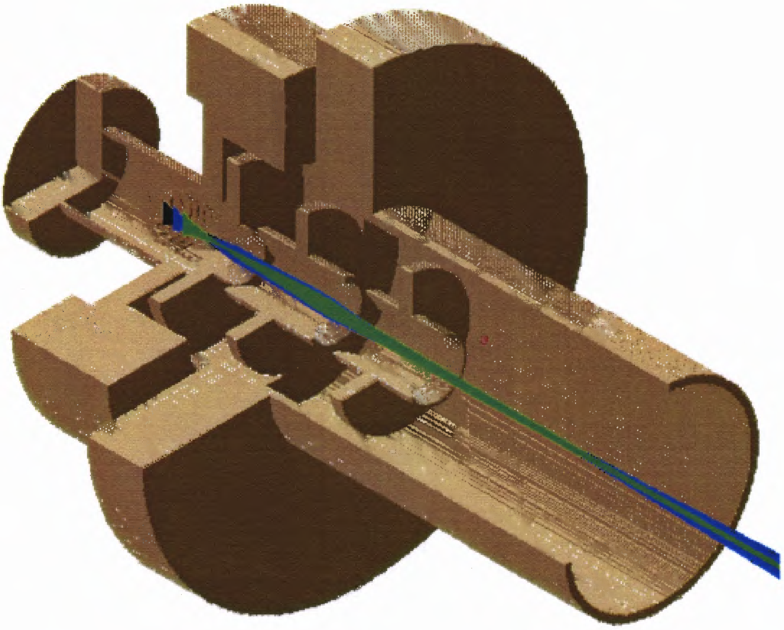

Figure 3.6 3-D cutaway clipping graph of the same simulation shown in Figure 3.5.

The simulations also helped to optimize the geometry of key components of the ion source. For example, in the preliminary design, the inside diameter of the extractor insert was 5mm. When a so designed and constructed ion source was attached to the research implanter for performance test with argon gas, it was found that the ion current was even less that with the initial source and arcing also happened at higher acceleration voltages. Simulations were carried out to find the cause of these problems and they showed that the diameter mentioned above was too small to pass all extracted ions to the next stage, the focusing electrode. Therefore, a new insert was fabricated with the inside opening doubled (10 mm). With the new insert, higher ion currents were achieved and no arcing has been observed.

It should be noted that the conditions obtained with SIMION simulation might be different from the best values found in the actual experiments. This may be related to several factors not accounted for in the simulations. First, SIMION does not consider the space charge effects that normally exist in real sources. Secondly, the ion distributions inside the anode were assumed to be cylindrically symmetric in the simulations. In the real source, however, the filament was on one side of the anode and the density of generated ions could be higher on one side than on the other. Finally, the spiral shape of the anode could not be projected into the simulation instance, but instead was presented with a set of rings.

Nevertheless, the ion optics simulations with SIMION gave valuable information on the ion source operation and helped to design the source structure.

3.1.3 Operation and Performance of the New Source

After the source was constructed, based on the design optimized with SIMION simulations, it was attached to the research implantation system and tested with different source materials including argon gas and decaborane vapor.

Figure 3.7 shows the schematic of the electric connections for the ion source. A 0~20 V, 20 A DC power supply (Electrostatics Inc., Model LS15-15A) was used to supply the filament current and was normally operated at ~ 6 V. The anode was positively biased with respect to the filament with a 400 V, 0-120 mA DC power supply (HP 6209B). One end of the filament was also connected to the source flange by using a copper wire with two clips at both ends. The acceleration electrode was connected to the ground. All the source power supplies were mounted on the shelves inside an electrical cabinet and isolated from the grounded cabinet housing. The acceleration voltage was provided by a precision regulated high voltage DC power supply (CPS Inc., Model CPS-100R, 0-30 kV/1.0mA). The output of the supply determines the potential difference between the source flange and the grounded acceleration electrode, which defines the acceleration voltage on the ion beam. An isolation transformer (rated 20 kV) was used to power the source power supplies. The potentials on the extraction electrode and the focusing electrode were negative with respect to the filament potential and were supplied by a 0-3 kV, 1 mA power supply module (Bertan model PMT-30C/1V) and a 0-7.5 kV, 250 μA power supply module (Bertan model PMT-75C N-S), respectively.

With the new ion source, higher beam currents were achieved at lower gas pressures than with the initial source. For example, at 9 kV acceleration voltage, the maximum decaborane current was ~ 45 nA, measured on the vertical probe wire on the sample block (see section 2.2) without scanning, which is higher than the value of ~ 30 nA obtained with the old source. The new source can also be operated at higher acceleration voltages (up to 18 kV for argon beam and 15 kV for decaborane beam) without causing arcing, which is a major advantage over the old source. Later, this source was also used to supply B^+ ions by electron impact ionization of BF_3 gas, with a beam current of ~ 12 nA at 2 kV acceleration voltage.

In addition, the new ion source has the following features and advantages over the old source:

- The source structure is more rigid and easier to handle. The beam forming electrode assembly with its electrical feedthroughs are mounted onto the ionizer flange that is bolted to the source chamber. Whenever it is necessary to change the filament or anode, only the ionizer itself needs to be disconnected from the back flange of the ionization compartment.
- The filament life is longer than in the case of the old source. This may be attributed to the use of thicker tungsten filament (0.010 vs. 0.005). Typically, one filament can last for about 10 hours when used in decaborane vapor, and more than 24 hours in case of argon or BF_3 gas.
- The ionization process occurs in a more confined volume. This allows a higher operating vapor pressure in the ionizer, enhancing ionization and reducing consumption of source gases.
- The beam forming electrode consists of discs and inserts. The insert of an electrode can be easily replaced with one with a different geometry for optimized performance.

Other modifications had been tried to further enhance the performance of the new ion source. For example, it was attempted to construct a cylindrical anode from stainless steel or molybdenum mesh. The mesh has a transparency of 81.7% (The percentage of open area over the total mesh area). The cylindrical mesh anode was thought to ensure a more uniform electrical field and to better confine electrons inside the enclosed space, thus enhancing the ionization of gas molecules. However, test results showed no significant improvement of the beam current by using this type of anode. A test was also performed with four permanent magnets equally spaced around the outside of the ionization compartment. It was expected that existence of an axial magnetic field could confine electrons more effectively in the ionization space for more collisions with gas molecules. Although no improvement was observed in the ion current, it may be worthwhile to try to establish adjustable electromagnetic fields using a coil wound around the source housing in the future work.

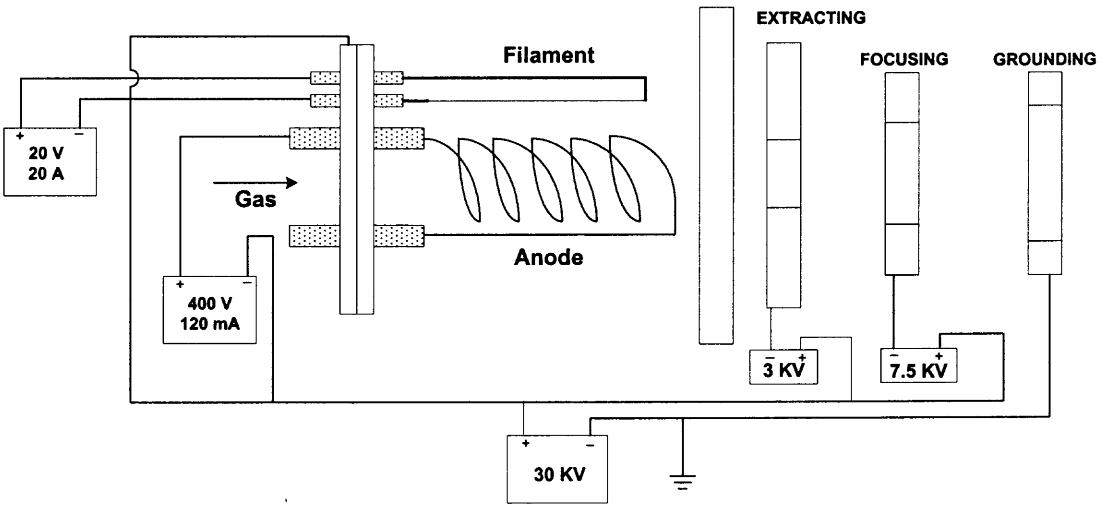

Figure 3.7 Schematic of electrical connections for the new ion source.

3.2 Beam Profiling

As described in Section 2.4, the beam distributions in front of the sample was originally profiled manually by moving either a metal strip or a wire probe, which were mounted on the sample block, across the ion beam in discrete steps. The number of samplings was small for completing the measurements in a reasonably short time. All values of the micrometer positions and the corresponding ion current readings had to be written down by hand and later be used to plot a position vs. current graph. Usually it required the collaboration of two students to perform the profiling work and thus it was only carried out for system adjustments, or before the implantation process started. In order to obtain the beam profiles more efficiently at any time during an experiment, a beam profiler was designed and mounted between the deflection section and the sample chamber, as part of the dissertation study. Figure 3.8 shows the beam profiler mounted in the beamline. The operation of the beam profiler was controlled from a personal computer (PC) by using a LabVIEW application program. Details of the beam profiler are described in following sections including its configuration, operation and control software.

3.2.1 Structure and Configuration of the Beam Profiler System

The structure of the beam profiler is schematically shown in Fig 3.9. The main body of the beam profiler is a 4″ diameter stainless tube. Both ends of the tube are connected to the deflection section on one side and the sample chamber on the other. Three smaller (3/4″ OD) stainless tubes, separated by 45°, were welded to the main tube perpendicular to its axis, and labeled as T-A, T-B, and T-C. Each tube was terminated with a 1½″ mini *Conflat* flange at its top. T-A and T-B, which were positioned on the top and side of the beam line, respectively, were used to mount two rotary vacuum feedthroughs. T-C was used to mount a mini *Conflat* flange with electrical feedthroughs. Two 1.8° step motors A and B (Applied Motion Products Inc., P/N 54092) were attached to the rotary feedthroughs through supporting frames. The driving shaft of each motor was mechanically coupled to the shaft of the corresponding vacuum feedthrough. A 1.6 mm diameter stainless steel wire probe was attached to the end of the extended shaft of each feedthrough and offset from its axis with a small ceramic tube. These two wire probes, A and B, were used to detect the ion beam profiles along the horizontal and vertical directions, and were wired to two separate electrical feedthroughs on T-C. The offset distance of probe A (probe B) from the axis was set to be 25.8 mm (25 mm) which is greater than the maximum possible half width (height) of the ion beam.

Each of the motors was driven separately by a step motor driver (Applied Motion Products, Model 2035). Figure 3.10 is a sketch of the motor driver. The two drivers were powered by a common 12 VDC power supply. The four lead wires on a motor were connected to the motor connectors on its driver. The logic inputs of the drivers (*STEP, DIRection*, and *ENable*) were connected to appropriate digital output channels on a National Instrument Data Acquisition (DAQ) board installed in a PC. The "Full/Half Step" switches on the drivers were set to "Half" position. Therefore, the actual step angle was 0.9° instead of 1.8° for both motors.

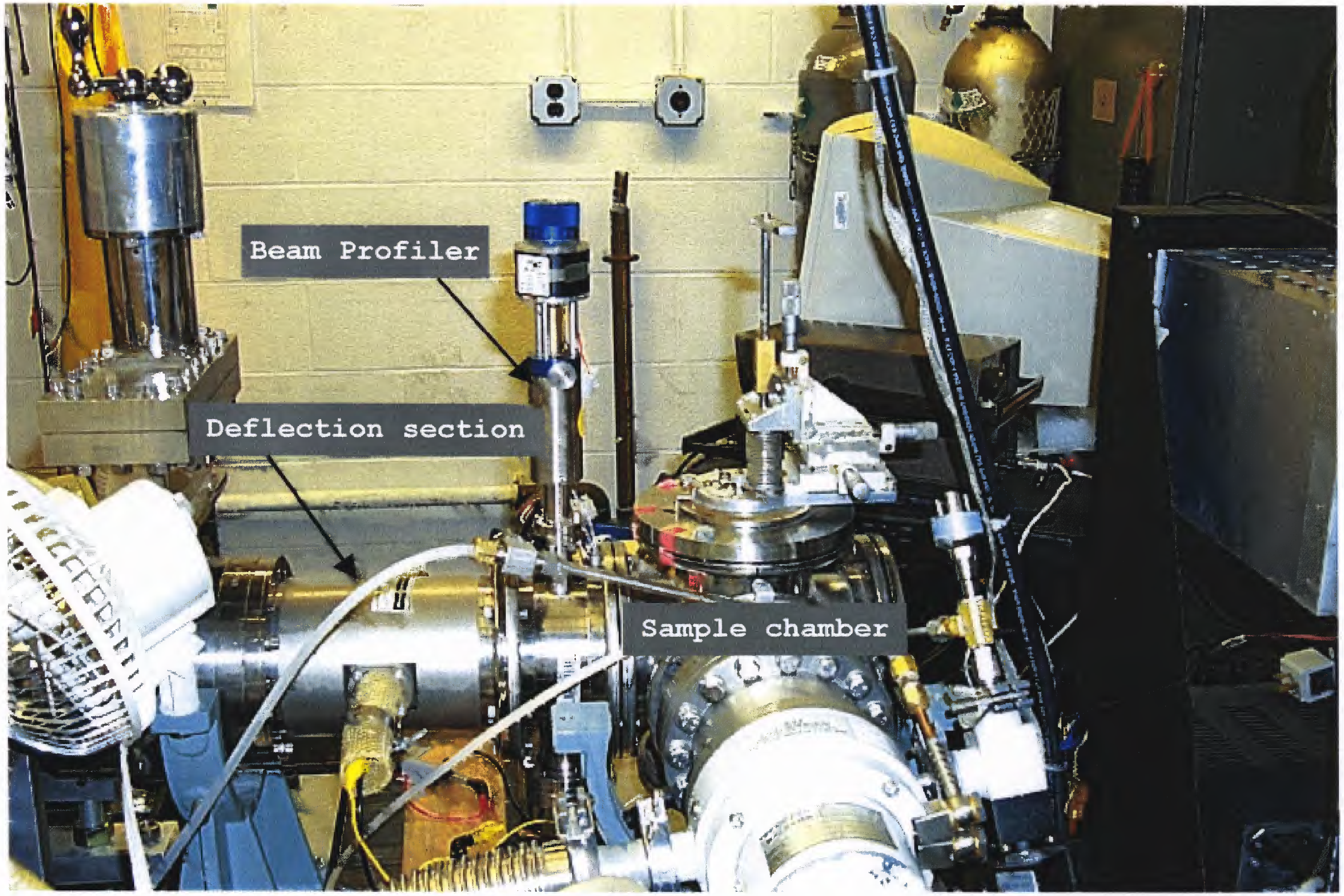

Figure 3.8 A beam profiler for automatic ion beam profiling was designed, constructed and mounted between the deflection section and the sample chamber, as part of the dissertation study.

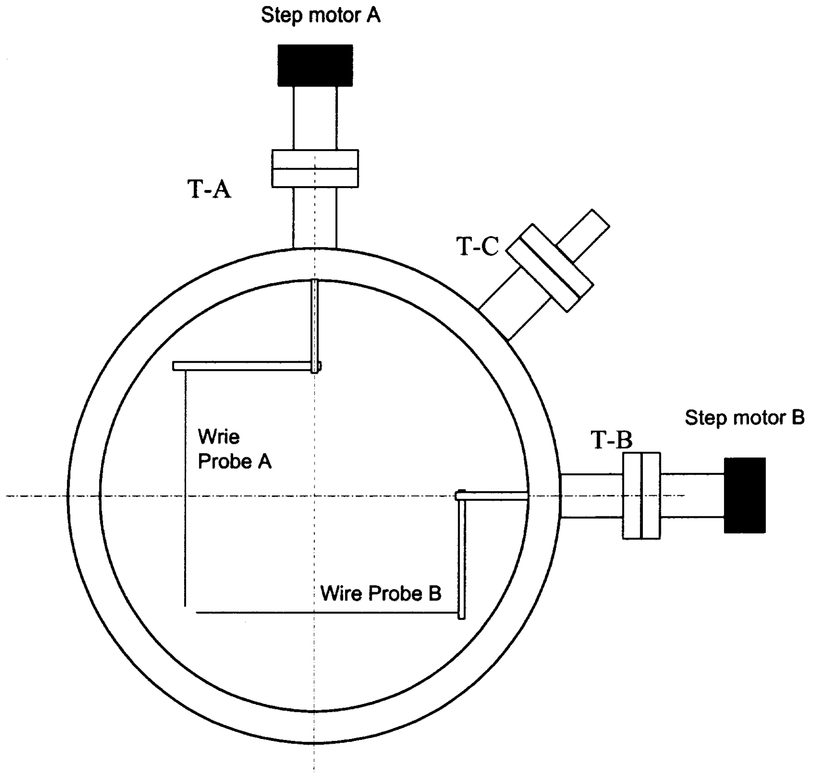

Figure 3.9 A schematic drawing of the beam profiler (side view).

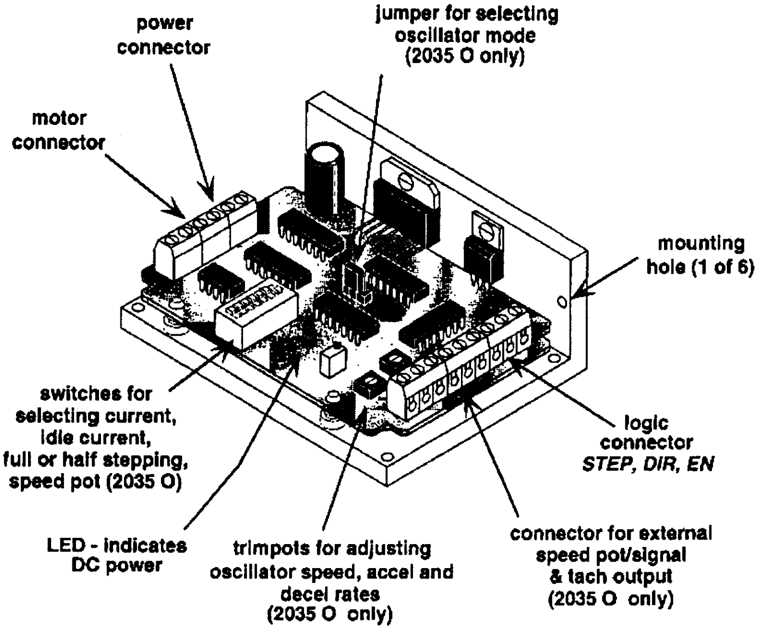

Figure 3.10 A sketch of the step motor driver [57]. The logic input signals (STEP, DIR, and EN) are provided by a Data Acquisition board controlled by the LabVIEW program.

3.2.2 Operation and Control of the Profiler

During an automatic beam profiling process with the beam profiler, the motors (and attached wire probes) are driven in a controlled sequence and the beam currents are measured by the probes at each circular position. The motor control and data acquisition system was built around a PC equipped with a Data Acquisition (DAQ) board and running LabVIEW software. Figure 3.11 is the system block diagram. A LabVIEW program, which is described in detail in the following sections, provides the user with the control interface. This program used various built-in functions to communicate with the DAQ board to send/receive digital/analog I/O signals. The motor drivers receive control signals, which drive the motor and specify the rotation direction of the motor (clockwise or counterclockwise), from the program via digital output channels on the DAQ board. The rotation of a motor caused its attached wire probe to move in a circular path. The angular position of the probe (or its projected position on the X-Y plane perpendicular to the beamline) was calculated by the program and used as the x-axis of a "Position vs. Ion Current" graph. The ion current measured on the wire probe was sent to a Keithley 485 picoammeter via a coaxial cable that was connected to an electrical feedthrough on T-C in Figure 3.9. The picoammeter provided a DC voltage output signal proportional to the input ion current. The proportionality factor was calibrated for each measurement range on the picommeter. The voltage from the picommeter was fed to an analog input channel of the DAQ board and converted into current values in the control program based on the proportionality factor. Two picoammeters were used, one for each wire probe.

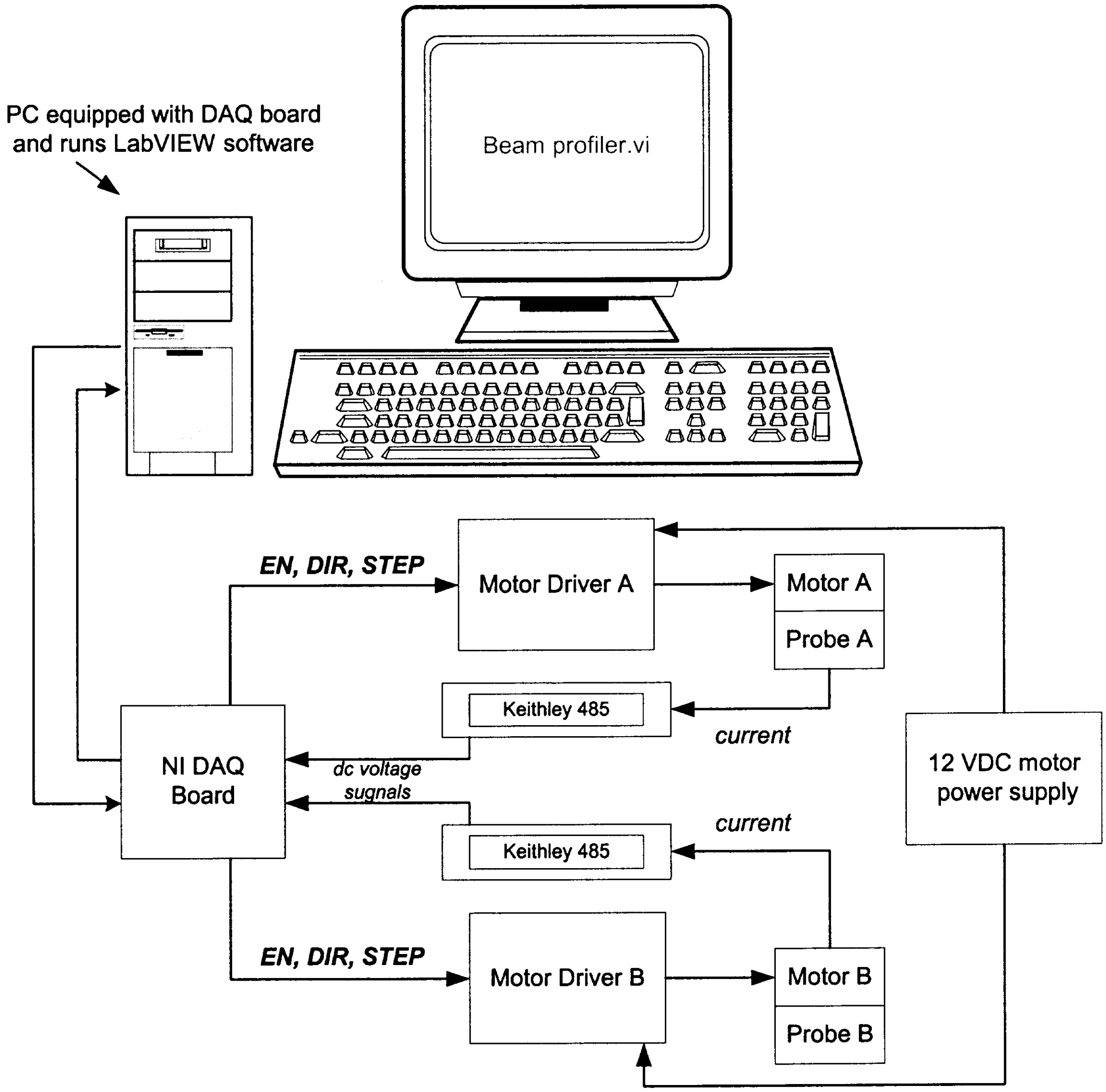

Figure 3.11 Block diagram of the control and data acquisition system of the beam profiler. It was built around a PC that was equipped with a NI DAQ board and runs LabVIEW software.

3.2.3 The LabVIEW Control Program

3.2.3.1 Introduction to Programming with LabVIEW. LabVIEW is short for **Lab**oratory **V**irtual **I**nstrument **E**ngineering **W**orkbench. It is a powerful and flexible instrumentation and analysis software development application released by National Instruments. It is different from text-based programming languages in that LabVIEW uses a graphical programming language, known as the G programming, to describe programming actions. Since LabVIEW employs terminology familiar to scientists and engineers and the graphical objects used to construct the programs are easily visualized, it provides a simple and straightforward methodology for data acquisition, analysis and instrument control from a PC. In LabVIEW, programs are called Virtual Instruments (VIs) since they have the look and feel of physical systems or instruments [58]. A LabVIEW VI is comprised of two windows, the front panel window and a block diagram window. The front panel is the VI user interface that allows interactive control of the program, while the block diagram window contains the source code represented in a graphic form (such as icons, wires, etc.).

The front panel of a VI is a combination of controls and indicators. Controls simulate the types of input devices one might find on a conventional instrument (such as knobs, switches or buttons, slides, digital control, etc.) and provide a mechanism to forward input from the front panel to the program. Indicators, on the other hand, provide a way to display data originating in the program back on the front panel. Indicators include various kinds of charts and graphs, as well as numeric, Boolean, and string displays. Controls and indicators are placed on the front panel by selecting and "dropping" desired objects from the *Control* palette. The size, shape and position of an object already on the front panel can easily be adjusted for better layout.

The block diagram of a VI looks like a computer program flowchart and corresponds to the code lines in a text-based program. In fact, the block diagram is the actual executable code. The block diagram consists of graphic components (objects) that perform specific functions ranging from simple arithmetic functions, to advanced data acquisition and analysis routines, and to file I/O operations, etc. Desired objects can be selected from the *Function* palette and dropped to the block diagram. The components of a block diagram belong to one the following three classes of objects:

- Nodes: Program execution elements.
- Terminals: Ports through which data passes between the block diagram and the front panel and between nodes of the block diagram.
- Wires: Data paths between terminals.

Programming a VI means selecting appropriate objects and wiring them together in the block diagram corresponding to the program execution flow. The desired execution flow is achieved by proper use of four flow structures in LabVIEW: the *For* loop, the *While* loop, the *Case* Structure, and the *Sequence* structure.

Since LabVIEW utilizes the art of modular programming of G language, a LabVIEW VI can be divided into a series of simpler subVIs that are analogous to subroutines. On the other hand, this VI could also be used as a subVI for another VI at a higher level. For example, in our LabVIEW program named " Beam Profiler.vi", various built-in DAQ functions (subVIs) were included to communicate with the DAQ board.

3.2.3.2 Front Panel of the Beam Profiling Virtual Instrument. Figure 3.12 shows the front panel of the beam-profiling VI program. The front panel can be used to preset the process parameters or dynamically change some parameters during the process, to monitor the process values and to display the beam profiles. Each object on the front panel was labeled to describe its specific function so that even the first time user can quickly learn how to handle it. Several controls common to both motors are on the top portion of the panel:

- Display mode: This control object is used to specify the x-axis of the beam profiles displayed on the computer screen, as described above. Two options are " Angular" mode and "Projected" mode.
- Number of readings: This control is used to specify the number of sampled data that are used to calculate an averaged current reading at each angular position. The larger this number, the more accurate the current reading, but the longer the time required to complete the profiling.
- Step angle: This is the angle by which the motors rotate per step. This number is used to calculate the angular position of the moving probe. It should be set at 0.9 unless the step selection switches on the motor drivers are reset to "Full" positions. (See Figure 3.10)

There is an "Emergency Stop" button (large red button) at the top right corner of the front panel that is used to stop the running program and thus stop the rotating motor in case something goes wrong during the profiling process. Below the common control area, there are two groups of controls and indicators that are used to control individual motors, to display motor status and current reading on the corresponding probes. Since the appearances, layouts and tasks of the two groups are similar, only the objects of the top group labeled "Vertical Profiling" are described below:

- Angle position: this meter-like indicator displays the current angular position of the moving probe (probe B in case of vertical profiling). The value is calculated in the program based on the step angle setting and the actual number of steps executed.
- Current reading: indicates the current value measured by the probe at a step.
- Rotation radius: this control sets the probe rotation radius that is used by the program to convert the angular position to projected position. The rotation radius was obtained by measuring the offset distance of the probe from the motor axis and should be modified only when the position of the probe wire is changed.
- Rotation speed: although named as "speed", this control actually sets a dimensionless number that divides a time constant (1000 ms) and specifies the waiting time between two motor steps. Therefore, the larger this "speed" number, the shorter the waiting time and the faster the motor moves. Its value can be preset or adjusted while the program is running either by dragging the horizontal slide or by entering a desired value in the digital display above its label.
- Range selector: It is essential that the selection on this control is the same as the range selected on the Keithley picoammeter. Depending on the selections of the range, the program uses a proportionality factor to convert the voltage input on the DAQ board to a current value measured by the picoammeter.
- File path: specifies the path (name) of a file that is used to store the beam profile data (angular/projected positions and current values). If no file is specified in this control, the program will pop up a dialogue window when the motor stops, asking the user if

the data needs to be stored or not. At the same time, a current vs. position graph is displayed on the X-Y graph type indicator below the “File path” control.

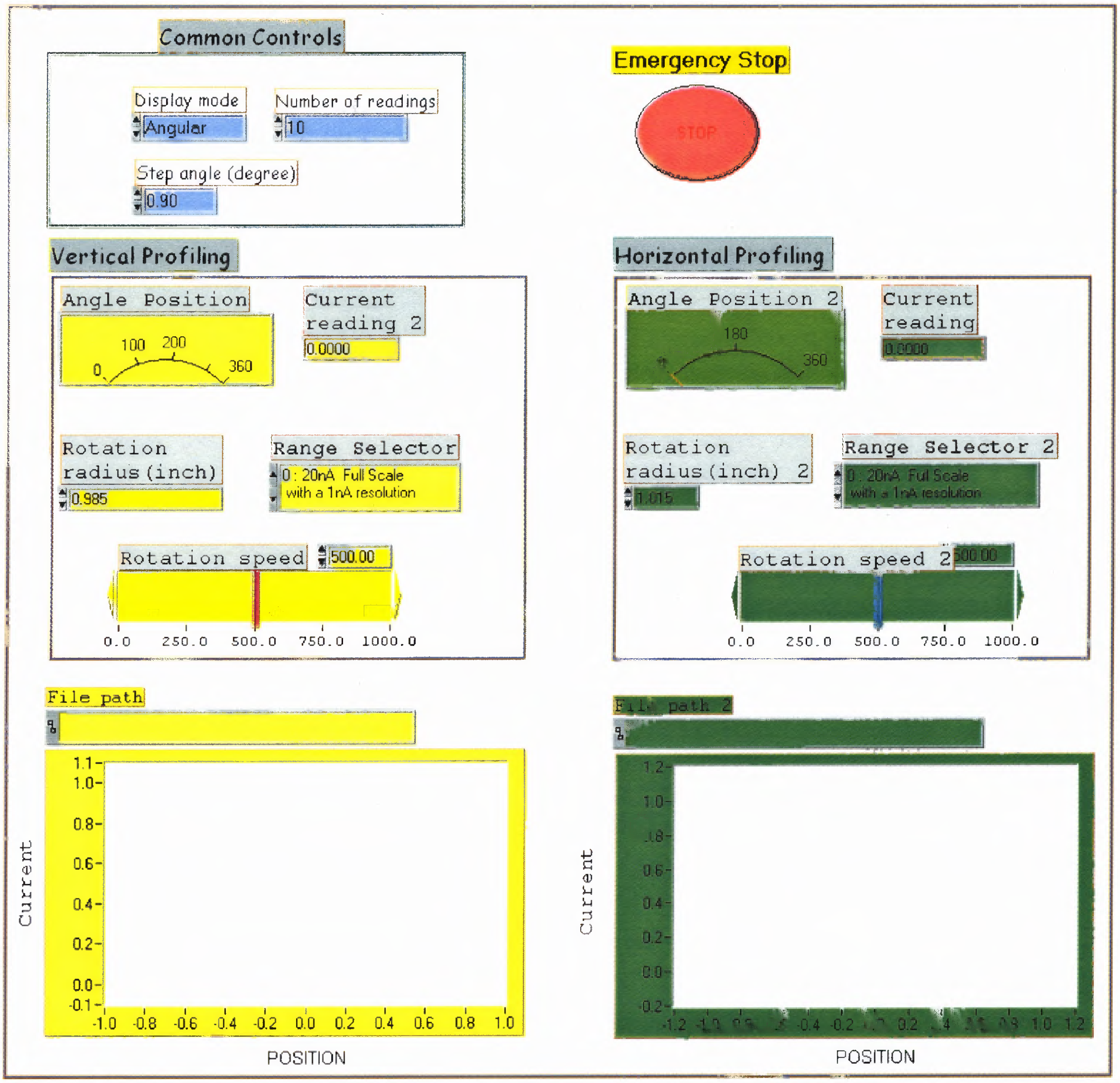

Display mode: Angular

Number of readings: 10

Step angle (degree): 0.90

Current reading 2: 0.0000

Rotation radius (inch): 0.985

Range Selector: 0: 20nA Full Scale with a 1nA resolution

Rotation speed: 500.00

Current reading: 0.0000

Rotation radius (inch) 2: 1.015

Range Selector 2: 0: 20nA Full Scale with a 1nA resolution

Rotation speed 2: 500.00

Figure 3.12 Front panel of the LabVIEW program for ion beam profiling.

3.2.3.3 Execution Order of the Control Program. The program was designed to execute in the following order to complete a beam profiling process:

1. Vertical profiling: The program sends signals to drive Probe B to rotate a full circle (360°) from its zero position. The rotation direction can be predefined by the user in the block diagram. While the probe is rotating, its position values and the current values at each position are displayed on indicators on the front panel and stored into two arrays. When the probe stops after finishing a full circle, the vertical beam profile is displayed on the screen and all data are stored into a spreadsheet file for future analysis.
2. Horizontal profiling: Probe A is driven to rotate a full circle to obtain beam profile along horizontal direction. The rotation direction is set to be counterclockwise if seeing from above the beamline. The display and storage of data and display of the profile graph are similar to those described above.
3. Probe A is driven to rotate in an opposite position to its original position.
4. Probe B is driven to rotate in an opposite position to its original position.

3.2.3.4 Block Diagram of the Virtual Instrument. Based on the execution order, described in the previous section, the block diagram of the beam profiling VI was constructed utilizing a *Sequence* structure that has four subdiagrams looking like frames of a film (numbered as frame 0, 1 …3), as shown in Figure 3.13. The subdiagrams are executed sequentially and each of them carries one of the 4 tasks described above. Outside the *Sequence* structure is a LabVIEW built-in function " Write to digital line" that is used to enable both motors at the beginning of the program. Figure 3.13 shows only the first subdigram corresponding to "vertical profiling" and its components. Inside this subdiagram is a *While* loop that executes the graphical codes inside it until the loop is iterated for 400 times. During each loop, motor B rotates by 0.9° and the current measured on probe B is read by the program. After 400 iterations, motor B rotates by $400 \times 0.9° = 360°$ and all temporarily stored data are sent to the X-Y graph indicator and the "Write to a spreadsheet" function that are located outside the loop structure. For the purpose of easy understanding and better visualization, some parts of the execution codes inside the loop are represented by several nodes. These nodes are saved as subVIs that are called when the main VI is running. Functions carried by these subVIs or built-in functions, shown in the diagram in Figure 3.14, are briefly described below,

- Node 2 - Reading.vi : Get current value drives the motor to rotate by 1 step.
- Node 3 - Range.vi : Scale the current value to match the range selected on the Keithley picoammeter.
- Node 2 - reading.vi : Get angular or projected position value.
- Write to Digital Line.vi: Set the motor rotating direction.

The block diagram can be easily edited to meet specific requirements under different situations. For example, the execution order can be changed so that the horizontal profile is measured first or the probe B returns back before probe A does. This is accomplished by simply clicking on the border of a sequence frame and assigning it a new frame number corresponding to its desired position in the new execution order. Or the loop iteration conditional value can be changed so as to have the probes rotate only a half circle. When making any changes in the block diagram, it is important to ensure that two probes would not collide with each other.

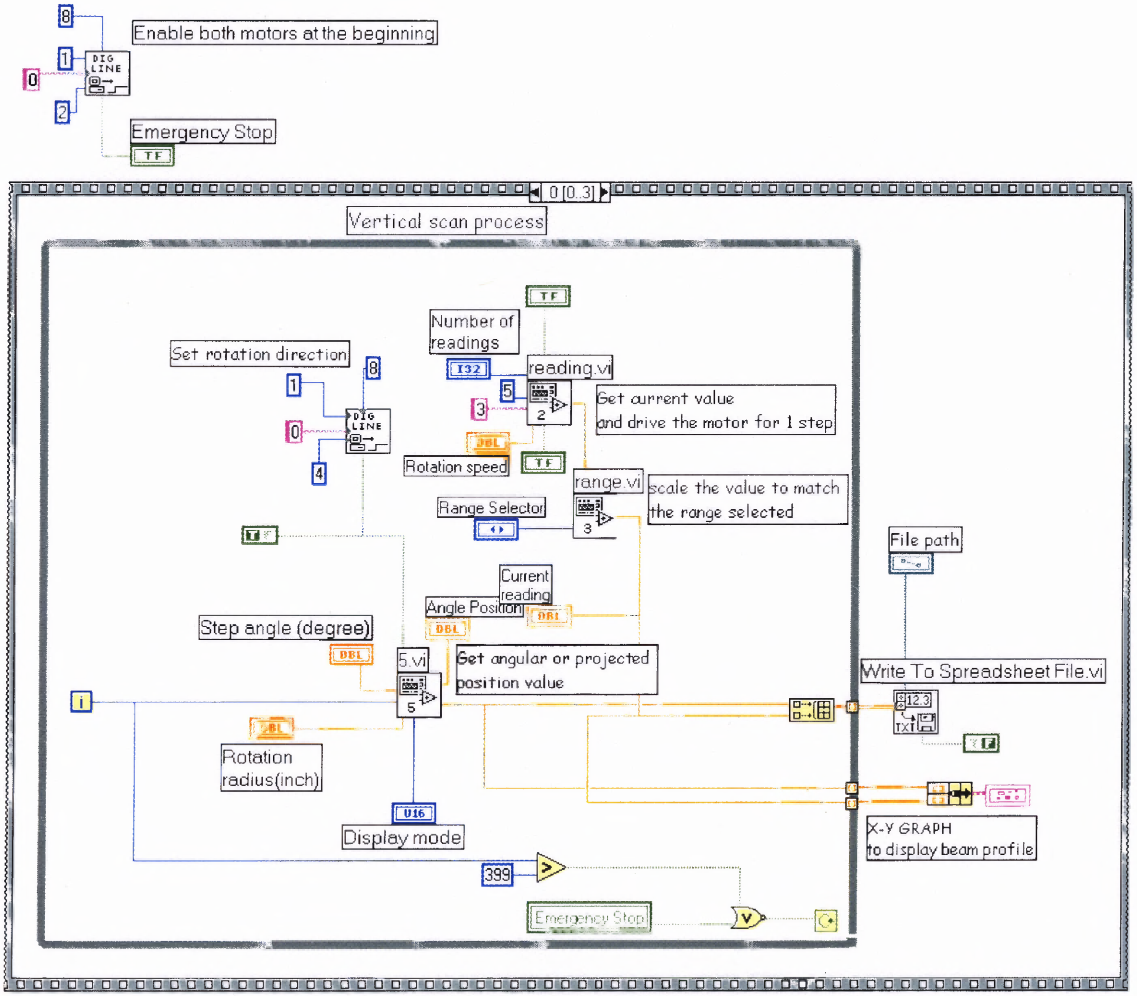

Figure 3.13 The block diagram of the beam profiling VI file. Only the first sequence is shown here that is executed to drive probe B to turn a full circle to obtain the vertical distribution of the ion beam.

3.2.4 Results Obtained with the Beam Profiler

As compared to the manual profiling method that is described in Section 2.4.3, the use of the beam profiler provides a faster and easier way to find the optimum operating conditions of the system. A beam profiling process using the beam profiler typically takes less than 2 minutes. Therefore, the beam profiler can also be used to check the beam uniformity during prolonged implantation processes, which is impossible with manual measurements. In addition, an automatically obtained beam profile is more accurate than that obtained manually since the former has much more data points (400 for a 360° rotation). Furthermore, since the probe rotates in a circular path instead of moving in a plane, the beam profiles can be used to tell whether the beam is convergent or divergent before it reaches the sample. The beam profiler has been extensively used for general system adjustment, finding of best operating conditions before implantation, and process monitoring during implantation. Figure 3.14 shows typical Ar^+ beam profiles (horizontal and vertical) obtained using the beam profiler.

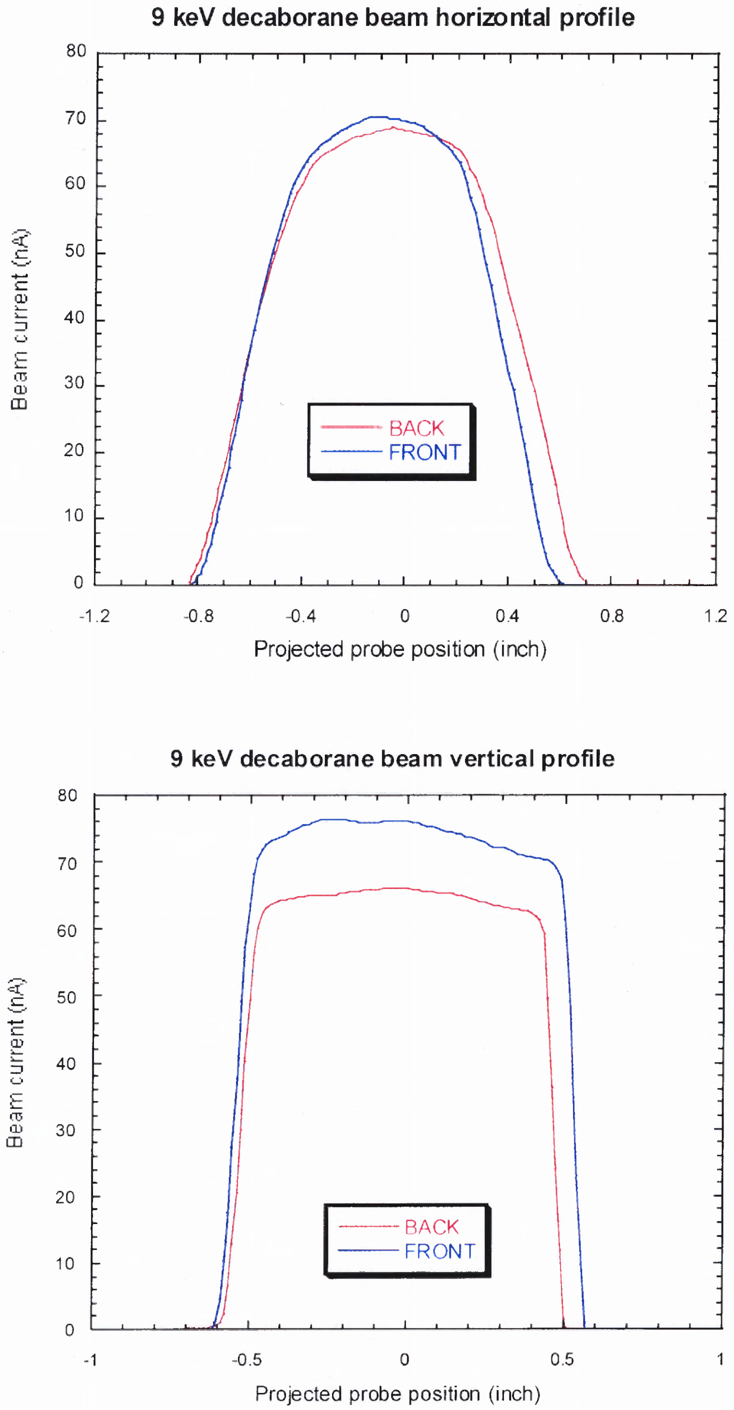

Figure 3.14 The horizontal profile (top) and vertical profile (bottom) of a 9 keV Ar^+ ion beam measured with the beam profiler.

CHAPTER 4

CHARACTERIZATION TECHNIQUES

4.1 Introduction to Secondary Ion Mass Spectrometry

Secondary ion mass spectrometry (SIMS) is a surface analysis technique widely used for the chemical characterization of organic and semiconductor surfaces. The basis of the technique, as well as its fundamental limitation, is the requirement for bombardment of the material to be analyzed, in vacuum, with an energetic (keV) primary ion beam followed by mass spectrometry of the emitted secondary ions. Primary beam species useful in SIMS include Ar^+, O_2^+, Ga^+ or Cs^+ at energies between 1 and 30 keV. The SIMS primary ion beam can be focused to less than 1 μm in diameter. As shown schematically in Figure 4.1, the bombarding primary ion beam produces monatomic and polyatomic particles of sample material (M) and the characteristic sputtered secondary ions (M^+, M^-) that give information on composition of the sample [59]. The secondary particles carry negative, positive, and neutral charges and they have kinetic energies that range from zero to several hundred eV. Typical SIMS sputter yields fall in a range from 5 and 15. Sputter rates in typical SIMS experiments vary between 0.5 and 5 nm/s and depend on primary beam intensity, sample material, crystal orientation and the intended analysis [60].

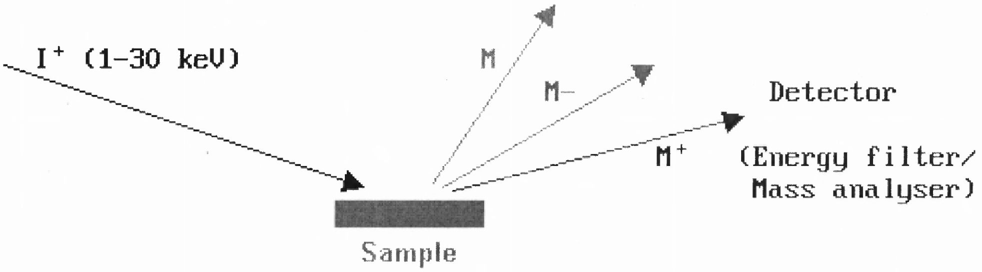

Figure 4.1 In SIMS the surface of the sample is subjected to bombardment by high energy ions, which leads to the ejection (or *sputtering*) of both neutral and charged species from the surface [59].

The basic SIMS system consists of: an ion gun to provide a source of primary ions, a mass spectrometer with which to detect the secondary ions, a data acquisition system, and a vacuum environment in which to house the ion gun and mass spectrometer [61].

There are two basic variants of the SIMS technique: static SIMS and dynamic SIMS. They are based on the same physical process described earlier. When the sputtering rate is extremely low, the entire analysis can be performed while consuming less than a tenth of an atomic monolayer. This slow sputtering mode is called static SIMS. In static SIMS the aim is to obtain sufficient signal to provide compositional analysis of the surface layer without actually removing a significant fraction of a monolayer (about 10% of a monolayer for a $1 cm^2$ sample).

Dynamic SIMS, on the other hand, is mainly used for depth profiling. In dynamics SIMS, the sample surface is slowly sputtered away. Continuous monitoring the secondary ion count rate of selected elements as a function of time leads to depth profiles. To convert the time into depth, a profilometer is used, after the sputter analysis process, to measure the sputter crater depth by dragging a stylus across the crater and noting vertical deflections. Total crater depth divided by total sputter time provides the average sputter rate. The ion counts are converted into element concentrations by using a Relative Sensitivity Factor (RSF). Quantitative SIMS analysis requires standard materials from which the RSF value is measured. Because ion yields depend on the analyzed element, the sputtering species, and the sample matrix, separate RSF values must be measured for each element. Depth resolution depends on the flatness of crater bottom. Modern instruments provide uniform sputter currents by sweeping a finely focused primary beam in a raster pattern over a square area. In some instruments, apertures select secondary ions from the crater bottoms, but not the edges. Alternatively, the data processing system ignores all secondary ions produced when the primary sputter beam is at the ends of its raster pattern [60].

Since the SIMS technique itself relies upon the removal of atoms from the surface, it is by its very nature a destructive technique. One of the main advantages that SIMS offers over other depth profiling techniques (e.g. Auger depth profiling) is its sensitivity to very low concentrations (~ ppm) of elements. This is particularly important in the semiconductor industry where dopants are often present at very low concentrations. The depth resolution achievable (e.g., the ability to discriminate between atoms in adjacent thin layers) is dependent upon a number of factors that include:

1. the uniformity of etching by the incident ion beam,
2. the absolute depth below the original surface to which etching has already been carried out,
3. the nature of the ion beam utilized (i.e. the species & energy of the ions),

as well as effects related to the physics of the sputtering process itself (e.g., ion-impact induced burial) [59].

Dynamic SIMS can also be used to obtain compositional images of a surface formed from the spatial variations of the secondary ion currents across the surface. This type of application is termed as imaging SIMS or ion imaging. The main problem in imaging SIMS is to ensure that sufficient signal is obtained at the desired spatial resolution whilst minimizing the ion flux incident on any part of the surface. This is most easily achieved by switching from the traditional approach of using continuous-flux ion guns and quadrupole mass spectrometer detectors, to using pulsed ion sources and time-of-flight (TOF) mass spectrometers. The TOF mass spectrometers are a much more efficient way of acquiring spectral data, and also provide good resolution and sensitivity up to very high masses. Using such instruments, SIMS images with a spatial resolution of better than 50 nm are obtainable.

Dynamic SIMS technique has been used in this dissertation work to obtain the depth profiles of B and H in decaborane implanted Si samples and to characterize transient enhanced diffusion of B dopant in Si implanted with decaborane and B^+ implants. Details regarding these analyses are described in Chapter 5.

4.2 Principles of Rutherford Backscattering Spectroscopy

Rutherford Backscattering Spectroscopy (RBS) has long been used for surface analysis by nuclear physicists, since it provides a quick and simple method of examining target purity and thickness in nuclear physics experiments [62]. The growing need for surface analysis in many areas of material science has prompted the development and use of RBS in many surface/thin film oriented research studies. Many accelerators in the energy range of 1 to 3 MeV, that were previously used for nuclear physics, are now used for solid state analysis by RBS. The electronic industry have provided the largest driving force for the development of the technique, with their requirements for detailed information on shallow doped layers in semiconductors and on metal-semiconductor contact, thin film compositions and layer thickness, etc. The operational principles of RBS are simple to follow. A beam of energetic ions such as He^+ in the MeV energy range is directed at a sample. Due to the elastic collisions of the He ion nucleus with the nuclei of the sample atoms, some of the projectiles will be scattered back at energies characteristic of the scattering element mass and depth. These backscattered particles are collected by a solid state detector that counts the number of scattered particles and measures their energies.

The energy loss for a backscattered ion depends on the mass(es) of the target atom(s) and the depth it travels to within the target. Given the initial energy of the projectiles, the energy of the backscattered ions can be calculated from collision kinematics for the specific elements that are present in the sample. The concentration of an element in the sample can be determined from the number of counts of its corresponding peak in the backscattered ion energy spectrum by comparing to spectrum of a standard sample or from computer simulation. The deeper an ion penetrates into the target, the more energy it loses when it is backscattered. Therefore, a single RBS spectrum can provide both mass identification and the depth distribution of these elements. The combination of RBS and channeling can provide data on the degree of disorder within a crystal and the lattice position of impurities within the lattice. This combination of techniques was used extensively to characterize the lattice location and lattice disorder following the initial development work on ion implantation into silicon in the 1960s.

A schematic of typical configuration in RBS is shown in Figure 4.2. A high-energy beam, typically 2 MeV He^+, is extracted from an accelerator and passed through a magnetic analyzer. The beam is then collimated and directed onto the target in a target chamber in which the pressure is usually kept below 10^{-6} torr. The scattered particles are detected by solid state detectors and energy analyzed and counted. Solid state detectors are commonly used since they detect particles of all energies simultaneously. In a typical experimental arrangement a silicon surface barrier detector is placed at a backscattering angle of ~ 170° and a distance ~ 15 cm from the target. The angular spread of the beam at the detector can be reduced by placing slits in front of the detector to improve mass resolution if necessary. The initial stage of the electronic system is a charge-sensitive preamplifier, which provides a minimum of pulse shaping but gives a maximum signal-to-noise ratio. The subsequent main amplifier creates a suitable pulse shape to optimize resolution and count-rate capability. Data acquisition, storage and display are usually provided by a multi-channel analyzer (MCA). The desired RBS spectrum is accumulated by measuring the amplitude of each pulse (caused by a scattered particle striking the detector) and storing it at an appropriate channel address (or channel number) that is proportional to the energy of the scattered particle. Information contained in a RBS measurement can be best fitted by computer simulation by means of adjusting the parameters associated with the simulated structure to optimize the fit between the simulated and measured spectra. RUMP is a well-established RBS analysis computer program package developed by Doolittle *et al* at Cornell University, which provides comprehensive analysis and simulation of RBS spectra [63]. It has been used for RBS spectra analysis in the current work in order to determine the Si sputtered yields by decaborane cluster ions. The details are given in Section 6.1.

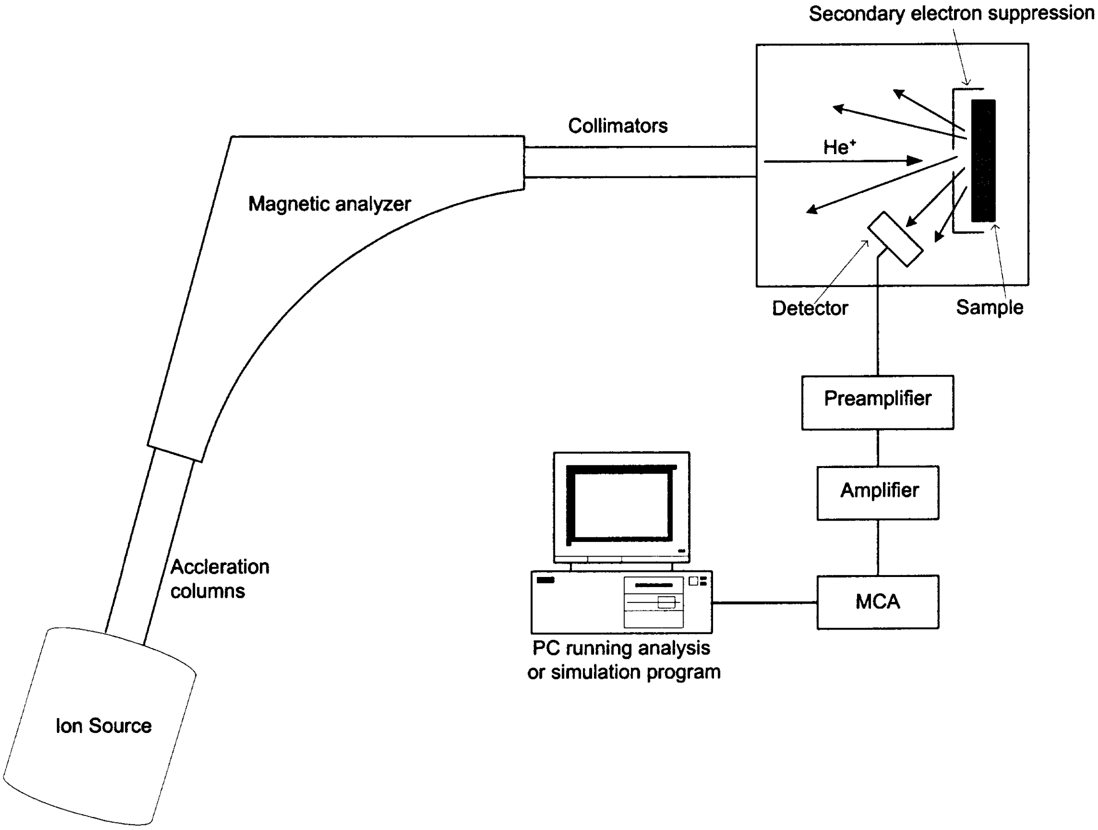

Figure 4.2 Typical configuration of a Rutherford Backscattering Spectroscopy facility.

4.3 Principles of Atomic Force Microscopy

Atomic force microscopy (AFM) is one of the most advanced and widely used techniques for surface characterization of materials. The development of AFM followed the development of the Scanning Tunneling Microscope (STM). Although the STM can provide sub-angstrom resolution in all three dimensions, it is limited to conductive and semiconductor samples. AFM, in contrast, can generate 3-D topography on insulators and conductors for area up to 100 μm × 100 μm. It has 2 ~ 10 nm lateral resolution and ~ 0.1 nm vertical resolution. With AFM, little or no sample preparation is required and samples can be tested in ambient air, in liquid or in vacuum, if needed. Figure 4.3 shows the basic configuration of the Digital Instrument NanoScopeIIIa® AFM at NJIT.

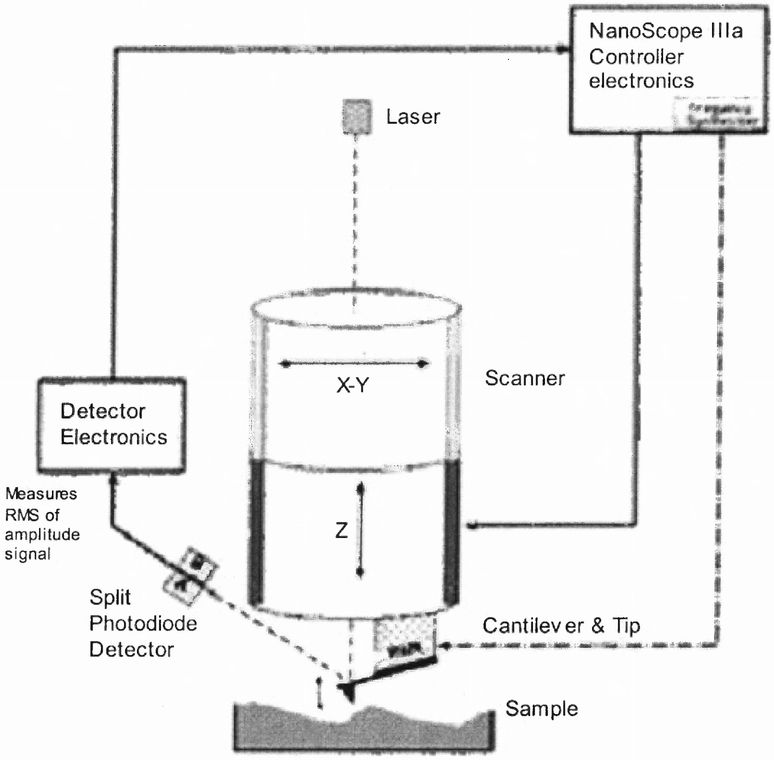

Figure 4.3 Basic configuration of the DI NanoScopeIIIa® AFM at NJIT [64].

The name of AFM is based on the fact that the most commonly utilized tip-sample interaction is an interatomic force called *van der Waals* force. In an AFM measurement, the sample surface is scanned by a microscopic sharp tip attached to the free end of a minute cantilever. The movement of the tip or sample is performed by an extremely precise positioning device made from piezo-electric ceramics, most often in the form of a tube scanner. The scanner is capable of sub-angstrom resolution in x-, y- and z-directions. The z-axis is conventionally perpendicular to the sample. Due to sample surface features, the variation of tip-sample interaction causes changes in the cantilever deflection or oscillation amplitude. The changes are sensed by a laser beam deflection system. The light from the laser is reflected from the tip end of the cantilever onto the split photo-diode. By measuring the split photo-diode difference signal, changes in the bending of the cantilever can be measured. Three dimensional topographical maps of the surface are then constructed by plotting the local sample height versus horizontal probe tip position. The image contrast can be achieved in many ways. The three main AFM measurement modes are contact mode, tapping mode and non-contact mode.

In contact mode, the probe is scanned across a sample surface while monitoring the change in cantilever deflection with the split photodiode detector. A feedback loop maintains a constant cantilever deflection by vertically moving the scanner. The distance the scanner moves vertically at each x-y data point is stored by the computer to form the topographic image of the sample surface. As the name suggests, the tip and sample remain in close contact as the scanning proceeds. One of the drawbacks of remaining in contact with the sample is that there exist large lateral forces on the sample as the tip is "dragged" over the specimen. These extra forces can distort measurement data and cause severe damage to the sample, including movement or tearing of surface features.

Tapping mode is the next most common mode used in AFM. When operated in gas or vacuum, the cantilever is oscillated at its resonant frequency (often hundreds of kilohertz) and positioned above the surface so that it only lightly “taps” on the surface for a very small fraction of its oscillation period. The laser deflection system detects the amplitude of cantilever oscillation. A feedback loop maintains a constant oscillation amplitude by moving the scanner vertically at every (x, y) position. Recording this movement forms the topographical image. Although contact with the sample still exist, the very short time over which this contact occurs means that lateral forces are dramatically reduced as the tip scans over the surface. When imaging poorly immobilized or soft samples, the tapping mode may be a far better choice than the contact mode for imaging [65].

Non-contact operation is another method that may be employed when imaging by AFM. The probe is held a small distance above the sample. Attractive *Van der Waals* forces acting between the tip and the sample are detected, and topographic images are constructed by scanning the tip above the surface. This is a very difficult mode to operate in ambient conditions with the AFM. It provides substantially lower resolution than either contact or tapping mode, and may also result in unusable data and sample damage.

Tapping mode AFM has been utilized in the dissertation research to characterize the effect of irradiation of decaborane cluster ions on various surfaces. The details are described in section 6.2.

CHAPTER 5

THE EFFECTS OF DECABORANE IMPLANTATION IN SILICON

5.1 Transient Enhanced Diffusion of Boron in Silicon

The final depth profiles of B in Si may be defined as much by the projected range as by diffusion during dopant activation annealing. In the case of shallow B-doped junctions, the critical phenomenon is transient enhanced diffusion (TED), which may exceed equilibrium diffusion by orders of magnitude. Therefore, in assessing the potential application of decaborane for ultra shallow junction formation, it is essential that TED associated with cluster ions is at least no larger than for the case of B^+ ions.

5.1.1 Experimental Procedures

Si samples with epitaxial embedded B marker layers were used to measure enhanced boron diffusion and Si self-interstitial induced by a near surface implant. This allows spatially separating implanted species from diffusing species that can be profiled away from the surface [66]. Boron doping superlattices (B-DSLs) were grown in Si by low temperature molecular beam epitaxy (MBE) at Bell Laboratories, Lucent Technologies. The superlattices consisted of six 10-nm wide layers doped with B concentration of 2×10^{18} cm^{-3} spaced 100 nm apart in undoped Si crystal, as shown in Figure 5.1. All experiments described thereafter in this section were performed with these superlattices.

To investigate the dependence of boron TED on the incident ion energy, three samples were implanted with $B_{10}H_x^+$ at 12 keV, 5 keV and 2 keV. To verify that TED associated with cluster ion implantation is no more pronounced than for monomer ion implantation, B implantation was carried out with 1.2 keV B^+ ions to the same B dose as

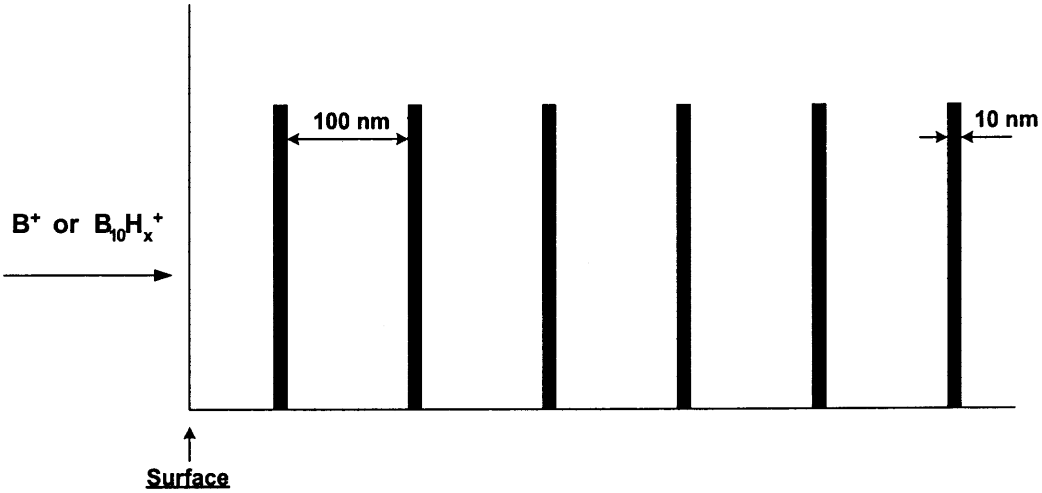

Figure 5.1 Schematic drawing of the B-DSL structure in the samples for TED experiments.

with $B_{10}H_x^+$ cluster ions. The B^+ ion beam was obtained through electron impact ionization of BF_3 gas, as described in Section 2.2. Before implantation, all four samples were treated with buffered HF acid for 60 seconds, to remove the native oxide, and then loaded into the implantation system. Since the samples were too small to be held with spring clips, silicon grease applied to the backside of the sample was used to mount the sample onto the sample block. Each sample was mounted on the sample block in such away that its bottom edge was at the center of the implantation region and was bordered by a regular p-type Si sample that was used for dose measurement by Nuclear Reaction Analysis. The nominal implantation dose was determined by ion current integration as described in Section 2.2.1.

The four implanted samples were soaked in trichloroethylene for 5 minutes, followed by rinsing with acetone, methanol and finally de-ionized (DI) water. The purpose of this procedure is to totally remove the silicone grease on the backside of the sample. The samples, together with an unimplanted control sample, were then cleaned with a standard "P-clean" process as follows [31]: the samples were dipped in 1:1

solution of sulfuric acid and hydrogen peroxide for 5 minutes, rinsed with DI water three times, and finally dried by high-purity nitrogen gas. All these samples were then subjected to rapid thermal annealing under the same condition (850 °C, 15 min, in flowing Ar gas ambient). Table 5.1 shows the experimental conditions for all TED samples.

After the annealing step, SIMS analysis was performed on these samples to obtain the depth profiles of the B marker layers. An unimplanted/unannealed B-DSL sample was also tested as a reference. This analysis used 3.0 keV O_2^+ primary ions at 60° incident angle and had a detection limit of 3×10^{15} B/cm^2. By comparison of the SIMS depth profiles on different samples, the broadening of B marker layers due to B transient enhanced diffusion can be clearly shown and the enhancement of B diffusivity can be extracted from SIMS measurement data. Details are described in the following section.

Table 5.1 Experimental Conditions for TED Samples

Sample Number	Ion Species	Ion Energy (keV)	Actual Dose (B/cm^2)	Rapid Thermal Annealing
A121	$B_{10}H_x^+$	5	1.0×10^{14}	850 °C, 15 min.
A122	$B_{10}H_x^+$	12	1.3×10^{14}	850 °C, 15 min.
A221	No implantation / No annealing			
A222	No implantation			850 °C, 15 min.
A321	$B_{10}H_x^+$	2	7.1×10^{13}	850 °C, 15 min.
A322	B^+	1.2	1.2×10^{14}	850 °C, 15 min.

5.1.2 Results and Discussion

To extract the boron diffusion coefficients, each boron doping spike in the annealed samples was analyzed separately by comparing it with its corresponding counterpart in the unimplanted sample (control sample A221). In this way errors due to the slowly varying resolution of SIMS depths are avoided. The dopant diffusion is governed in this case by the one-dimensional diffusion equation:

$$\frac{dc}{dt} = \frac{d}{dz}\left(D\frac{dc}{dz}\right) \tag{5.1}$$

where z is the depth into the sample, c is the dopant volume concentration, and D is the diffusivity. The equation has an analytical solution:

$$c(z,t) = \frac{1}{2\sqrt{\pi Dt}}\int_{-\infty}^{\infty} c(\zeta,0)e^{-(z-\zeta)^2/4Dt}\,d\zeta \tag{5.2}$$

where $c(z,0)$ is the concentration at depth z before diffusion started, and $c(z,t)$ is the concentration at the same depth after diffusion for a time interval t. For the samples used in the TED measurements, the experimentally determined concentration $\hat{c}(z,0)$ and $\hat{c}(z,t)$ have the form of discrete data points, $\hat{c}_i(z_i,0)$ and $\hat{c}_i(z_i,t)$, $i = 1,2\ldots n$. The B diffusivity is given by [28]:

$$D_B = D_{B,x}[1 + \beta c(z)/n_i] \tag{5.3}$$

where n_i is the intrinsic carrier concentration and β is the enhancement factor. If $c(z) < ni$, $D_{B,int} = D_{B,x}\,[1+\beta]$ is called the intrinsic B diffusivity.

Equation (5.1) was solved numerically with the process simulator PROPHET, taking into account the concentration dependence of the diffusivity. An optimization routine was used for a best fit between the experimentally determined concentrations

$\hat{c}_i(z_i,t)$ and the output of the process simulator, $c_i(z_i,t)$. The residual vector was calculated with:

$$r_i = c_i(z_i, t) - \hat{c}_i(z_i - z_0, t) \tag{5.4}$$

and the norm $\|\mathbf{r}\|$ was minimized by varying $D_{B,int}$ and a parameter z_0 for each doping spike. The parameter z_0 serves to line up both depth profiles at exactly the same depth to prevent errors due to slightly varying SIMS depth scales [28].

Figure 5.2 shows the SIMS B profiles from two control samples A221 and A222. It can be seen that all six B doping spikes in sample A222 were broadened after annealing, due to the equilibrium boron diffusion in Si. From these profiles, the equilibrium boron diffusivity D_B^* for each doping spike was extracted by the method described above. The main sources of errors in extraction of diffusivity are: statistical fluctuations in the SIMS concentrations, errors in the depth scale due to varying sputter beam current, measurement errors in the determination of the crater depth, and variation in the Si deposition rate during MBE growth [67]. These errors have been estimated using a Monte-Carlo approach and the results are given as error bars in the subsequent figures.

For the implanted samples, only the second through sixth boron markers were used for TED analysis since the first doping spike was superimposed by the B implants. Figure 5.3 compares the depth profiles of boron marker layers in samples A122 and A322 that were implanted with 12 keV $B_{10}H_x^+$ cluster ions and 1.2 keV B^+ ions, respectively. It also shows the profiles for the unimplanted control sample A222. The implanted samples clearly show much wider B doping spikes than the control, indicating that there is transient enhanced diffusion from both boron and decaborane implants. It is also shown that TED from the 1.2 keV B^+ implanted sample is very similar to that from the 12 keV $B_{10}H_x^+$ implanted sample. For a quantitative analysis of each broadened peak in Figure 5.3, the time-averaged boron diffusivity, $\langle D_B \rangle$, and its error were extracted in a similar way as used to extract the equilibrium boron diffusivity D_B^*. The time-averaged enhancement in boron diffusivity, defined as $\langle D_B \rangle / D_B^*$, is taken as an indication of the extent of transient enhanced diffusion due to injection of excessive Si self-interstitials. Figure 5.4 shows $\langle D_B \rangle / D_B^*$ as a function of marker depth for both $B_{10}H_x^+$ and B^+ implants at equivalent B energy and dose. It was once suggested that decaborane implantation could suppress boron transient enhanced diffusion, possibly due to the surface amorphization effect by cluster ions [25]. The data shown in Figure 5.4, however, demonstrate that implantation with decaborane cluster ions leads to essentially the same amount of TED of B in Si as that in Si implanted with atomic boron ions of the equivalent energy and dose. This is in agreement with the results reported in a previous study where comparable boron diffusivity enhancements were observed from implantation of 5 keV $B_{10}H_x^+$ and 0.5 keV B^+ ions, although the ion beams were not mass-analyzed [27]. Furthermore, the finding is consistent with the so-called "+1 model" for TED, that is, the enhanced dopant diffusion is caused by the injection of excessive Si self-interstitials whose concentration is approximately equal to the number of implanted atoms that can become substitutional in the Si lattice site [29].

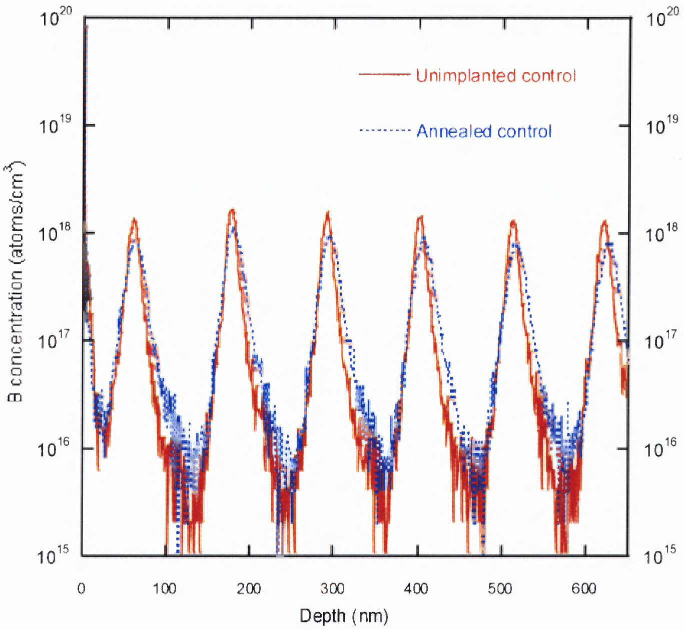

Figure 5.2 SIMS B depth profiles of two control samples A221 and A222. All six B doping spikes in sample A222 were broadened after annealing, due to the thermal equilibrium boron diffusion in Si.

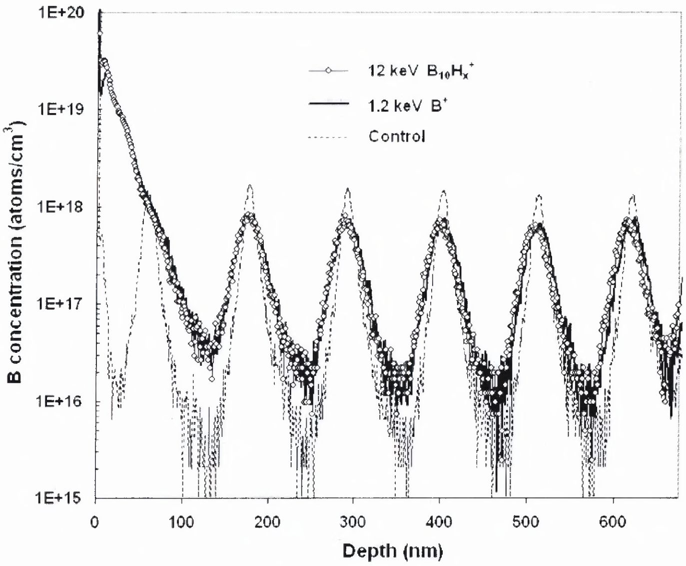

Figure 5.3 Depth profiles of boron marker layers in samples A122 and A322 that were implanted with 12 keV $B_{10}H_x^+$ cluster ions and 1.2 keV B^+ ions, respectively.

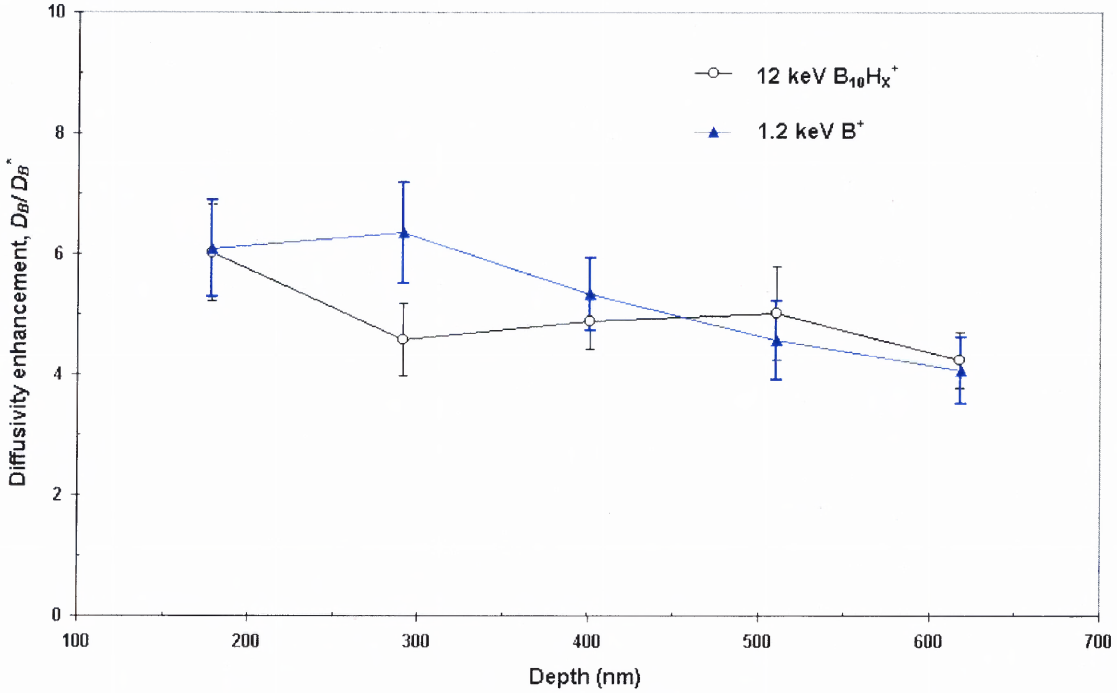

Figure 5.4 Comparison of boron diffusivity enhancements for the second through sixth B marker layers from samples implanted with 12 keV $B_{10}H_x^+$ cluster ions and 1.2 keV B^+ ions. The error bar for each marker layer was obtained from estimation using a Monte-Carlo approach.

Figure 5.5 compares the SIMS depth profiles of boron from the TED samples implanted with decaborane cluster ions at 12 keV, 5 keV and 2 keV. Although the profiles in the figure look similar for different energies, the differences in the amount of TED are indicated by quantitative analysis of diffusivity enhancement for each boron marker layer in these samples, as shown in Figure 5.6. The averaged boron diffusivity enhancement for $B_{10}H_x^+$ implants, calculated from the values of $\langle D_B \rangle / D_B^*$ for the five marker layers in consideration, are: 5.0 ± 0.3 for 12 keV, 3.8 ± 0.1 for 5 keV, and 3.0 ± 0.1 for 1.2 keV. The decrease of the amount of TED with decreasing ion energy, as shown in Figure 5.7, can be explained by the fact that TED is driven by the Si self-interstitials. The lower the ion energy is, the closer the implantation damage is to the surface. Since the Si surface under inert annealing conditions is a good sink for interstitials [27], the proximity to the surface means that more interstitials recombine at the surface. Provided that the annealing time is longer than the time for the interstitials to anneal out, the faster completion time leads to a smaller time-averaged diffusion enhancement [68]. These results also confirm a previous observation that implantation with lower cluster energy could reduce boron TED in Si [26].

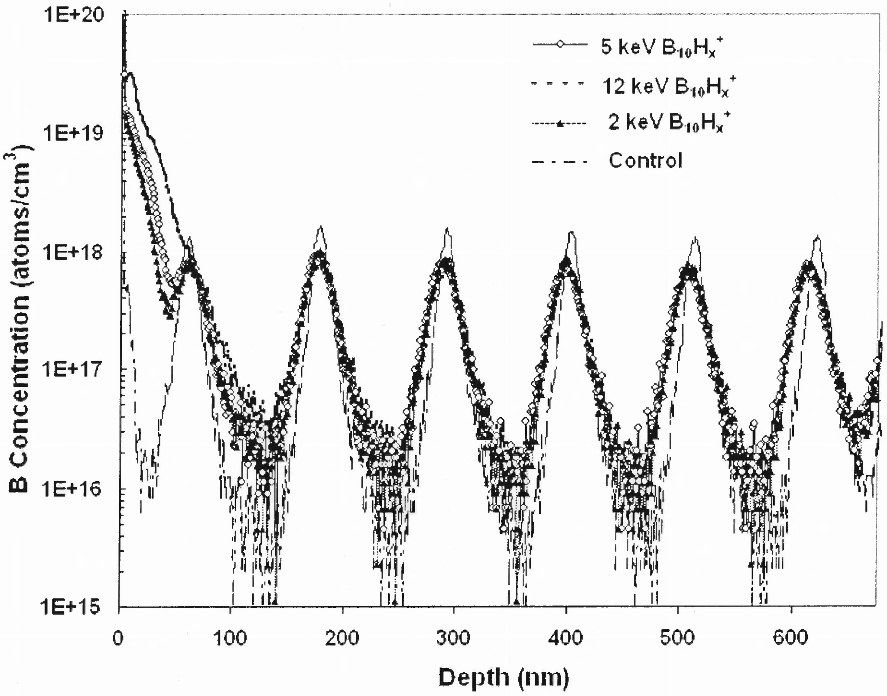

Figure 5.5 Depth profiles of boron marker layers in samples implanted with $B_{10}H_x^+$ cluster ions at 12 keV, 5 keV, and 2 keV.

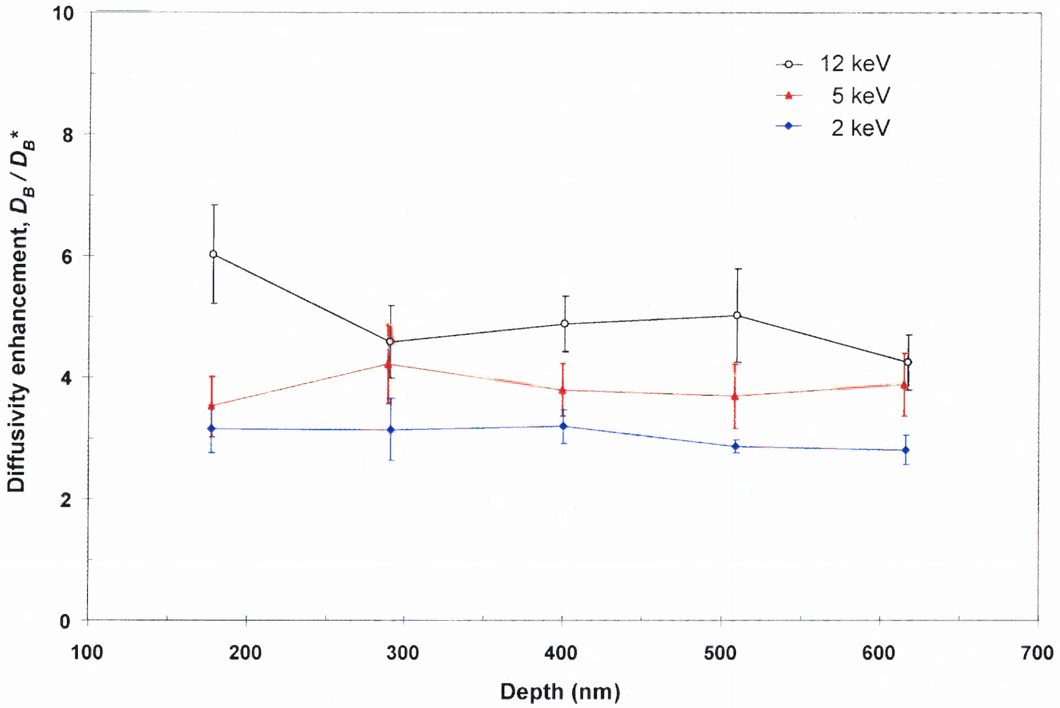

Figure 5.6 Comparison of boron diffusivity enhancements for the second through sixth B marker layers from samples implanted with $B_{10}H_x^+$ cluster ions at 12 keV, 5 keV and 2 keV.

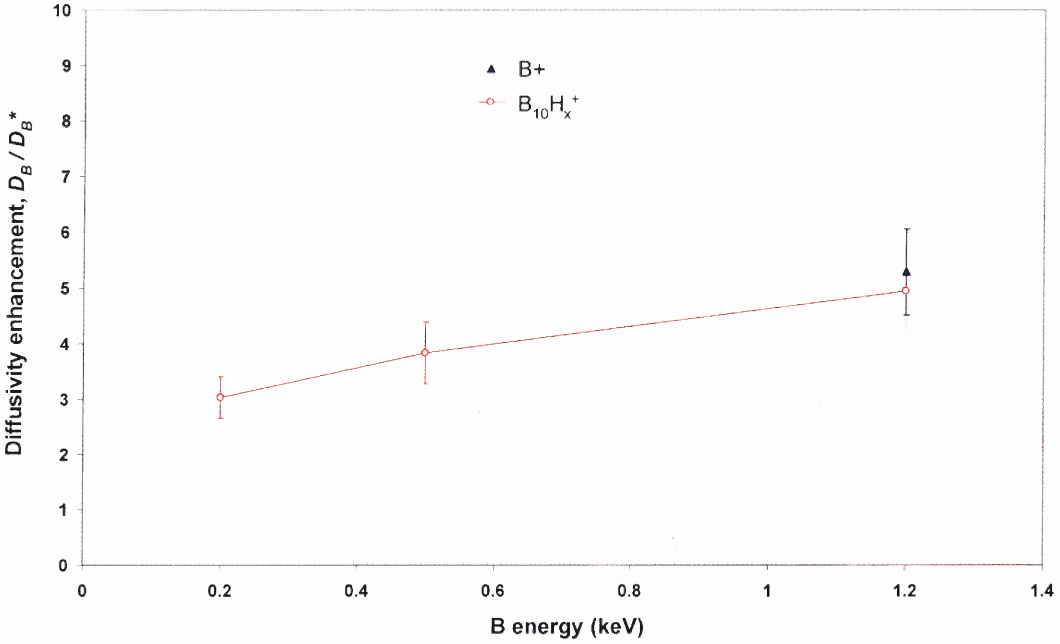

Figure 5.7 The amount of TED induced by decaborane implantation decreases with decreasing cluster ion energy. This is explained by the proximity of implantation damage to the Si surface at lower ion energy.

5.2 SIMS Depth Profiles of Boron and Hydrogen

One of the differences between implantation with B^+ ions and $B_{10}H_x^+$ ions is that the latter also co-implants hydrogen. There is interest in the implanted hydrogen since it may affect the transistor performance, if a significant amount of hydrogen remained in the silicon after activation annealing. It is reasonable to expect that hydrogen atoms implanted near the silicon surface will easily diffuse out. Computer simulation showed that some H is implanted, although the amount is much less than the B [34]. Hydrogen incorporated in Si by high energy (440 keV) decaborane implantation was not detected by SIMS after RTA at temperatures of 800°C or above [24]. However, there was no experimental study revealing the whereabouts of hydrogen before and after annealing for lower energy decaborane implantation.

5.2.1 Experimental Procedures

To investigate the depth profiles of boron and hydrogen atoms in Si implanted with decaborane cluster ions, a Si sample was prepared from an n-type Si (100) wafer. Before implantation, the sample was cleaned with buffered hydrofluoric acid for 40 seconds to remove the surface oxide. Decaborane implantation was performed with 12 keV $B_{10}H_x^+$ ion beam at normal incident direction to a B dose of 2.0×10^{15} cm^{-2}. The implanted sample was then divided into four pieces. Two of the pieces were kept as-implanted, while the other two pieces were subjected to rapid thermal annealing (1045 °C /0.9s) in a flowing Ar gas ambience using a Heatpulse 8108 RTP furnace at Bell Laboratories, Lucent Technologies. Detailed descriptions about the RTP equipment and recipe have been provided in Ref. [31]. A "P-clean", which is described in Section 5.1.1, was used to remove possible metal contaminants from the sample surface before annealing. One pair of the as-implanted and annealed samples was used for boron profile analysis and the other pair for hydrogen profile analysis. Secondary Ion Mass Spectrometry (SIMS) was employed to obtain B and H depth profiles in the samples as well as in an unimplanted control sample. Distribution of Si and O were also measured. SIMS measurements were performed at Evans-East using a PHI Quadrupole SIMS instrument with the H detection limit at 1.0×10^{19} cm^{-3} and the B detection limit at 3.0×10^{17} cm^{-3}. A primary O_2^+ ion beam at 0.5 keV was used in measurements of B and Si while a 1 keV Cs^- ion beam was used in measurements of H and O. The B concentration was calibrated against a NIST reference material (SRM-2137). Its relative error is estimated at 10%. The depth scales were determined using a sputtering rate standard (EE-1025) by measuring the time required to sputter through the peak of the standard. The accuracy of the depth calibration is within 3%.

5.2.2 Results and Discussion

Depth profiles of B in Si measured on the as-implanted and annealed samples in Figure 5.8 show that shallow implantation of B in Si is achieved with decaborane ions. The projected range of B was measured as 47 Å, which is comparable to the value (68 Å) for equivalent B^+ implant, which was obtained from a TRIM simulation. The junction depth is 40 nm at the B concentration level of 1×10^{18} cm^{-3}. Annealing results in diffusion, which significantly spreads the B concentration. The junction depth is 57 nm at 1×10^{18} cm^{-3} concentration level. Shallower junctions could be obtained with lower doses. The high dose in this experiment was used to facilitate the measurements of H concentration.

Figure 5.9 shows the corresponding H profiles, together with the results obtained from the unimplanted region. Although a significant amount of H is seen in the as-implanted sample, annealing reduces it by two orders of magnitude near the apparent H projected range. At the junction depth, the H concentration after annealing is the same as that in the control region. This indicates that little co-implanted hydrogen was left in Si after annealing, which is in agreement with an earlier study [24]. Note a broad peak close to the surface (~ 20 Å) in both the as-implanted and annealed samples, which is not seen in the control region. Comparison with Si and O profiles in Figure 5.10 and 5.11 leads to an explanation that the peak is at the Si/SiO_2 interface that traps the H atoms.

The results confirm that decaborane ion implantation implants B at the same depth as a B^+ ion beam with ten times lower energy. Hydrogen implanted with decaborane ions diffuses out of Si almost entirely at the junction depth, and little detrimental effect on device performance can be expected from the co-implanted hydrogen.

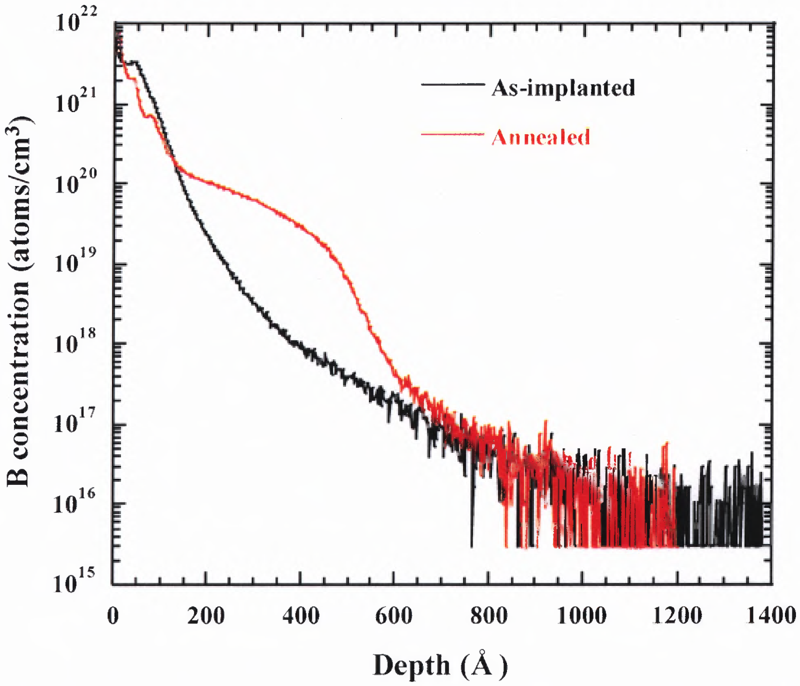

Figure 5.8 Depth profiles of B in Si measured on the as-implanted and annealed samples.

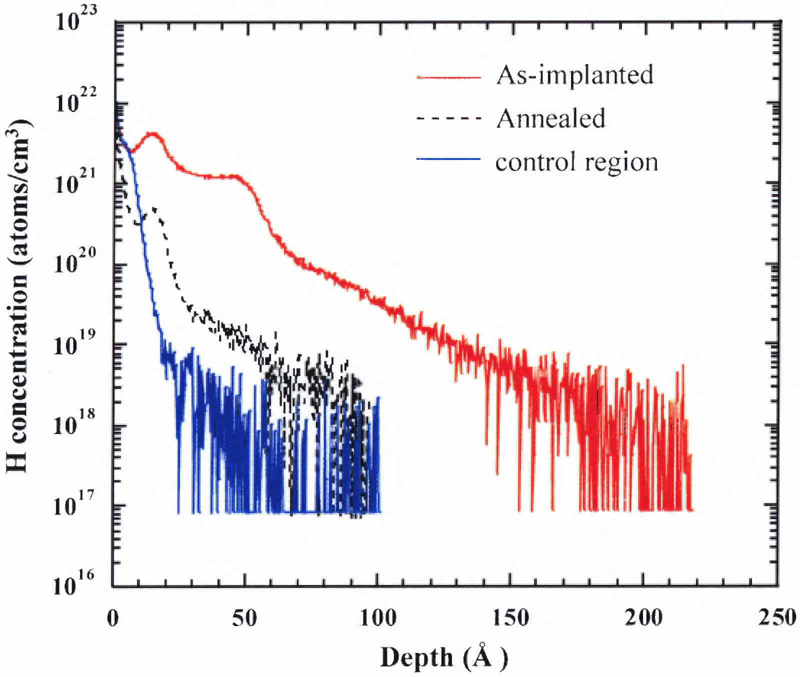

Figure 5.9 Depth profiles of H in Si measured on the as-implanted and annealed samples.

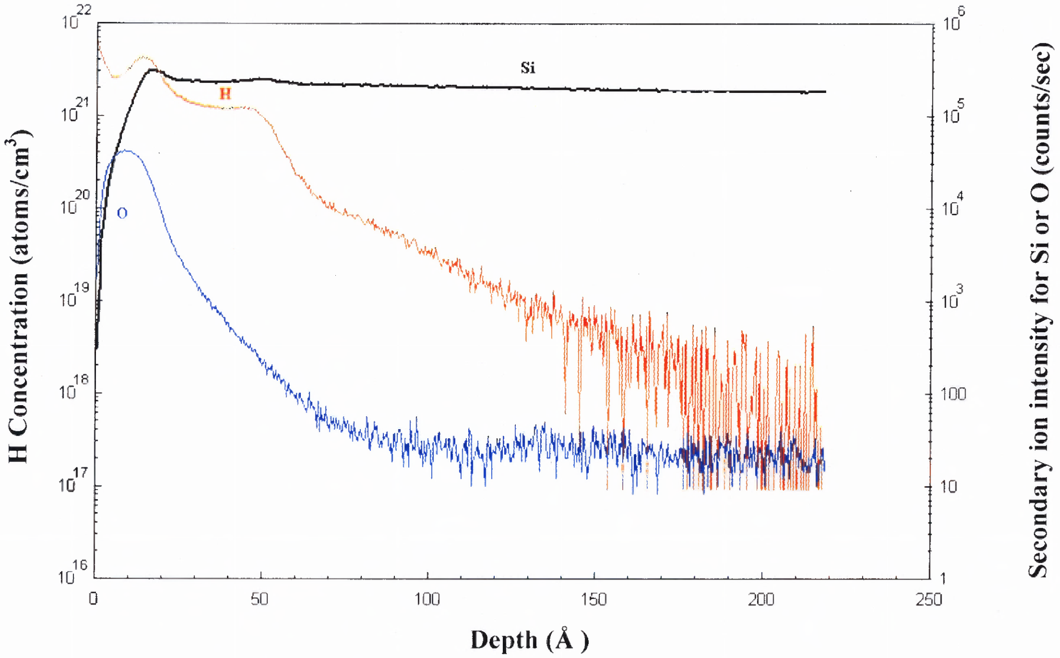

Figure 5.10 SIMS profiles of H, O, and Si in Si implanted with 12 keV $B_{10}H_x^+$ cluster ions (2×10^{15} B/cm^2) before rapid thermal annealing. Si and O concentrations are not normalized.

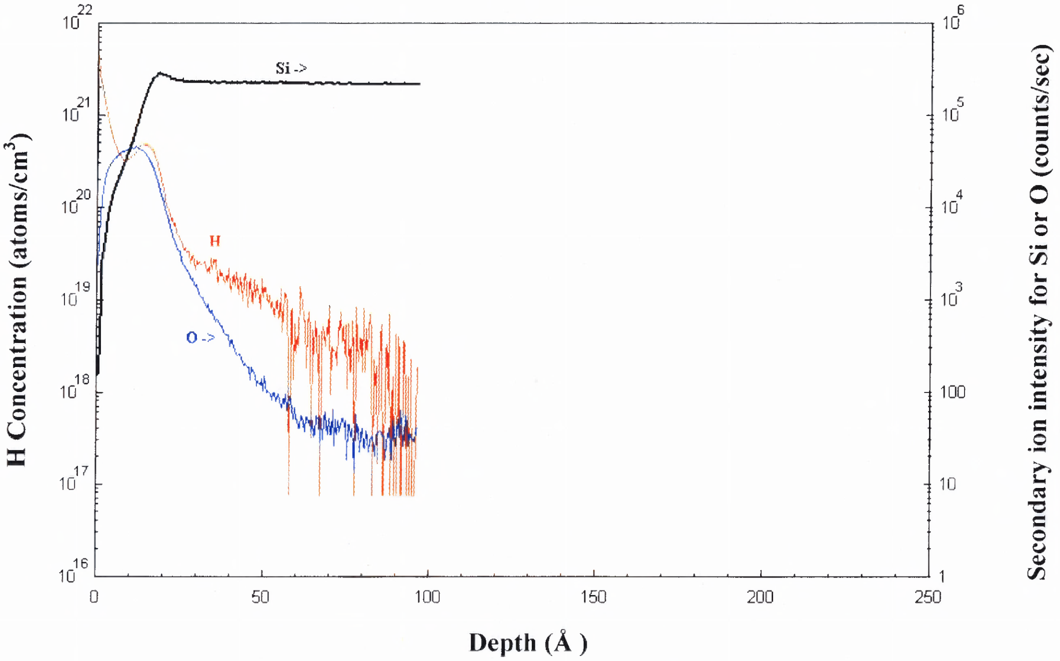

Figure 5.11 SIMS profiles of H, O, and Si in Si implanted with 12 keV $B_{10}H_x^+$ cluster ions (2×10^{15} B/cm^2) after rapid thermal annealing. Si and O concentrations are not normalized.

CHAPTER 6

SURFACE EFFECTS OF DECABORANE IMPLANTATION

Ion Implantation not only induces lattice damages inside the target material, but also causes changes on the target surface due to sputtering. Sputtering is the erosion of a sample by energetic particle bombardment and is characterized primarily by the sputtering yield, which is defined as the ratio of the mean number of emitted atoms to the number of incident particles [34]. The sputtering yield depends on the structure and composition of the target material, and the parameters of the incident ion beam including its impact angle. In the sputtering process, atoms are ejected from the outer surface layers. The bombarding ions transfer energy in collisions with target atoms, which recoil with sufficient energy to induce recoils of other lattice atoms. Some of these backward recoils will approach the surface with high enough kinetic energy to escape from the surface.

When an energetic cluster ion impacts upon a surface, its constituent atoms interact nearly simultaneously with many target atoms and deposit high energy density into a very small volume of the target material. The atoms of the target undergo multiple collisions with one another and with the atoms of the projectile, resulting in a complex collision cascade. MD simulation results [45] indicate that when an Ar_{688} cluster collides with a Si (100) surface, the kinetic energy of the cluster is transferred to the target nearly isotropically and a symmetrical crater is formed. Within the region close to the crater, the atomic arrangement becomes highly disordered. Many target atoms are sputtered in directions lateral to the trajectory of the impinging cluster. This results in sputtering and implantation effects which are fundamentally different from those associated with the simpler binary collisions which take place during monomer ion impacts.

The sputtering yield of Si by decaborane cluster ions and the effect of cluster ion bombardment on the surface morphology are both important factors when evaluating the implantation process. Rough surfaces after ion bombardment may have adverse effects on the subsequent fabrication processes, and a large sputtering yield can cause significant loss of the substrate materials particularly with low energy cluster ions implanted into fine device structures. Although $B_{10}H_x^+$ cluster ions can be implanted at an acceleration energy equivalent to that of monomer B ions, the ion-solid interaction mechanism involved in the impact of these two types of ions may be quite different. Part of this dissertation work is dedicated to the efforts to answer these questions. The study of sputtering and surface morphology of silicon surface impacted by decaborane cluster ions will also help to expand the knowledge on cluster-solid interaction in general and may point out other potential applications.

6.1 Sputtering Yield of Silicon with Decaborane Cluster Ions

6.1.1 Experimental Procedures

In order to obtain the sputtering yield of Si with decaborane, special samples were fabricated with the Si/C/Si sandwich structure, as shown in Figure 6.1. First, a layer of diamond-like carbon (DLC) was deposited on a *p*-type Si substrate using chemical vapor deposition at Epion Corporation in Billerica, Massachusetts. Then a very thin amorphous silicon film (a-Si) was grown on the DLC layer by low temperature molecular beam (MBE) deposition at Bell Laboratories, Lucent Technologies in Murray Hill, New Jersey.

The purpose of the DLC layer is to energetically separate, on the Rutherford Backscattering Spectroscopy (RBS) spectra, the peak of the top a-Si film from the edge corresponding to the Si substrate. Because of the large difference in the atomic mass between carbon (AMU = 12) and silicon (AMU = 28), the carbon spectrum edge is below those two energies. But the loss of energy for the ions back scattered from the Si substrate passing through the carbon layer is sufficient to shift the substrate edge so that the high energy peak corresponds only to the top a-Si layer.

The Si area density in the a-Si film was measured as $1.55 \times 10^{17}/\text{cm}^2$ by RBS. This corresponds to a film thickness of about 310Å, which is in agreement with MBE process data.

Figure 6.2 shows the RBS spectrum obtained from the Si/C/Si sample before implantation together with the RUMP simulation [70] indicated by the red solid line. The samples subjected to energetic ion bombardment were also evaluated with RBS. Based on the difference in the peak counts for the top a-Si layer between the implanted sample and unimplanted sample, the amount of Si atoms removed from the top layer was determined and thus the sputtering yield of a-Si was calculated as following:

$$Y_{Si} = \frac{\text{Amount of Si atoms sputterd from the surface}}{\text{Amount of incident ions}} \qquad (6.1)$$

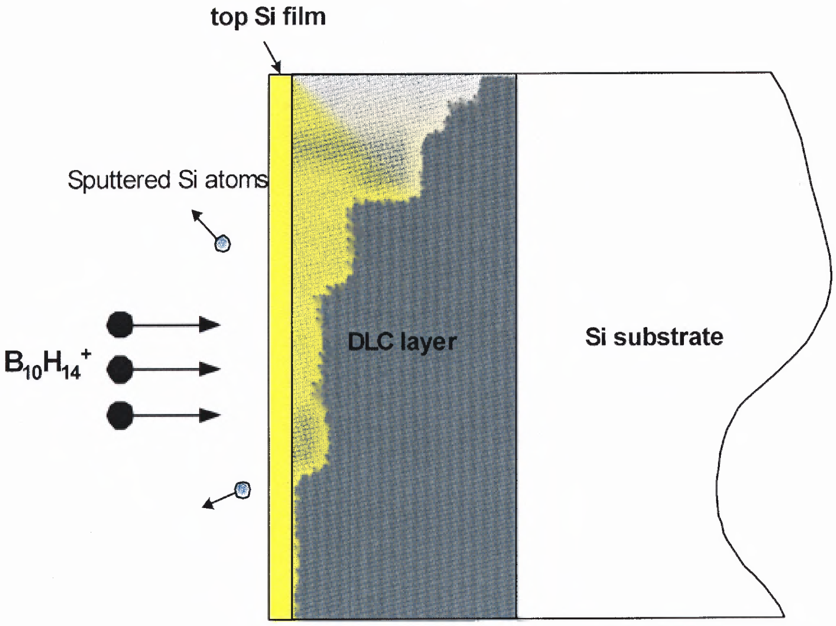

Figure 6.1 Schematic of the sputtering yield experiment with a Si/C/Si sample. The diamond-like carbon (DLC) layer served to separate the contributions from the Si substrate and from the top a-Si film in the Rutherford Backscattering Spectroscopy (RBS) spectra.

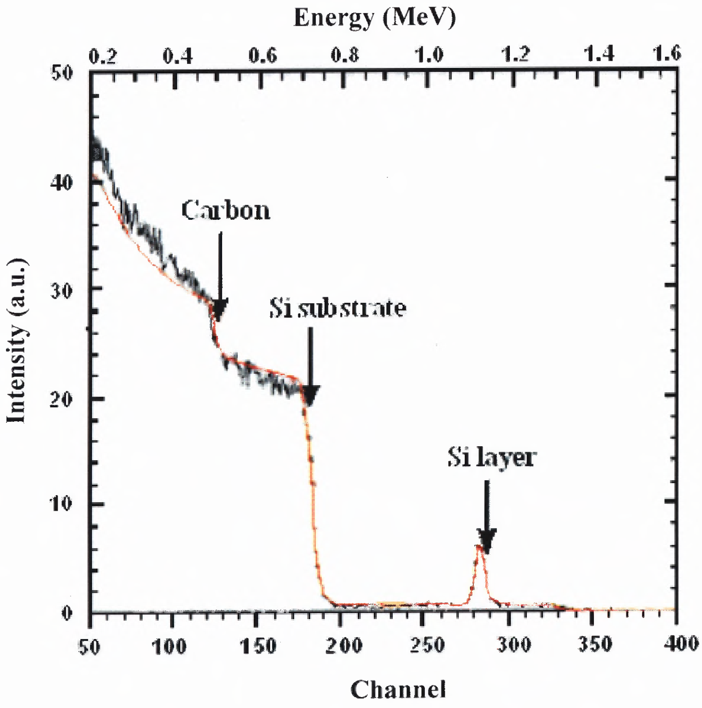

Figure 6.2 RBS spectrum of the Si/C/Si sample before implantation.

6.1.2 Results

To verify the validity of sputtering yield measurements based on RBS analysis, a Si/C/Si sample was implanted with 5 keV Ar^+ ions to the nominal dose of 5.0×10^{15} atoms/cm^2, as measured by the ion beam current integration. The sample was then analyzed with RBS using 2.2 MeV He^+ primary ions, at Bell Laboratories, Lucent Technologies. The RBS system had a 4 keV/channel energy resolution. The amount of Si removed by Ar^+ bombardment was measured as 3.5% of the initial amount, that is:

$$3.5\% \times (1.55 \times 10^{17} / cm^2) = 5.425 \times 10^{15} / cm^2 \tag{6.2}$$

The sputtering yield of Si by 5 keV Ar^+ ions was calculated to be:

$$Y_{Si/Ar^+} = \frac{5.425 \times 10^{15} atoms / cm^2}{5.0 \times 10^{15} ions / cm^2} \approx 1.1 \tag{6.3}$$

This value is close to the available data on the sputtering yield of Si by 5 keV Ar^+ ions that is ~1.3 [69]. This indicates that it is feasible to measure the sputtering yield of Si by $B_{10}H_x^+$ cluster ions using RBS.

Two samples were then implanted with $B_{10}H_x^+$ ions at 12 keV to two different doses. RBS measurements show that, on the sample implanted to the nominal dose of 5.0 $\times 10^{16}$ B atoms/cm^2, the amount of Si removed was 15% of the initial amount, that is:

$$15\% \times (1.55 \times 10^{17} / cm^2) = 2.325 \times 10^{16} / cm^2 \tag{6.4}$$

The thickness of the Si removed after $B_{10}H_x^+$ implantation is:

$$(2.325 \times 10^{16} / cm^2)/(5 \times 10^{22} / cm^3) = 4.65 \times 10^{-7} cm = 46.5 Å \tag{6.5}$$

The sputtering yield of Si with $B_{10}H_x^+$ ions at 5.0×10^{16} B atoms/cm^2, in terms of number of ejected Si atoms per incident boron atom, was calculated to be:

$$Y_{Si/B_{10}H_x^+} = \frac{2.325 \times 10^{16}\ Si\ atoms/cm^2}{5 \times 10^{16}\ B\ atoms/cm^2} = 0.465 \tag{6.6}$$

For the sample implanted to the nominal dose of 1.0 × 10^{17} B atoms/cm^2, the amount of removed Si was 24% of the initial amount, that is:

$$24\% \times (1.55 \times 10^{17} / cm^2) = 3.72 \times 10^{16} / cm^2 \tag{6.7}$$

The thickness of the Si removed after $B_{10}H_x^+$ implantation is:

$$(3.72 \times 10^{16} / cm^2)/(5 \times 10^{22} / cm^3) = 7.44 \times 10^7 cm = 74.4Å \tag{6.8}$$

The sputtering yield of Si with $B_{10}H_x^+$ ions at 1.0 × 10^{17} B atoms/cm^2, in terms of number of ejected Si atoms per incident boron atom, was calculated to be:

$$Y_{Si/B_{10}H_x^+} = \frac{3.72 \times 10^{16}\ \mathrm{Si\ atoms/cm^2}}{1.0 \times 10^{17}\ \mathrm{B\ atoms/cm^2}} = 0.372 \tag{6.9}$$

The statistical measurement errors are assumed to be inversely proportional to the square root of RBS counts. The weighted average of the above two values is 0.41 ± 0.04, which means there are 0.41 Si atoms sputtered from the surface per incident boron atom. An important question is how the sputtering yield of a 10-atom cluster (B_{10}) compares with B monomer ions. Hydrogen is expected to have a negligible effect, since it is so light.

To further study the dependence of the Si sputtering yield on the incident energy of decaborane cluster ions, two more Si/C/Si samples were implanted to 1.0 × 10^{17} B atoms/cm^2 with $B_{10}Hx^+$ cluster ions accelerated to 9 keV and 5 keV, respectively. Then the samples were analyzed with RBS facility at the Army Research Laboratory located in

Aberdeen, Maryland. The RBS experiment was performed using 2 MeV He^+ ions, on a National Electrostatics tandem accelerator (model: 5SDH-2 Pelletron). The RBS scattering angle was 170° degrees, and the incoming beam was normal to the surface of the sample. Measurements of the a-Si film thickness were performed in both the irradiated area and within an unirradiated area. Figure 6.3 and 6.4 show the RBS spectra for the irradiated area and an unirradiated area of the samples implanted with 9keV and 5 keV $B_{10}H_x^+$ ions, respectively. Using RUMP, the data were fit by normalizing the back ledges of the spectra, where the signal is entirely from the silicon substrate and the DLC carbon. Then the RUMP subroutine SIM was used to fit a simulation to the spectrum. Once a fairly good simulation was achieved, the RUMP subroutine PERT was used to do a least-squares fit to the surface silicon layer thickness to yield the thickness numbers. The sputtered depth is obtained from the difference between the film thickness in the unirradiated region and that in the irradiated area. Table 6.1 lists the initial film thickness and the derived sputtered thickness for each of the samples.

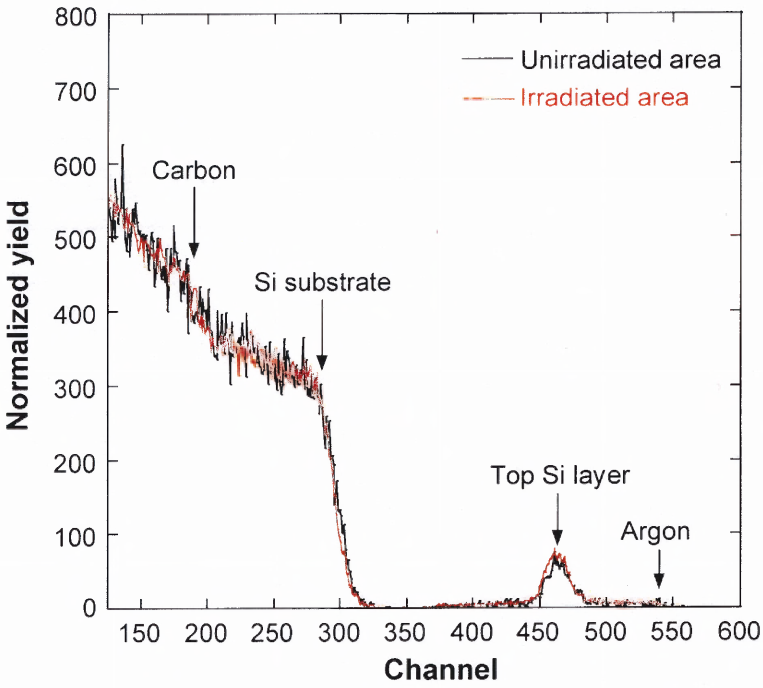

Figure 6.3 RBS spectra of the Si/C/Si sample irradiated with 9 keV $B_{10}H_x^+$ ions.

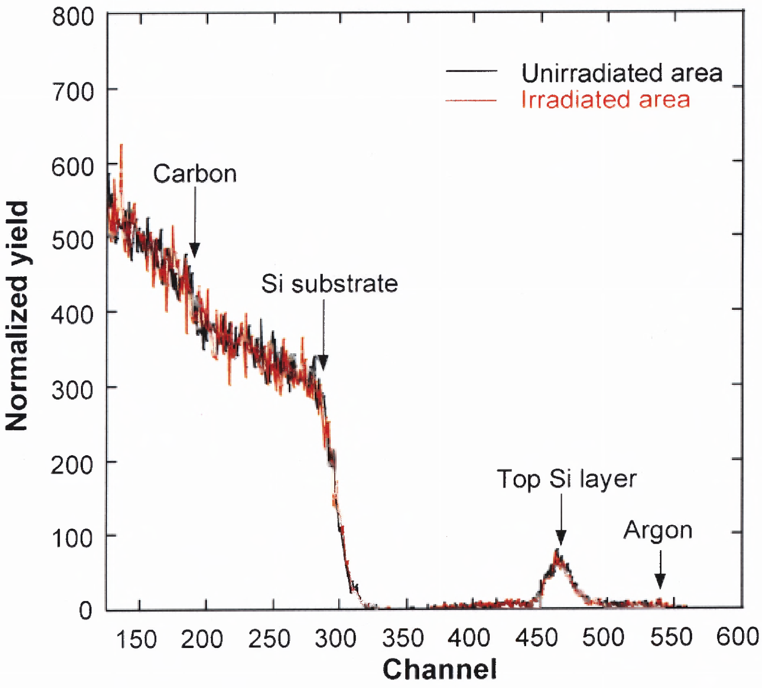

Figure 6.4 RBS spectra of the Si/C/Si sample irradiated with 5 keV $B_{10}H_x^+$ ions.

Based on these experimental values, the sputtering yield of a-Si that is defined as the number of ejected Si atoms per incident boron atom, is calculated using the following equation:

$$Y_{Si} = \frac{\text{Si density (atoms/cm}^3\text{)} \times \text{sputtered depth (cm)}}{\text{ion dose (B/cm}^2\text{)}} \tag{6.10}$$

In case of 9 keV decaborane cluster ion irradiation, the Si sputter yield is:

$$Y_{Si} = \frac{5 \times 10^{22}\ \text{(atoms/cm}^3\text{)} \times 57 \times 10^{-8}\ \text{(cm)}}{1.0 \times 10^{17}\ \text{(B/cm}^2\text{)}} = 0.285 \tag{6.11}$$

For the irradiation with 5 keV decaborane cluster ions, the Si sputtering yield is:

$$Y_{Si} = \frac{5 \times 10^{22}\ \text{(atoms/cm}^3\text{)} \times 36 \times 10^{-8}\ \text{(cm)}}{1.0 \times 10^{17}\ \text{(B/cm}^2\text{)}} = 0.180 \tag{6.12}$$

Table 6.1 RBS Measurement Results for Sputtering Yield of Si by Decaborane Ions

Ion Energy (keV)	B dose ($\times 10^{17}$ cm^{-2})	Initial Film Thickness (Å)	Sputtered Depth (Å)	Sputtering yield *Y*
12	0.5	310	46.5	0.465
12	1.0	310	74.4	0.372
9	1.0	287	57	0.285
5	1.0	250	36	0.180

6.1.3 Discussion

To our best knowledge, there are no published data on sputtering yields of Si with B either in the form of monomer ions or in the form of cluster ions. The data presented in this thesis represent the first systematic study on this phenomenon. The main interest of this research is the difference between the effects of cluster and monomer ions of equivalent energy. For comparison purposes, an empirical formula, developed for calculating sputtering yield of monomer ions, could be used to estimate the Si sputtering yield by atomic B^+ at energies equivalent to those used in the decaborane impact experiments described above. The empirical formula was developed by Yamamura *et al.* [71], with parameters determined by the best fits to available sputtering yields data over a wide range of ion-target combinations and energy [72]:

$$Y(E) = 0.42\frac{\alpha^* Q K s_n(\epsilon)}{U_S\left[1 + 0.35 U_S s_e(\epsilon)\right]}\left[1\text{-}(E_{th}/E)^{1/2}\right]^{2.8} \tag{6.13}$$

where:

$Y(E)$ - sputtering yield

E - energy of incident ions (eV)

E_{th} - sputtering threshold energy (eV)

α^* *and* Q - empirical parameters

U_S - sublimation energy of the target (eV)

$s_n(\varepsilon)$ - Lindhard's elastic reduced stopping cross section

$s_e(\varepsilon)$ - Lindhard's inelastic reduced stopping cross section

K - conversion factor from s_n to the stopping cross section S_n

The functions $s_n(\varepsilon)$ and $s_e(\varepsilon)$ are expressed in terms of the reduced energy ε:

$$\varepsilon = \frac{0.03255}{Z_1 Z_2 \left(Z_1^{2/3} + Z_2^{2/3}\right)^{1/2}} \frac{M_2}{M_1 + M_2} E \tag{6.14}$$

where Z_1 and Z_2 are the atomic numbers of the incident ion and target atom and M_1 and M_2 are their atomic mass numbers, respectively.

Lindhard's elastic reduced stopping cross section is approximated by:

$$s_n(\varepsilon) = \frac{3.441\sqrt{\varepsilon}\ln(\varepsilon + 2.718)}{1 + 6.355\sqrt{\varepsilon} + \varepsilon\left(6.882\sqrt{\varepsilon} - 1.708\right)} \tag{6.15}$$

The inelastic reduced stopping cross section is given by:

$$s_e(\varepsilon) = k\varepsilon^{1/2} \tag{6.16}$$

where,

$$k = 0.079 \frac{(M_1 + M_2)^{3/2}}{M_1^{3/2} M_2^{3/2}} \frac{Z_1^{2/3} Z_2^{2/3}}{\left(Z_1^{2/3} + Z_2^{2/3}\right)^{3/4}} \tag{6.17}$$

The conversion factor K is in the unit of eV-cm/10^{15} atoms and is calculated using the following equation:

$$K = \frac{S_n}{s_n} = 8.478 \frac{Z_1 Z_2}{\left(Z_1^{2/3} + Z_2^{2/3}\right)^{1/2}} \frac{M_2}{M_1 + M_2} \tag{6.18}$$

Best fit values of empirical parameters E_{th}, α^* and Q were obtained by applying equation (6.14) to experimental data [71, 72]. The parameter Q was observed to depend only on the target material. Values of α^* were found to be dependent on each ion-target combination, and the following empirical expression for α^* was obtained:

$$\alpha^* = 0.08 + 0.164(M_2 / M_1)^{0.73} + 0.0145(M_2 / M_1)^{1.29} \tag{6.19}$$

The sputtering threshold energy is given by:

$$E_{th} = \left[1.9 + 3.8(M_2/M_1)^{-1} + 0.134(M_2/M_1)^{1.24}\right]/U_S \tag{6.20}$$

Table 6.2 lists all the parameters used in equation (6.13). The estimated sputtering yields of Si with B monomer ions are compared in to those with B in cluster ions for three incident B energies Table 6.3 as well as in Figure 6.4. The errors in the estimated values came from the uncertainty of the parameter Q, and the errors of the experimental values contained the contributions from the RMS measurement errors and from the estimated relative error (10%) in dose measurements.

The results show that the experimental values agree well with the estimated values for all three B energies under investigation, considering the measurement errors and the uncertainties in the parameters and approximations in the formula. Also shown is the trend of increased sputtering yield with increasing ion energy, which is in agreement with general understanding of ion energy dependence of the sputtering yield for the studied energy regime. These findings suggest that, in the sense of sputtering, the constituent B atoms in a decaborane cluster behave much like independent B atoms.

Table 6.2 Parameters Used in Equation (6.13) for Calculation of Sputtering Yield of Si by B^+ Ions

Z_1	5	Z_2	14
M_1	10.811	M_2	28.0855
U_S (eV)	4.63	E_{th} (eV)	17.596
α^*	0.370	Q	0.78 ± 0.17

Table 6.3 Comparison of Sputtering Yield of Si with B in the Form of Monomer Ions and in the Form of Cluster Ions

E (eV)	500	900	1200
Estimated sputtering yield [B as monomer ions]	0.25 ± 0.05	0.32 ± 0.07	0.35 ± 0.08
Experimental sputtering yield [B in decaborane cluster]	0.18 ± 0.05	0.28 ± 0.06	0.41 ± 0.06

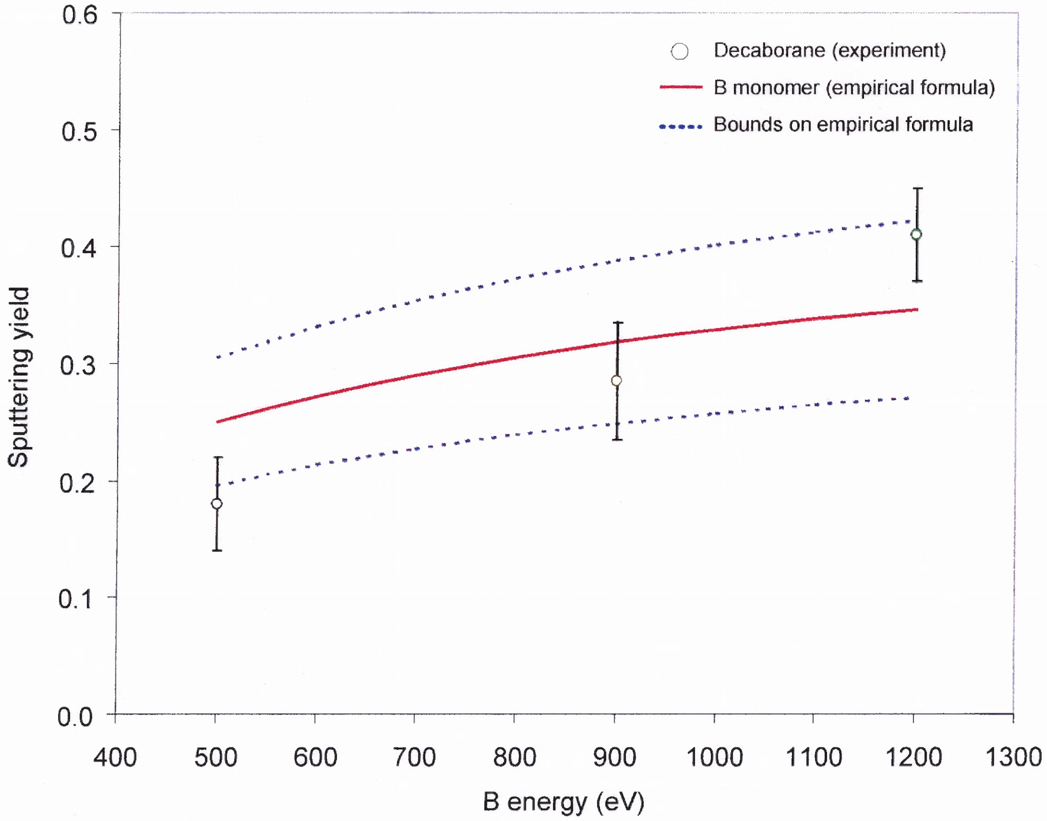

Figure 6.5 Comparison of Si measured sputtering yields (ejected Si atoms per incident B atom) for decaborane ions (experimental points) with the empirical formula for B monomer ions of equivalent energy. The bounds on the values of the empirical formula are due to the uncertainty of the parameter *Q* in Eq. (6.13).

6.2 AFM Study on Morphology of $B_{10}H_x^+$ Bombarded Surfaces

6.2.1 Description of the Experiments

It is of both scientific and technological interest to investigate the irradiation effect of decaborane cluster ions on solid surfaces. The study helps us to understand whether B atoms in a decaborane ion behave like those in large gas cluster that showed different surface effects than the monomers. Also for the reasons as described earlier in this chapter, it is important to demonstrate that decaborane ions at least will not roughen the substrate surface, if they are intended for use in very fine featured electronic device structures.

For surface studies, Si/C/Si samples (See Section 6.1.1) with a thin top layer of amorphous Si (a-Si) and crystalline Si (c-Si) samples cut from a n-type Si (100) wafer were irradiated with $B_{10}H_x^+$ cluster ions to 1.0×10^{17} B/cm^2 at 5 keV and 12 keV. To see the effect of $B_{10}H_x^+$ cluster ions on other surfaces (e.g., polycrystalline metal), a Ta film (~ 2.4 μm) deposited on Si by sputtering was also irradiated by 12 keV $B_{10}H_x^+$ ions to a dose of 1.0×10^{17} B/cm^2. To contrast the surface effects of cluster and monomer ions some samples were also irradiated in the same apparatus with Ar^+ ions to 5.0×10^{16} Ar/cm^2. All samples were probed with tapping mode AFM before and after implantation. The AFM tests were carried on a Digital Instruments NanoscopeIIIa® facility at Epion Corporation in Billerica, MA, using SiN tips of ~10 nm nominal radius. The data files were processed using off-line analyzing software at NJIT. Surface roughness and Power Spectra Density were extracted and used to characterize the morphology change on different surfaces due to decaborane irradiation. The average roughness R_a is defined as the arithmetic average of the absolute values of the surface height deviations measured from the mean plane:

$$R_a = \frac{1}{n}\sum_{i=1}^{n}\left|z_i - \bar{z}\right| \qquad (6.21)$$

where n is the total number of height data points obtained while the probe was scanned over the sample surface of a specific area, z_i is the height at position i, and $\bar{z}$ is the average height. While two surfaces could statistically have the same "average roughness", they may be in fact significantly different in surfaces features. Power Spectral Density (PSD) analysis, which reveals periodic surface features and provides their spatial frequency distribution, is especially useful in evaluating extremely flat surfaces such as that of Si wafers.

6.2.2 Results and Discussion

AFM imaging shows that irradiation by energetic decaborane cluster ions smoothes rather than roughens the surfaces studied in this dissertation.

Figure 6.6 shows the AFM image (3 μm × 3 μm scan area) of the initial a-Si surface, with an average roughness R_a = 3.7 Å. Figure 6.7 and 6.8 are the images of the same scan size on samples irradiated with $B_{10}H_x^+$ ions at 12 keV and 5 keV, respectively. After 12 keV $B_{10}H_x^+$ ion bombardment, the average roughness of a-Si decreased to R_a = 2.4 Å versus R_a = 3.7 Å before the irradiation. After 5 keV $B_{10}H_x^+$ ion bombardment, the average roughness of a-Si decreased to R_a = 2.3 Å versus R_a = 3.7 Å before the irradiation. The difference is significant, although the absolute changes may be small because the initial surface was already very smooth. AFM images reveal that a uniform morphology of the initial surface with sharp features of varying heights (see Figure 6.6). Cluster ion irradiation significantly reduces the sharp features on the initial surface and leaves the surface with gentle undulations (Figure 6.7 and 6.8). The results also indicate that the ion energy has no significant effect on the final roughness for these two values used. In Figure 6.9, the Power Spectra Density (PSD) of the initial surface is compared to those of the areas irradiated with the 12 keV and 5 keV $B_{10}H_x^+$ ion beams. What is clearly shown in this graph is that $B_{10}H_x^+$ ion bombardment effectively decreased the 2-dimensional isotropic power of the high spatial frequency ($\geq$ 10 □m^{-1}) features, while it has little effect on the lower spatial frequency features. This is in agreement with the qualitative observations on the AFM images, since diminishing of the sharp surface features corresponds to attenuation of high spatial frequency components in the PSD.

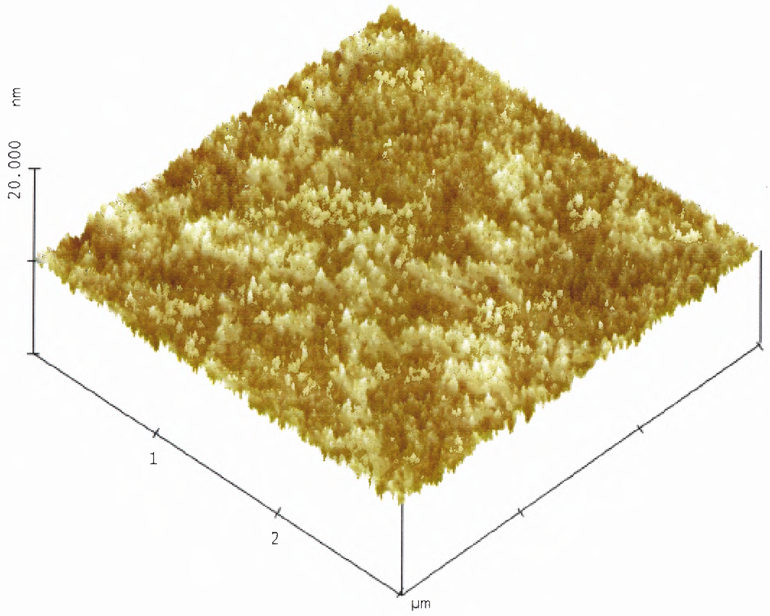

Figure 6.6 AFM image (3□m × 3□m) of the initial a-Si surface (R_a = 3.7 Å).

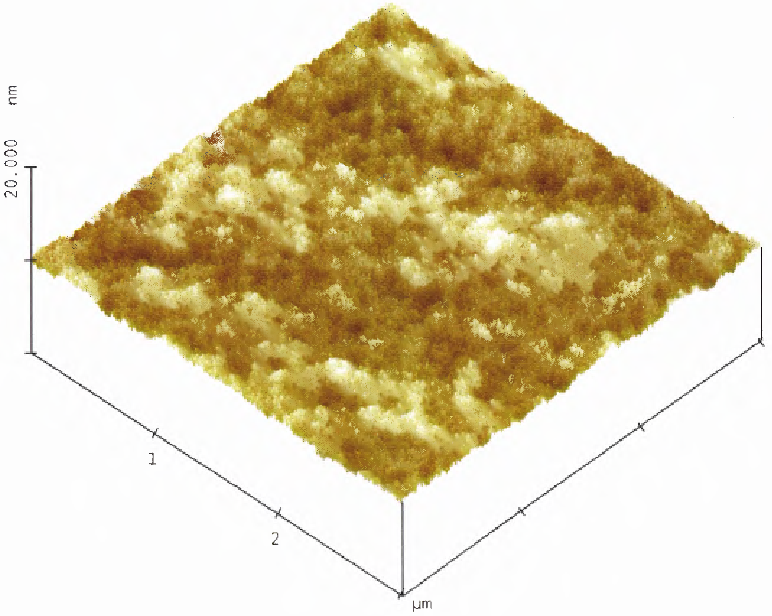

Figure 6.7 Average roughness of a-Si surface was decreased to R_a = 2.4 Å after irradiation with 12 keV $B_{10}H_x^+$ cluster ions.

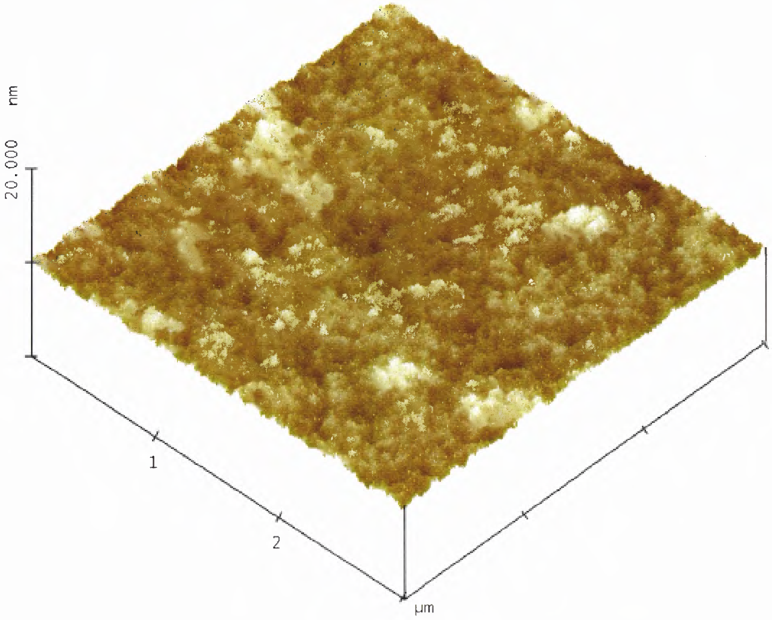

Figure 6.8 Average roughness of a-Si surface was decreased to R_a = 2.3 Å after irradiation with 5 keV $B_{10}H_x^+$ cluster ions.

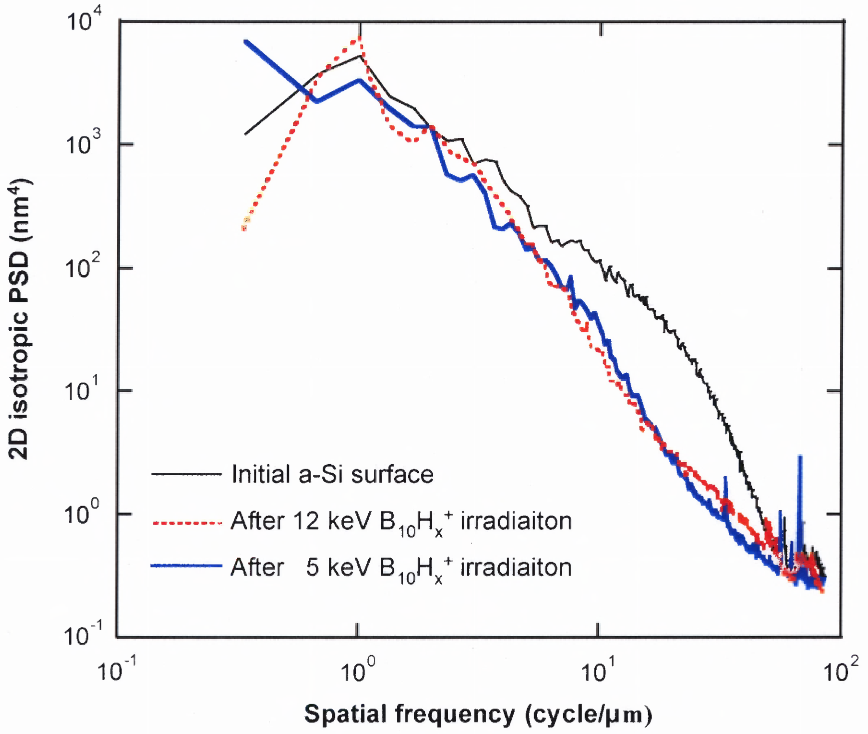

Figure 6.9 PSD of the initial a-Si surface (shown in Figure 6.6) is compared to those of a-Si surfaces irradiated with $B_{10}H_x^+$ cluster ion beam at 12 keV and 5 keV, shown in Figure 6.7 and Figure 6.8, respectively.

Results of tapping mode AFM (1 μm × 1 μm scan) on a c-Si sample also show that the surface was smoothed after $B_{10}H_x^+$ ion irradiation. The average roughness of the c-Si surface decreased from R_a = 1.15 Å (Figure 6.10) to R_a = 0.81 Å (Figure 6.11), due to irradiation of 12 keV $B_{10}H_x^+$ ion beam. Similar to the case of a-Si, PSD comparison for c-Si surfaces before and after irradiation (Figure 6.13) shows the decrease of features in the spatial frequency range near 10 μm^{-1}. The initial c-Si surface, however, was very smooth and had lower amplitude in this frequency range, as compared to the initial a-Si surface.

In contrast to the smoothing effect from the decaborane cluster ions, irradiation with monomer Ar^+ ions significantly roughens the c-Si surface, causing R_a to increase to

5.11 Å. The dramatic change in morphology can be clearly seen from the AFM image (Figure 6.12) as well as from the PSD results in Figure 6.13.

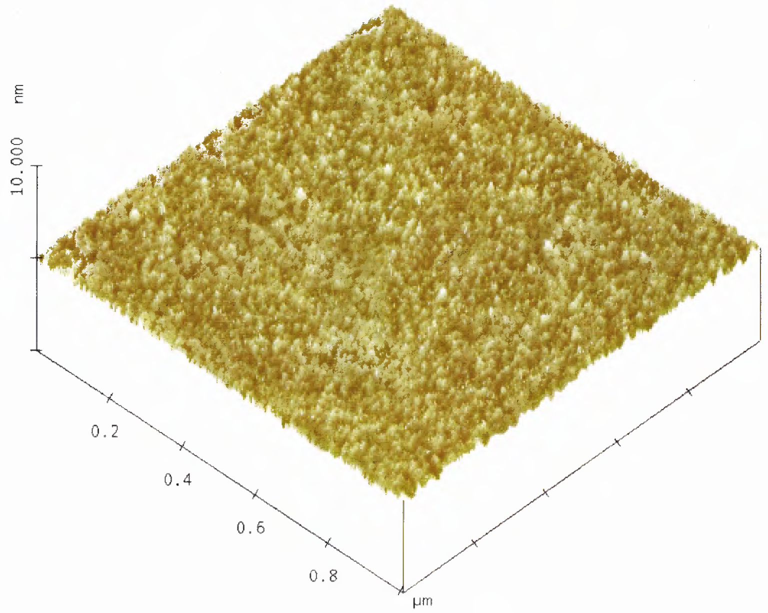

Figure 6.10 AFM image (1 □m × 1 □m) of the initial c-Si surface (R_a = 1.51 Å).

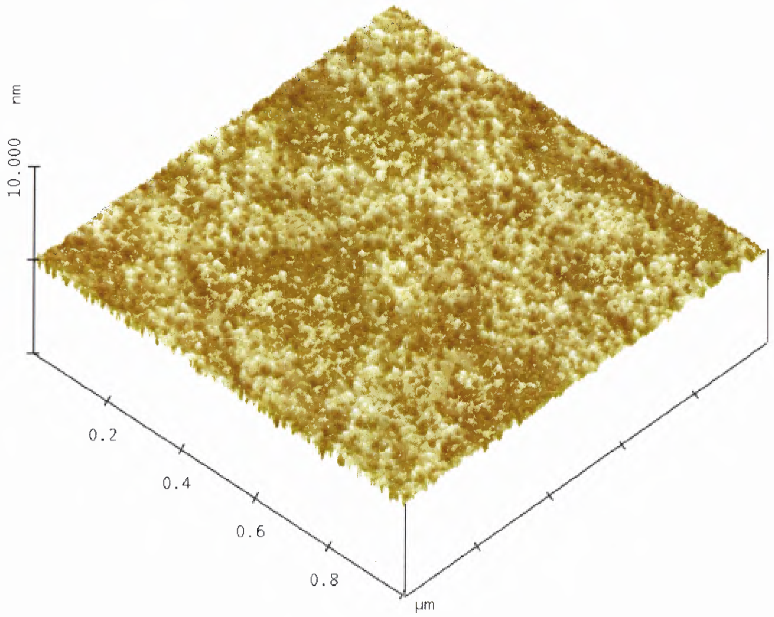

Figure 6.11 Average roughness of c-Si surface was decreased to R_a = 0.81 Å after irradiation with 12 keV $B_{10}H_x^+$ cluster ions.

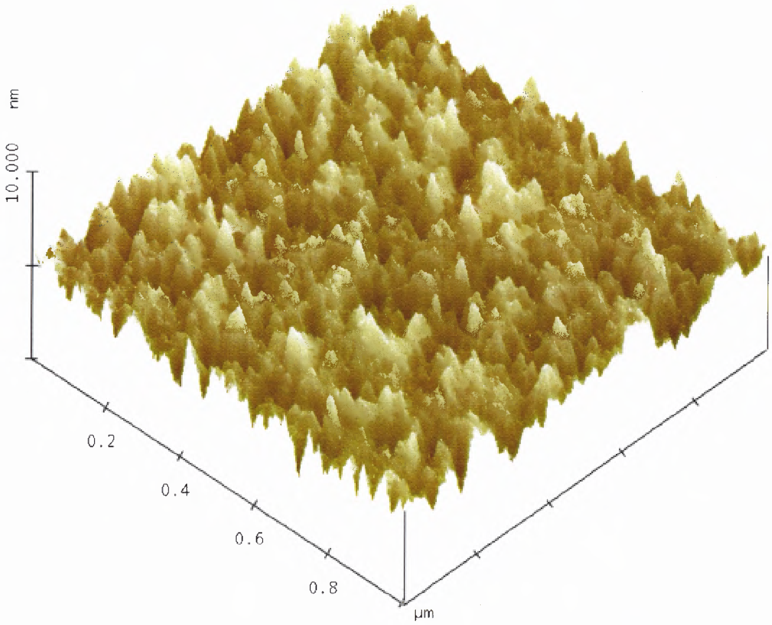

Figure 6.12 Average roughness of c-Si surface was increased to R_a = 5.1 Å after irradiation with 12 keV 12 keV monomer Ar$^+$ ions.

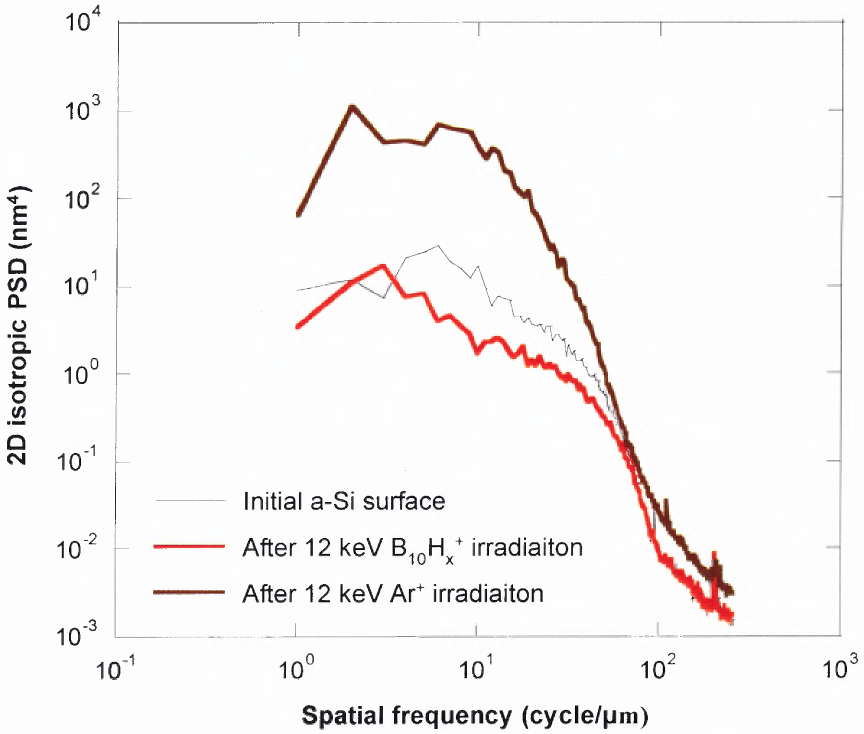

Figure 6.13 PSD of c-Si surface before and after irradiation with 12 keV $B_{10}H_x^+$ cluster ions and 12 keV monomer Ar$^+$ ions.

Decaborane cluster ions also showed a smoothing effect on a Ta films. For example, R_a decreased from 32.6 Å to 22.0 Å for a 10 μm × 10 μm scan (Figure 6.14) and R_a decreased from 30.1 Å to 23.1 Å for a 1 μm × 1 μm scan (Figure 6.15). The irradiated surface was still rather rough, which could be explained by the following reasons: 1) initial roughness of this film was an order of magnitude larger than that of the Si surfaces described previously, 2) Ta has much larger atomic mass and is not as easily sputtered as Si, or 3) boron could react with Ta to form a tantalum boride that is more sputter resistant than bare Ta. PSD comparisons for the 1 μm × 1 μm areas (see Figure 6.16) reveals that irradiation with decaborane cluster ions effectively reduced features of the spatial frequency range near 10 μm^{-1}. The results nevertheless show clearly the smoothing effect of irradiation by decaborane ions. The fact that the relatively small cluster ions have different effects than the monomer ions and that they can smooth surfaces of various materials may indicate their potential application for surface modification.

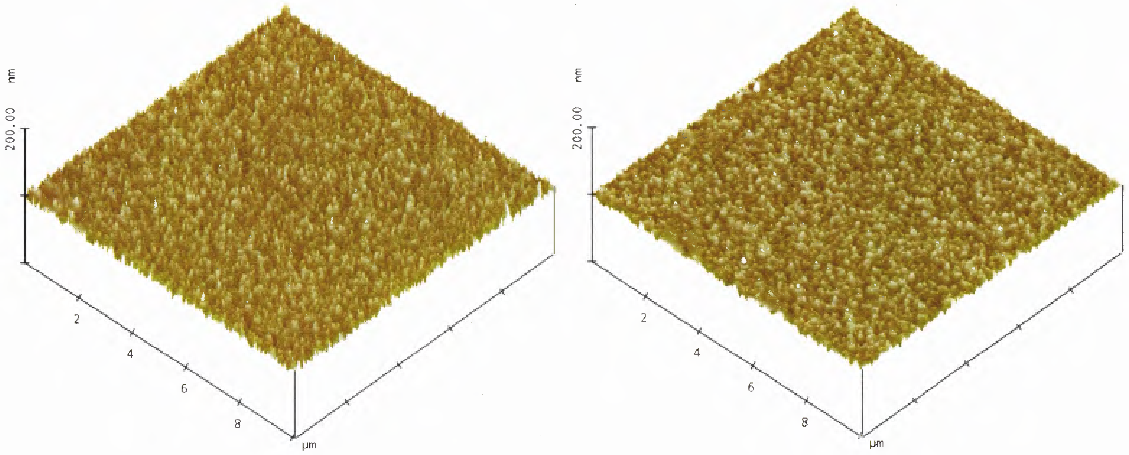

(a)

(b)

Figure 6.14 AFM images (10 □m × 10 □m scan) of a) initial Ta film surface and b) Ta film surface after irradiation with 12 keV $B_{10}H_x^+$ cluster ions.

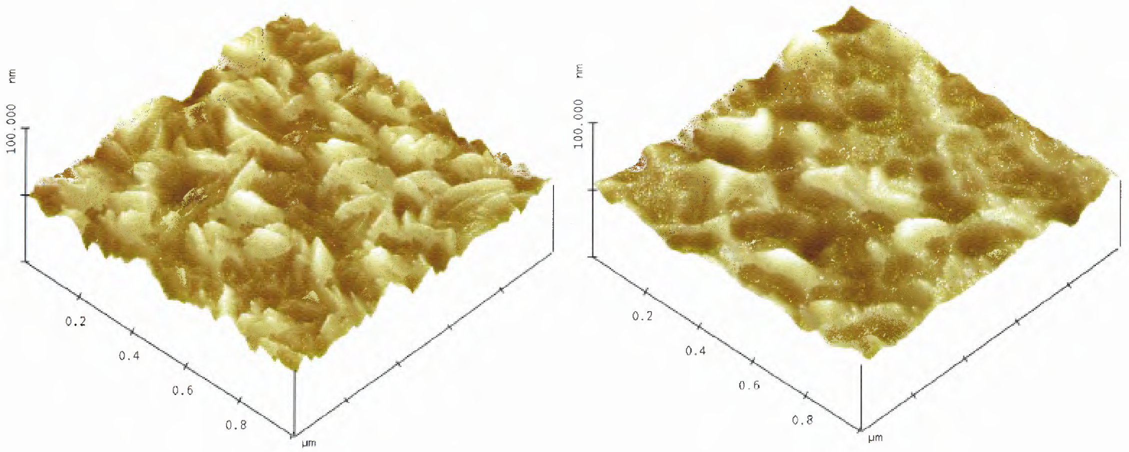

(a)

(b)

Figure 6.15 AFM images (1 □m × 1 □m scan) of a) initial Ta film surface and b) Ta film surface after irradiation with 12 keV $B_{10}H_x^+$ cluster ions.

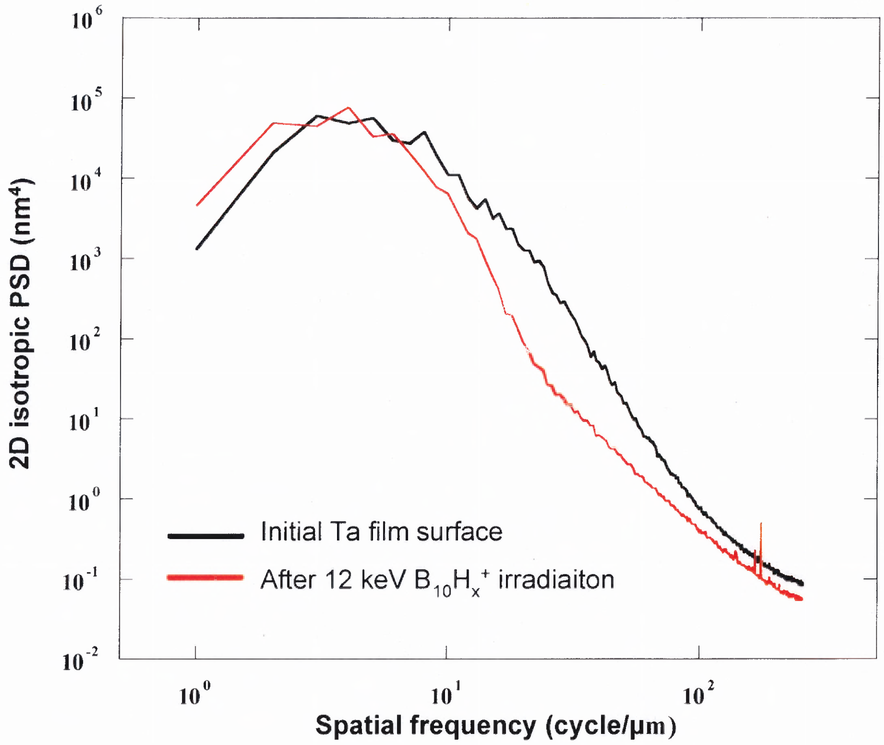

Figure 6.16 PSD comparison for Ta film (1 □m × 1 □m area) before and after irradiation with 12 keV $B_{10}H_x^+$ cluster ions.

AFM studies reveal that decaborane ion beams smooth various surfaces including a-Si, c-Si and a Ta film. Similar surface smoothing effects were only demonstrated by much larger gas cluster ions consisting of hundreds to thousands of atoms and have never been observed on metallic or semiconductor surfaces bombarded by monomer ions. The surface smoothing is a striking effect of cluster impact and it implies a fundamental difference in the projectile-solid interactions caused by the concentration of mass and energy of projectiles arriving in the form of clusters at a localized area of the surface.

CHAPTER 7

COMPUTER SIMULATIONS OF DECABORANE IMPACT ON SILICON

7.1 Introduction

This chapter describes a study of the impact process of decaborane cluster ions on Si surfaces, using molecular dynamics (MD) simulations. The impact of cluster ions, such as decaborane, may result in collision events that are quite different from those of energetic individual atoms or monomer ions. The study of the dynamics of the collision processes between a cluster and a solid surface may help to better understand the irradiation effects by decaborane cluster ions. Computer simulations can reveal details of the physical processes involved in the ion-solid interactions that cannot be obtained from experiments. Since a MD simulation numerically solves Newton's equation of motion for each atom in the simulated system, it provides information on the position and velocity for each atom at each time step during the system evolution after an impact. A number of valuable information can therefore be obtained from the MD simulation including, but not limited to, lattice damage, implant depth profile, and sputtering yield of target atoms.

7.1.1 Computer Simulation of Atomic Collision Processes in Solids

The collision process in a solid subjected to impact by energetic projectiles has been for a long time a topic of interest for physicists as well as materials scientists since this process determines the structure, composition and properties of the target material. In order to describe the motion of atoms in a solid, it is necessary to find the proper expression for the interatomic forces. For a collision process occurring in a solid impacted by atomic ions, the interatomic forces exerted on one atom may involve contributions from multiple atoms. Due to the complexity of the forces affecting one atom, these forces cannot be solved analytically except in some specific cases.

At the medium incident energy range (1 ~ 100 keV), however, the impact process can be described as a series of random collisions between a projectile and an atom in the solid. This is the so-called "binary collision" model. It is based on the fact that the range of a significant interatomic force for the collision is shorter than the distances of target atoms in the bulk because of the screening effect, and the collision only lasts the order of $\sim 10^{-15}$ s, which is much less than the period of lattice vibration. Lindhard *et al* [73] solved this random process analytically and obtained the range distributions of implanted atoms in a solid. Based on his linear cascade theory, Sigmund [74] developed the equation of transport of an energetic target atom in the solid and derived the formula expressing the sputtering yield dependence on incident energy of the projectile. These models showed good agreement with experimental results and contributed to the progress of ion beam engineering in industrial applications such as ion implantation and ion beam sputtering [75].

The binary collision process is usually simulated using Monte-Carlo (MC) codes. MC simulations make it possible to examine the evolution of a collision cascade, the formation of damage as well as ion-beam mixing and sputtering even for complex materials, which is difficult to solve analytically. Although a binary collision model was successful in analyzing the impact process of atomic ions, this method may not be suitable for studying impacts by cluster ions.

In order to analyze the impact of clusters onto solid, it is necessary to monitor the motion of all atoms involved in the collision process. This is accomplished by using a "molecular dynamics (MD)" simulation, where the evolution of a set of interacting atoms in a system is followed by numerically solving their Newton's equations of motion. Therefore, in contrast with the Monte-Carlo method, molecular dynamics is a deterministic technique: given an initial set of positions and velocities, the subsequent time evolution is in principle completely determined. MD simulation can provide space coordinates and velocities of both the projectiles and the target atoms at times in the order of 10^{-15} s [femtosecond: fs] to 10^{-12} s [picosecond: ps]. It is a suitable method to analyze the atomic collision processes with high time and space resolution, but it requires by far larger computational resources than does the Monte-Carlo method under the binary collision approximation.

7.1.2 Integration Algorithm in MD Simulation

In molecular dynamics, atoms interact with each other under the action of instantaneous forces. As the atoms move, their relative positions change and forces change as well. The motion follows the classical Newton's equation given by:

$$\frac{dv(t)}{dt} = \frac{d^2r(t)}{dt^2} = \frac{F}{m} \tag{7.1}$$

where F is the force acting on the object, which has mass m, velocity v and coordinate r at time t. Knowing positions and some of their time derivatives at time t, integration of equation (7.1) over a finite time step Δt gives the same quantities at a later time $t + \Delta t$. By iterating the procedure, the trajectories of interacting atoms can be followed for long times. The *Verlet* algorithm is the most commonly used time integration method in MD simulation [76]. The basic idea is to approximate the coordinates at time $t - \Delta t$ and $t + \Delta t$ by using Taylor's expansions with Equation (7.1) and to calculate the coordinate $r(t + \Delta t)$ from $r(t)$ and $r(t - \Delta t)$:

$$r(t \pm \Delta t) \approx r(t) \pm v(t)\Delta t + \frac{F(t)}{2m}\Delta t^2 \tag{7.2}$$

$$r(t + \Delta t) = 2r(t) - r(t - \Delta t) + \frac{F(t)}{m}\Delta t^2 \tag{7.3}$$

A problem with this method is that the velocities that are needed to compute the kinetic energy are not directly generated. One could compute the velocities from the positions by using:

$$v(t) = \frac{r(t + \Delta t) + r(t - \Delta t)}{2\Delta t} \tag{7.4}$$

However, the error associated to this expression is of order of Δt^2. To overcome this difficulty, some variants of the *Verlet* algorithm have been developed. The *leap-frog* algorithm is one of such variants where velocities are handled somewhat better:

$$r(t + \Delta t) = r(t) + v(t + \frac{\Delta t}{2})\Delta t \tag{7.5}$$

$$v(t + \frac{\Delta t}{2}) = v(t - \frac{\Delta t}{2}) + \frac{F(t)}{m}\Delta t \tag{7.6}$$

In the *leap-frog* method, both the position and velocity can be stored and their time evolution can be calculated. During each time step, the velocity for the current time t is obtained by interpolation:

$$v(t) = \frac{v(t + \frac{\Delta t}{2}) + v(t - \frac{\Delta t}{2})}{2} \tag{7.7}$$

An even better implementation of the same basic algorithm is the so-*called velocity Verlet* scheme, where positions and velocities at time $t + \Delta t$ are obtained from the same quantities at time t in the following way:

$$r(t+\Delta t) = r(t) + v(t)\Delta t + \frac{F(t)}{2m}\Delta t^2 \tag{7.8}$$

$$v(t+\Delta t) = v(t) + \frac{1}{2m}[F(t) + F(t+\Delta t)]\Delta t \tag{7.9}$$

The forces used in MD simulations are calculated from interatomic potentials. The potentials used in this work are described in section 7.2.1.

7.2 Simulation Model

7.2.1 Interatomic Potentials

For MD simulations, the force acting upon a particle i is derived from a potential energy function which depends on the particle coordinates:

$$F_i = -\frac{\partial}{\partial r_i} V(r_1, r_2 \ldots) \tag{7.10}$$

The total potential can be expanded according to the number of the atoms involved in the interactions, as given by:

$$V(r_1, r_2 \ldots) = \sum_i V_1(r_i) + \sum_{i<j} V_2(r_i, r_j) + \sum_{i<j<k} V_3(r_i, r_j, r_k) + \ldots \tag{7.11}$$

The first term in Eq.(7.11) normally represents the effects of external forces that are absent for an isolated system. The rest of the terms stands for interactions among particles. The terms V_2 and V_3 are for 2-body and 3-body potentials, respectively. The interatomic potential models employed in this study are described as follows.

ZBL potential

For the collision process at the energy range from several eV to several tens of keV, the interaction between two atoms can be described by the Coulomb potential taking into account the screening effect. The screening effect represents the fact that at intermediate distance the Coulomb potential between nuclei of two atoms is reduced by the space charge of the innermost electron shells. The screened Coulomb potential is given by:

$$V(r) = \frac{Z_1 Z_2 e^2}{4\pi\varepsilon r}\chi(r) \tag{7.12}$$

where Z_1 and Z_2 are the atomic numbers of the two atoms, $\chi(r)$ is the screening function and is defined as the ratio of the actual atomic potential, at some radius r, to the Coulomb potential. Ideally, it properly moderates the Coulomb potential to describe the interaction between two atoms at all separation distance. For large distance, $\chi(r)$ should go to zero, while for very small distance, $\chi(r)$ should go to unity. One widely accepted form of the screening function is the so-called ZBL model developed by J. F. Zeigler, J. P. Biersack and U. Littmark [32]. In the ZBL model, the screening function, $\chi_{ZBL}(r)$, is given as the function of the interatomic distance r and universal screening length a_U:

$$\chi_{ZBL}(r) = \sum_{i=1}^{4} c_i \exp(-d_i \frac{r}{a_U}) \tag{7.13}$$

$$a_U = \frac{0.8854 a_0}{(Z_1^{0.23} + Z_2^{0.23})} \tag{7.14}$$

where $a_0 = 0.0529$ nm is the Bohr radius of the hydrogen atom. The pair parameters (c_i, d_i) are shown below. Note that the summation of c_i ensures that $\chi(r)$ tends to unity for very small distance r.

$$\begin{pmatrix} c_i \\ d_i \end{pmatrix} = \begin{pmatrix} 0.02817, 0.2802, 0.5099, 0.1818 \\ 0.2016, 0.4028, 0.9423, 3.2000 \end{pmatrix} \quad i = 1,2,3,4 \qquad (7.15)$$

Stillinger-Weber potential

Systems of practical interest such as metals and semiconductors cannot be modeled only with pair-wise forces. For example, Si undergoes a series of structural transitions under pressure, which indicates that the cohesive energy is nearly independent on coordination, while a two-body model should favor the more packed structures, which have bonds. Therefore, many-body terms in Eq. (7.11), which represent the effect of the coordination of atomic bonds, should be considered in order to model the dynamics in solids like Si. The model developed by Stillinger and Weber [77] has been widely used to describe interactions in both solid and liquid forms of Si. The Stillinger-Weber (S-W) potential comprises both 2- and 3-body contributions. The pair potential is given by:

$$V_2(r_{ij}) = \begin{cases} \varepsilon A[B(r_{ij}/\sigma)^{-p} - (r_{ij}/\sigma)^{-q}]exp[(r_{ij}/\sigma - a)^{-1}] & r_{ij} < a \\ 0 & r_{ij}/\sigma \geq a \end{cases} \qquad (7.16)$$

where $\varepsilon = 2.17$ eV and $\sigma = 0.29051$ nm are energy unit and length unit, respectively. This potential automatically cuts off when the reduced distance $r = r_{ij}/\sigma$ reaches a without any discontinuities in any r derivatives, which is a distinct advantage in any molecular dynamics simulation study. The same advantage is extended to the three-body interactions as given by:

$$V_3(r_i, r_j, r_k) = h(r_{ij}, r_{ik}, \theta_{jik}) + h(r_{ji}, r_{jk}, \theta_{ijk}) + h(r_{ki}, r_{kj}, \theta_{ikj}) \qquad (7.17)$$

where θ_{jik} is the angle between $\mathbf{r_j}$ and $\mathbf{r_k}$ subtended at vertex i, etc. Provided that both r_{ij} and r_{ik} are less than the cutoff distance $a\sigma$, the function h has the following form:

$$h(r_{ij}, r_{ik}, \theta_{jik}) = \lambda \exp[\gamma(r_{ij}/\sigma - a)^{-1} + \gamma(r_{ik}/\sigma - a)^{-1}] \times (\cos\theta_{jik} + \tfrac{1}{3})^2 \tag{7.18}$$

Eq. (7.18) gives the minimum value of zero at $\cos\theta_{jik} = -1/3$, which means that the three-body term favors the tetrahedral structure expected in the Si lattice, whereas the two-body term reflects the effect of bond length σ and the binding energy ε in Si. The parameters used in the S-W model are summarized in Table 7.1.

In the simulations reported in this dissertation, interactions between two and three Si atoms are evaluated with the S-W potential. Many MD simulations of high-energy B implantation into Si have used only the ZBL repulsive forces between B and Si atoms. This may not be suitable for shallow implantation with cluster ions where the energy per B atom is much lower. Since it is known that B atoms often take up substitutional sites within Si lattice, they must have some binding potential to the lattice. As was suggested in Ref [34], the interaction between B dopant and Si host atoms was modeled with the ZBL screened Coulomb potential at short distance (r < 1.1 Å), joined to a Morse-type potential at long distance (r > 1.8 Å). The binding of B to the Si lattice was taken into account in the Morse potential by a dimmer binding energy D_m = 0.25 eV:

$$V_M = D_m\{exp[-2\beta(r - r_{eq})] - 2\,exp[-\beta(r - r_{eq})]\} \tag{7.19}$$

where r_{eq} = 2.351 Å is the nearest-neighbor spacing of the Si atoms in the lattice, and β =1.5 is the decay length of the function.

Table 7.1 Parameters in the S-W Potential for Si

ε(eV)	2.17	σ(nm)	0.20951
p	4	q	0
A	7.049556277	B	0.6022245584
λ	21.0	γ	1.20
a	1.8		

To account for the weak bonding in the molecule-like structure in a B_{10} cluster, the pair interaction between two B atoms was modeled via the modified Buckingham exponential-6 potential as following:

$$V_2(r_{ij}) = \begin{cases} \dfrac{\epsilon}{1-6/\alpha}\left\{\dfrac{6}{\alpha}\exp\left[\alpha\left(1-\dfrac{r_{ij}}{r_m}\right)\right] - C\left(\dfrac{r_{ij}}{r_m}\right)^6\right\} & \text{for } r_{ij} > r_{max} \\ \infty & \text{for } r_{ij} < r_{max} \end{cases} \tag{7.20}$$

where ϵ, α, r_m and C are model parameters. Parameter r_m is the radial distance at which the potential has a minimum. The cutoff distance r_{max} is the smallest positive value for which $dV/dr = 0$ and is obtained by an iteration solution of equation (7.20). The reason a cutoff distance is required is that at very short distances, the original Buckingham exponential-6 potential becomes negative.

7.2.2 Simulation System

The physical model for the simulations reported in this dissertation was originally developed by Z. Insepov [35, 36] and modified to meet the specific needs of the current study. This model combines conventional atomistic MD, for the central collision region, with a continuum thermodynamic representation for the rest of the system. Figure 7.1 shows the schematic of the model system. The central region is a tall cylinder consisting of ~ 53, 000 Si atoms arranged in the diamond lattice with a (001) top surface. Atoms in the cylinder are free to move except those in the two bottom mono-layers which are fixed. Thermal boundary conditions (TBC) were used instead of periodic boundary conditions (PBC) in the model. The region outside the cylinder radius was divided into symmetrical finite element cells that served to control the energy flow through energy absorbing walls, which was simulated by linear thermal diffusion equations. The boundary conditions for computation of thermal diffusion equations are as follows: the

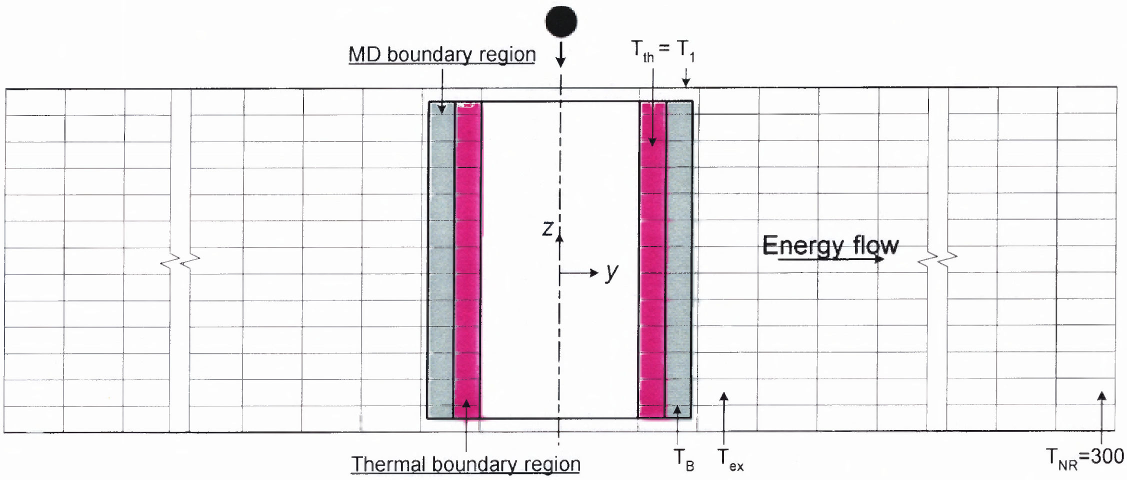

Figure 7.1 Schematic drawing of the system for MD simulation of B_{10} cluster impact on a Si target. The central collision region was simulated with conventional MD, while the outer region was modeled by continuum thermodynamics. The two regions were coupled by the temperature at the MD thermal boundary layer and at the inner layer of the thermal mesh cells.

temperature at the far radius of the mesh structure, T_{NR}, was kept constant at room temperature (300 K); and the temperature of the inner mesh layer, was set to be equal to the MD parameter, T_{th}. At each time step, parameter T_{th} was obtained by taking an average along the *z* direction in the MD thermal boundary layer. The temperature of each mesh cell was calculated from the temperatures of its four neighboring cells. The averaged temperature from the second inner mesh layer, T_{ex}, was considered as the external temperature for the MD part and used to scale the velocities of target atoms in the boundary layer using a scaling factor given by:

$$fac = \left(T_{ex} / T_B\right)^{1/2} \tag{7.21}$$

$$v_{i,new} = fac \times v_i \tag{7.22}$$

where T_B is the averaged temperature in the MD boundary layer and v_i and $v_{i,new}$ are the velocities of *ith* MD boundary atom before and after scaling, respectively. This hybrid method of combining MD with a continuum finite element model significantly reduces the required system size. It can account for the energy flow through the MD boundaries and avoids reflections of shock waves that would generate nonphysical conditions in the simulations.

For simplification purposes, the decaborane cluster ion bombarding the Si target surface was modeled as a cluster of ten B atoms. The hydrogen atoms were not included since a hydrogen atom only carries $< 1\%$ of the total cluster energy and has over ten times smaller mass and is expected to have a negligible effect on the collision events. The B_{10} cluster was represented as a sphere of FCC structure. The distance between two neighboring B atoms was 1.51 Å, which is equal to the average B-B bond length in a decaborane molecule.

7.2.3 Description of Simulations

In this simulation work, normal impacts on Si substrate by B_{10} clusters and B monomers with the incident energy of 500 eV/atom were studied.

To obtain statistical properties such as depth profiles of implanted B atoms and Si sputtering yields, ten simulations were performed for normal impacts of B_{10} clusters. Before each impact, a random orientation of the cluster was chosen and the x-y center of the cluster was aligned to the center of the MD cylinder.

Fifty simulations were performed for normal impact by B monomers. All starting x-y coordinates of B monomers were randomly selected within a 2.71 Å × 2.71 Å square at the center of the MD cylinder. Figure 7.2 shows the starting x-y coordinates for 50 B monomers and for 100 B atoms in ten B_{10} clusters.

As for B_{10} cluster impact, the simulations were carried out to at least 0.92 ps. The program was stopped if the kinetic energy of every B atom inside the target was less than 0.5 eV. In case of single B impact, the program was stopped if the B kinetic energy dropped below 0.1 eV.

The MD simulations were performed on three nodes of a Linux client-server system in the Physics Department of NJIT, at a speed of ~10 steps per minute. Each computing node has a 1 GHz Intel Pentum4® CPU and 1 GB physical memory (RAM). The incremental time step was so fine ($\Delta t = 7.7 \times 10^{-17}$ s) that a projectile would advance by no more than 1/10 of the thickness of a Si (001) monolayer during one step, which ensured high resolution of space evolution. During each time step, the force acting upon one atom was calculated from its potential interactions with all its surrounding atoms within the cutoff radius. Positions (x, y, and z coordinates) and kinetic energies of all B and Si atoms were stored into data files at specific time intervals. To monitor the evolution of target sputtering, numbers of sputtered Si atoms were also recorded at shorter time intervals. The definition of sputtered Si is described in section 7.3.3.

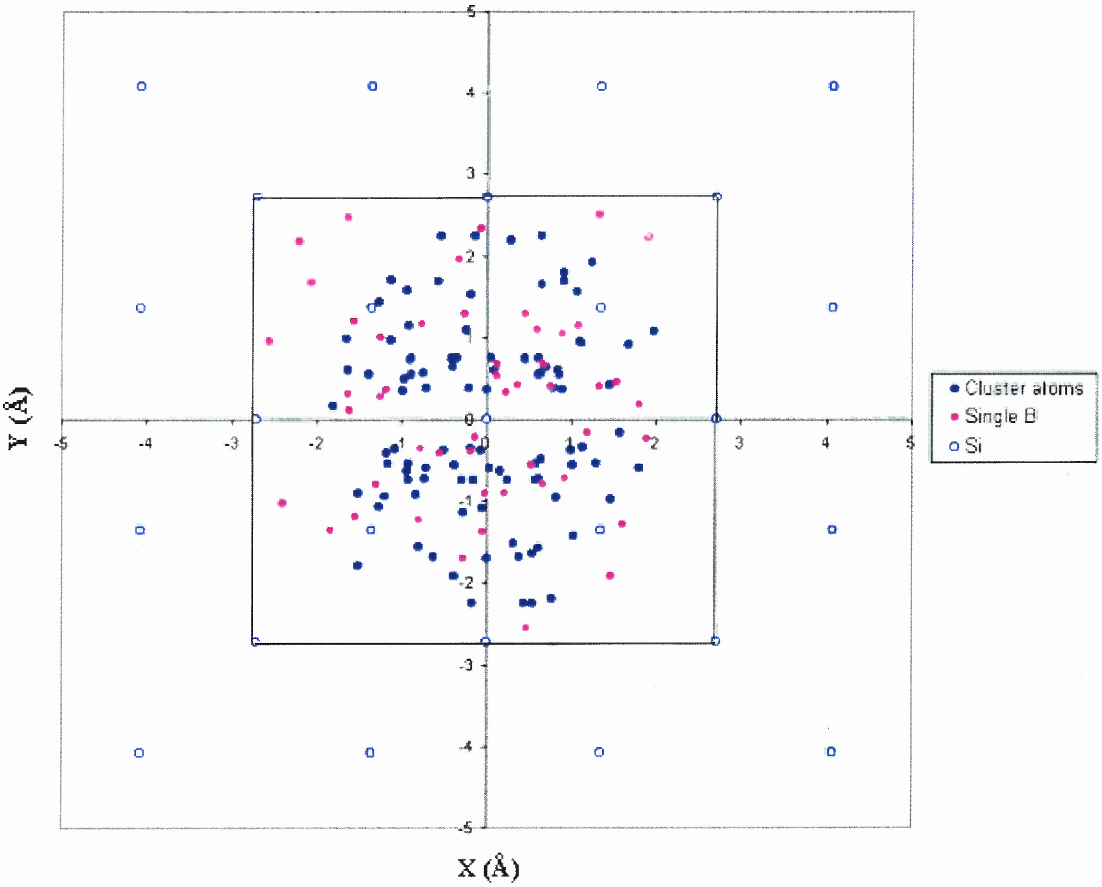

Figure 7.2 Starting positions of the B projectiles in the MD simulations.

7.3 Simulation Results and Discussion

7.3.1 Depth Distributions of Implanted Boron Atoms

B depth profiles from B monomer impacts and from B_{10} cluster impacts are shown in Figure 7.3 and 7.4, respectively. Each column in the figure gives the percentage of B atoms within a 5 Å range of depth. The left-most column at a negative depth range represents the percentage of back scattered B.

The mean depth of the B atoms was 37.3 Å with a standard deviation (STD) of 16.4 Å for B_{10} cluster impacts, and was 45.2 Å with a STD of 43.9 Å for B impacts. With B_{10} clusters, the peak of the depth distribution of implanted B atoms was between 20 to 25 Å. With B monomers, however, the peak was not well defined and the depth data were more scattered. This may be due in part to the lower statistic of B monomers (50 atoms) in comparison to that of B_{10} impacts (100 atoms). It can be noticed, however, that more monomer projectiles (16%) were implanted into depths > 85 Å than in the case of cluster impacts (9%). This is probably because of the channeling effect: with the ion beam perpendicular to the (001) surface of the target, some of the B projectiles may have impacted the surface close to the center of <001> channels. These projectiles did not make close impacts with the lattice Si atoms and had a much lower rate of energy loss, hence penetrated deeper into the target. In the cluster case, on the other hand, many simultaneous collisions near the surface at the beginning of the impact made the channeling effect less effective.

As also can be seen from the figures, B monomers showed somewhat smaller backscattering than B atoms in B_{10} clusters. Among 50 B monomer projectiles, only 2% were back scattered, while in cluster impact about 10% of the B atoms were back scattered.

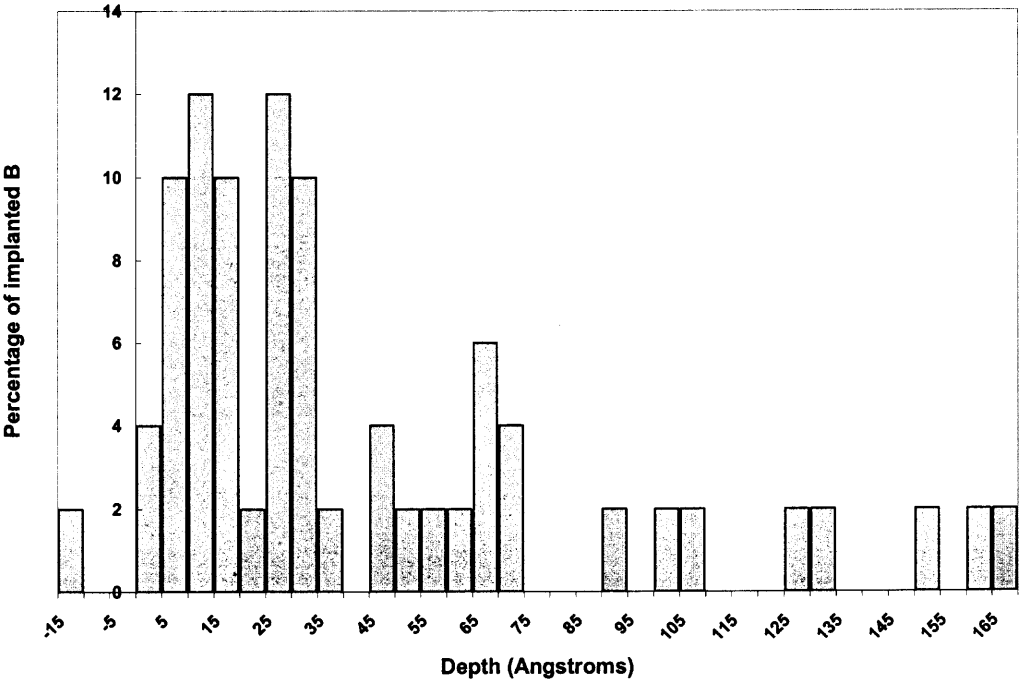

Figure 7.3 Depth profiles of B atoms in Si impacted by 0.5 keV B monomers.

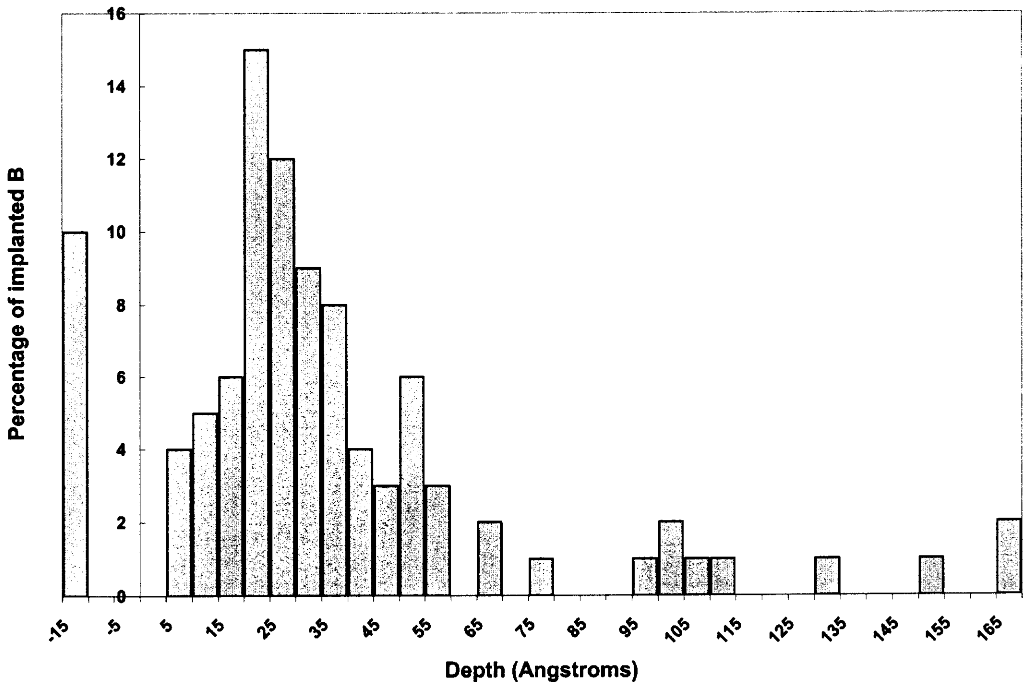

Figure 7.4 Depth profiles of B atoms in Si impacted by 5 keV B_{10} clusters, giving 0.5 keV per B atom, the same as for Fig. 7.3.

Figure 7.5 shows the B depth distributions in Si implanted with 0.5 keV B^+ ions, which was obtained from a TRIM simulation [78]. It is similar to that for B_{10} cluster impacts as shown in Figure 7.4. The B range is 39 Å, which is also very close to the mean B depth for B_{10} cluster impacts obtained from MD simulations.

These simulation results suggest that B implantation with B_{10} clusters lead to essentially the same depth of implanted atoms as with B monomers, which is in agreement with what had been observed with implantation experiments [16, 19, 24].

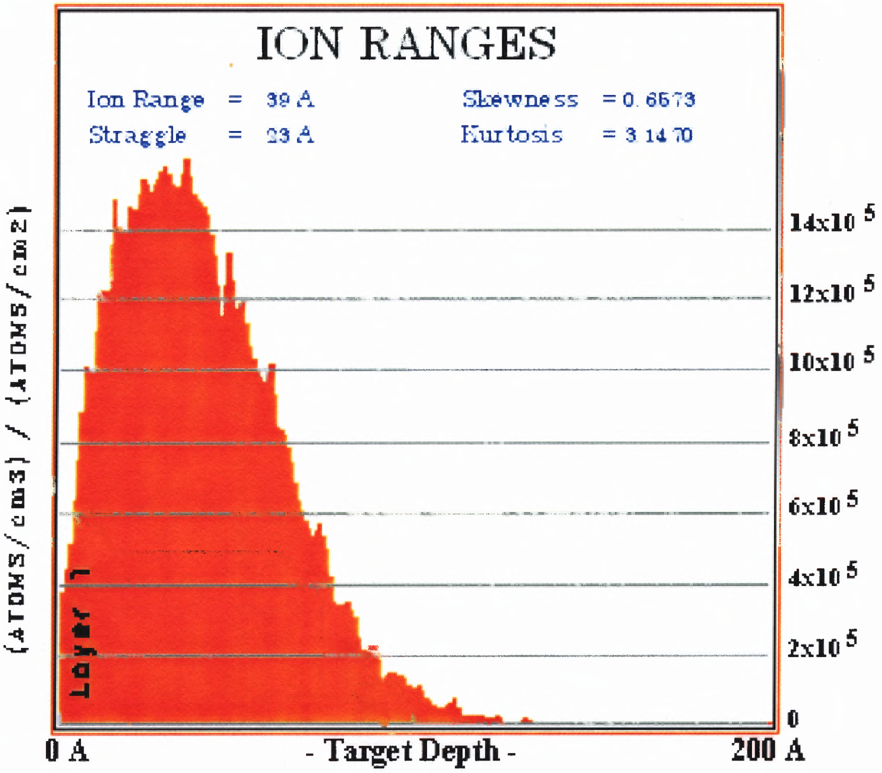

Figure 7.5 Depth profile of 0.5 keV B^+ in Si obtained from a TRIM simulation.

7.3.2 Evolution of Collision Cascades

The evolution of a typical B_{10} cluster impact event is shown in Figure 7.6. The atoms shown are within a (100) cross-sectional slab of thickness 3*As*, where *As* = 5.43 Å is the Si lattice constant. Figure 7.6 (a) to (d) are the side views of the slab at 58 fs (≈0.06 ps), 0.15 ps, 0.38 ps, and 1.54 ps after the impact. Figure 7.7 shows the side views 39 fs and 0.19 ps after a typical B monomer impact. In these figures, large solid circles represent implanted B atoms and Si atoms are illustrated as small open circles.

A significant loss of crystalline order of the target (lattice disorder) due to large energy deposition by cluster impact is clearly evident in Figure 7.6 (a). Disintegration of the cluster into constituent B atoms soon after the impact is also seen. The B atoms then interacted independently with the Si atoms. The cluster impact causes many target atoms to be displaced from their lattice sites, with each displacement requiring on the average around 15 eV energy. Most of the collisions occurred at a region near the surface and a crater-shaped disordered zone is seen formed under the surface. The impinging cluster transfers energy to the target atoms not only vertically but also radially. In Figure 7.8, the kinetic energy is plotted against the depth for all ten B atoms for the time period shortly (58 fs) after the impact. It shows that B atoms closer to the surface had already lost most of their kinetic energy. These B atoms have hard collisions with Si atoms and transfer much of their energy to them. On the other hand, two B atoms at depth > 45 Å only lost less than 10% of the initial kinetic energy.

In contrast, a B monomer impact of the same energy per atom causes much less damage to the Si lattice, as shown in Figure 7.7. The displacements of Si atoms were along the trajectory of the incident B atom.

The size of the disordered zone increases with elapsed time, as the cluster energy further spreads and displaces the target atoms. As shown in Figure 7.6 (b), while severe collisions between Si atoms continued in the sub-surface region, traces of lattice damage also could be seen in a deeper region accompanying those B atoms that moved. At this time, the energy carried by the cluster has been almost completely transferred to the Si target, as is evident in the kinetic energy vs. depth plot in Figure 7.9.

Later (> 0.15 ps), the B atoms deep inside the target were virtually stopped. The deposited energy, however, continues to create a large number of Si atoms to be displaced and recoiled to the surface. While more Si atoms were ejected from the bulk, some of the mobile Si atoms were moved toward the rim of the crater. Two B atoms were also removed from the target, as shown in Figure 7.6 (c) and (d). The removal of implanted B has been observed previously by B retained dose experiments and was expected to limit the obtainable B dose in Si [31]. Comparison between Figure 7.6 (c) and (d) also indicates gradual recovery of the damaged region inside the substrate.

A prolonged simulation (up to 4.6 ps) indicates that a crater remains on the Si surface after a B_{10} cluster impact. Figure 7.10 shows the side view of the (100) Si cross-sectional slab at 4.6 ps after a B_{10} cluster impact. As can be seen in Figure 7.10, some recoiled Si atoms have accumulated to form the rim of the crater. Analysis to the data indicated that those Si atoms in the center of the crater had negligible z-components of momentum and they tended to move laterally. Figure 7.11 is the top-view of the configuration of Si atoms within a 5.43 Å distance below the surface for the same moment. It clearly shows a crater with dimensions much larger than the initial cluster size. The crater formation is a unique feature of cluster impacts and has not been found in any impacts by monomer B atoms. Crater formation on Si surfaces impacted by larger clusters, such as Ar gas clusters and C_{60}, has been predicted by MD simulations [37, 79, 80]. Recently, craters by 24 keV Ar_{135} cluster impacts on Si (100) and Si (111) surfaces have been observed by Atomic Force Microscopy (AFM) and high-resolution transmission electron microscope (HRTEM) cross section imaging [43]. This work shows for the first time that craters are formed after impact of such small cluster as B_{10}.

Figure 7.12 compares the time evolution of the mean B kinetic energy for B monomer impacts and B_{10} cluster impacts. In both cases, almost all of the incident energy carried by the B atoms had been transferred to substrate atoms at a time about 0.2 ps. As can also be seen in the figure, the projectile energy loss process is only slightly faster in the cluster case. This also suggests that each B atom in the cluster interacted with the substrate Si atoms independently, which could explain the similarity of depth profiles of B implanted with monomer B ions and with cluster ions of equivalent energy.

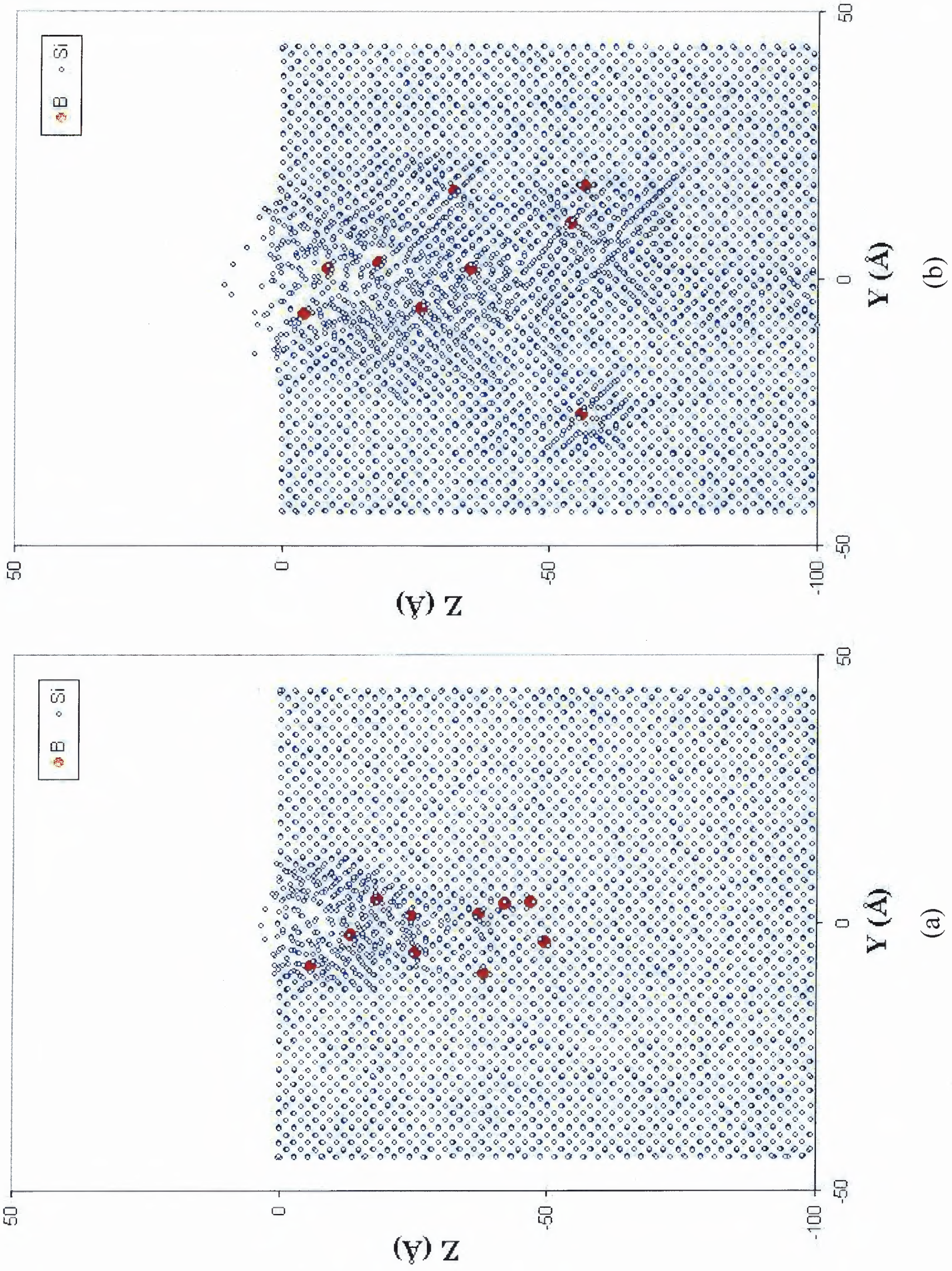

Figure 7.6 Side-views of a (100) cross-sectional slab of the Si target at (a) 58 fs, (b) 0.15 ps, (c) 0.38 ps, and (d) 1.54 ps after a B_{10} cluster impact.

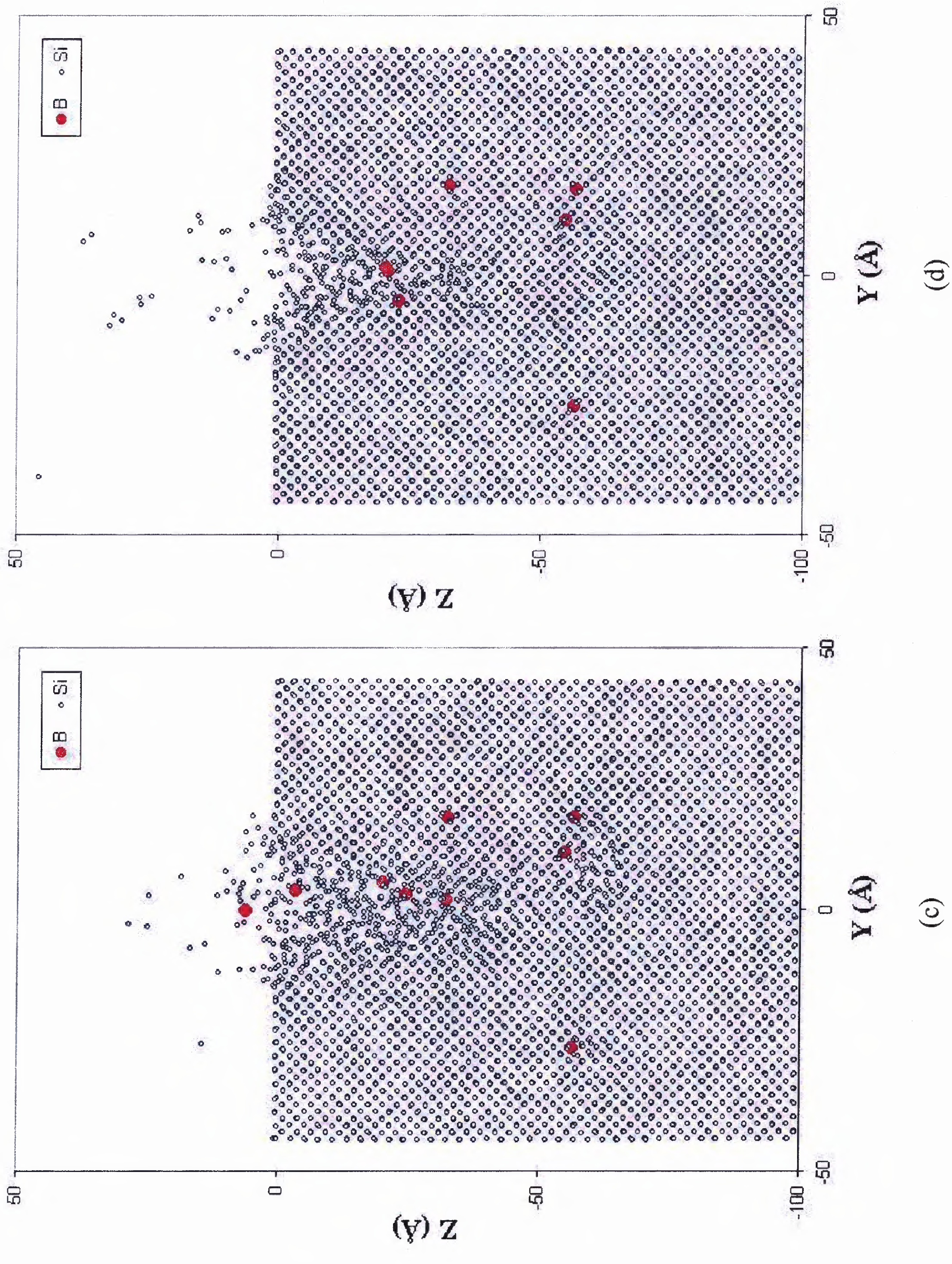

Figure 7.6 Side-views of a (100) cross-sectional slab of the Si target at (a) 58 fs, (b) 0.15 ps, (c) 0.38 ps, and (d) 1.54 ps after a B_{10} cluster impact (continued).

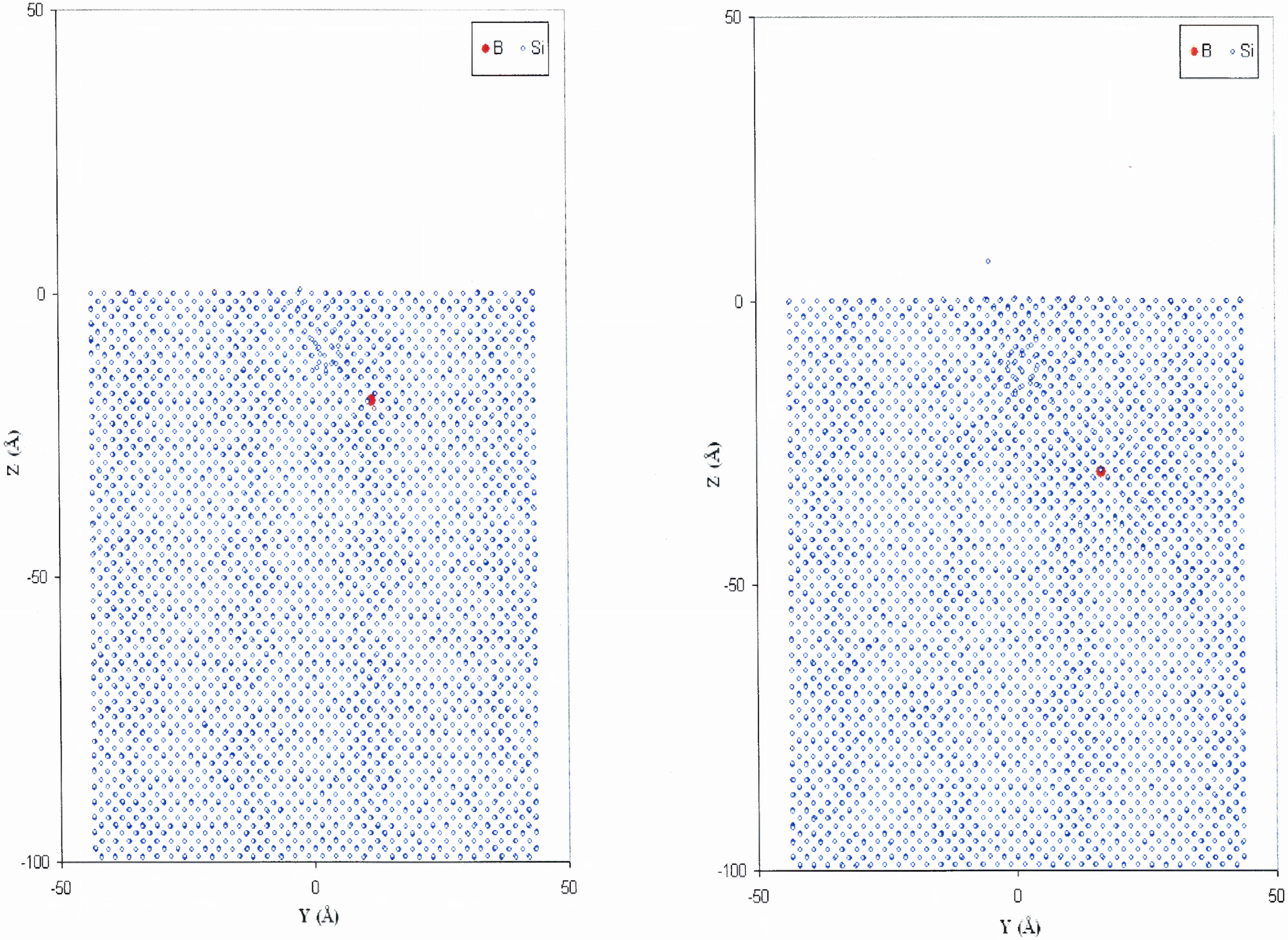

(a)

(b)

Figure 7.7 Side-views of a (100) cross-sectional slab of the Si target at (a) 39 fs, and (b) 0.19 ps after a 0.5 keV B monomer impact.

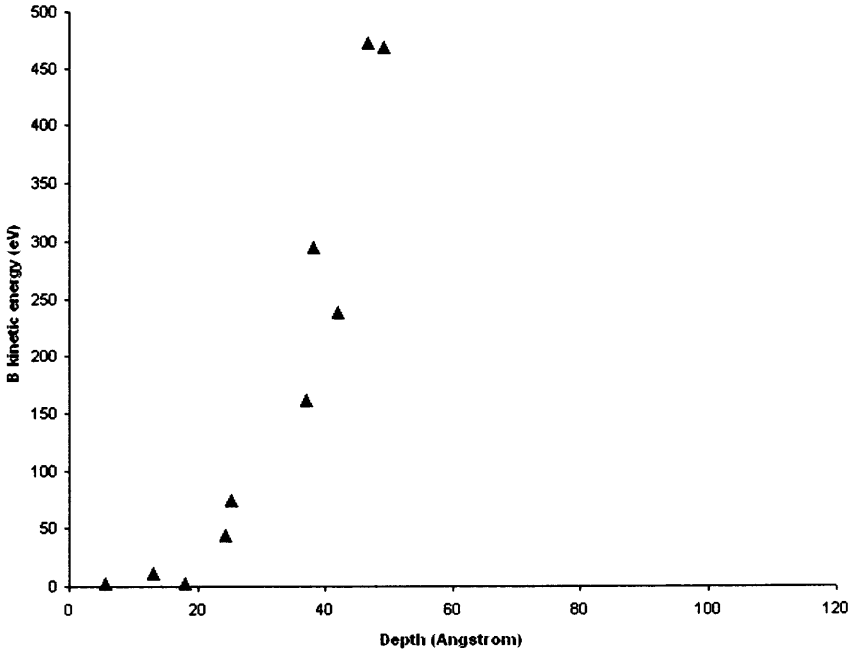

Figure 7.8 Kinetic energy vs. depth in Si for ten B atoms 58 fs after a B_{10} cluster impact.

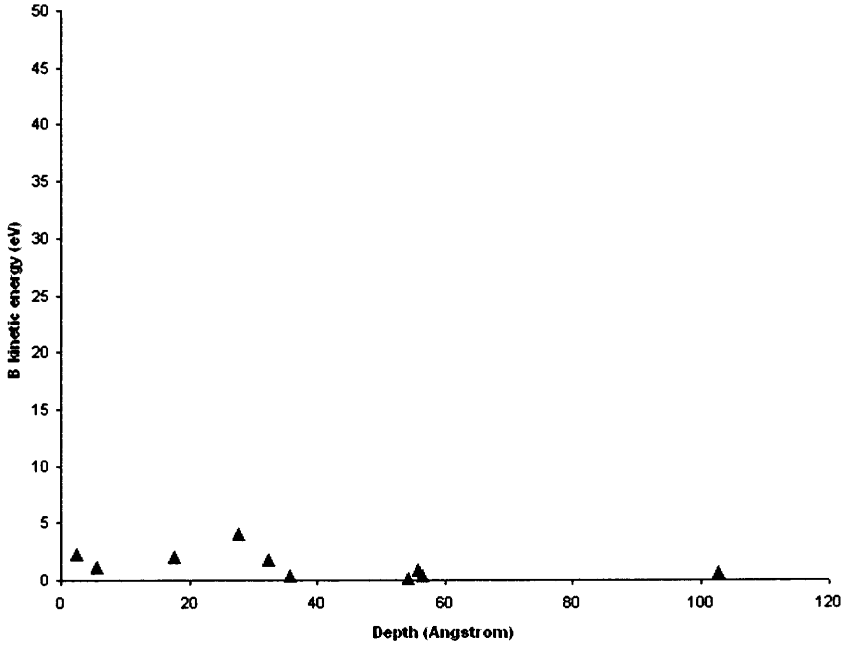

Figure 7.9 Kinetic energy vs. depth in Si for ten B atoms 0.15 ps after a B_{10} cluster impact.

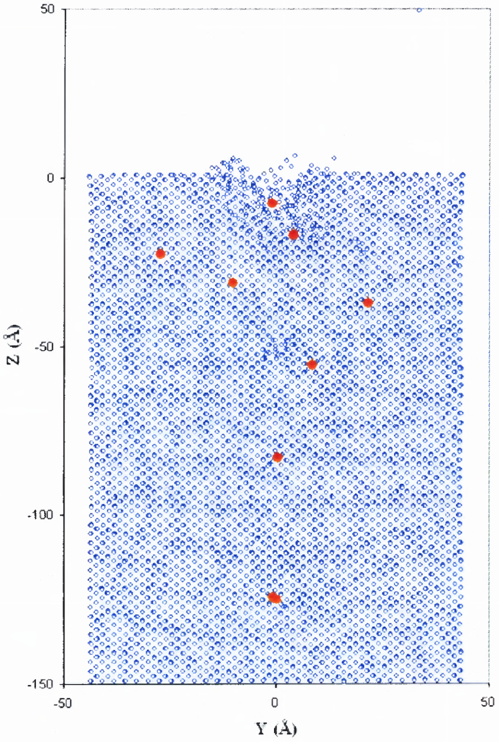

Figure 7.10 Side view of a (100) cross-sectional slab of the Si target at 4.6 ps after a B_{10} cluster impact.

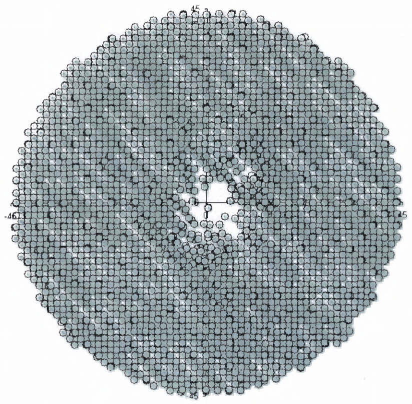

Figure 7.11 Top view of a (001) slab of the Si target at 4.6 ps after a B_{10} cluster impact. The thickness of the slab is the same as that of a Si unit cell (5.43 Å).

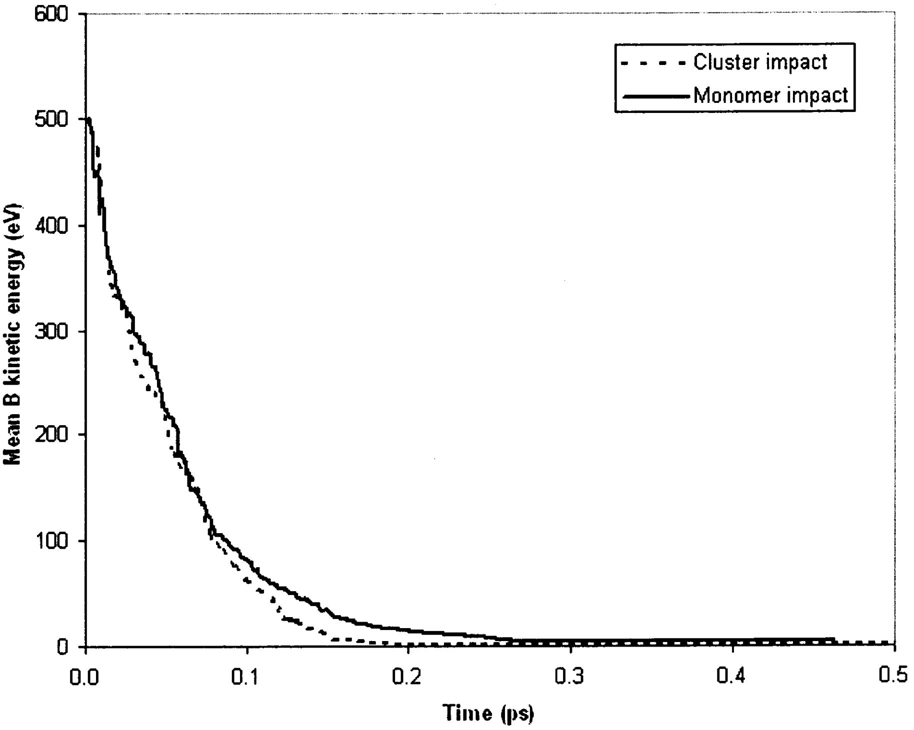

Figure 7.12 Time dependence of mean B kinetic energy for B monomer impacts and B_{10} cluster impacts.

7.3.3 Sputtering of Si by B_{10} Clusters

Sputtering of Si by B_{10} cluster impacts was also examined in this simulation work. The sputtering yield of Si was defined as the mean number of sputtered Si atoms per B atom of the cluster ion projectile. A silicon atom was considered to be sputtered if its distance from the surface was more than a control distance z_{cut} and its z-component of velocity was positive (directed out of the surface). It may be expected that with a proper choice of the control distance z_{cut} the sputtering yield should saturate after long-time simulation. Figure 7.13 shows the time dependence of the sputtering yield of Si by B_{10} clusters averaged for 10 cluster impacts for two different control distances (9 Å and 4.5 Å). The sputtering yield increases with time as more Si atoms leave the surface after the impact.

For smaller control distance (z_{cut} = 4.5 Å), the sputtering yield continues to increase even after 1 ps, while at z_{cut} = 9 Å it appears to be already saturated. This indicates that the dynamic process on the surface lasts for some time. Some of the ejected Si atoms having low kinetic energy would be affected by the surface potential and oscillate above the surface instead of being sputtered. The sputtering yield of Si with B_{10} clusters, obtained as the saturated value at z_{cut} = 9 Å, was 2.8 sputtered Si atoms per B atom in a B_{10} cluster and more than 4 for z_{cut} = 4.5 Å.

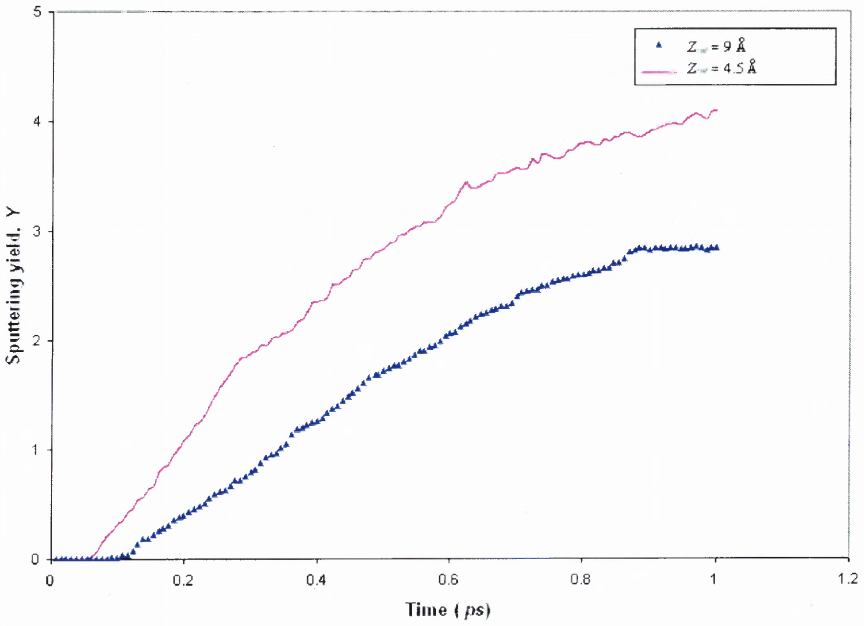

Figure 7.13 Time dependence of the sputtering yield of Si by 5 keV B_{10} clusters, obtained at two different control distances above the target surface.

It is interesting to compare the sputtering of Si by B_{10} clusters to that by B monomers. Using the same control distance (9 Å), the sputtering yield of Si with B monomers was calculated to be 0.04, which is about *70* times smaller than with B_{10} clusters. The large difference in simulated sputtering yield of Si by the two types of projectile is probably related to simultaneous impact of 10 times more atoms by a B_{10} cluster than by a B monomer with the same energy per atom. A cluster impact produces many more collisions and significant disorder in the near-surface region in a very closely spaced time and position manner than does a monomer impact. Moreover, B atoms in a breaking up cluster may have less probability of being channeled than a B monomer. This can be attributed to the higher degree of lattice disorder and different directions of B atom velocities after the breakup of the cluster. Since only those collisions that take place near the surface are effective in knocking atoms out of the material, diminished channeling that results in more collisions near the surface leads to a higher sputtering yield.

The sputtering yield of Si with B_{10} clusters obtained from MD simulations, however, is about 16 times larger than the experimental value (0.18 ± 0.05) measured with 5 keV decaborane ions, as described in section 6.1.2. The experimental value is however in a reasonable agreement with the empirical formula for sputtering yield of Si with monomer B ions. On the other hand, the simulated sputtering yield of Si with monomer B ions is 4.5 times smaller than that given by the empirical formula.

The difference between the monomer sputtering yields could be in part attributed to the fact that the Si target in the MD simulations was a perfect single crystal. In comparison, the empirical formula was derived from measurements on amorphous or polycrystalline materials. Examination of MD simulation results revealed strong channeling effects that resulted in deep implantation, deposition of significant fraction of ion energy deep under the surface and consequently low sputtering yield. Simulations were performed with B monomers impacting Si(001) surface at an angle: the Si target was first tilted along <110> axis by 7° from incident direction of the projectile and then rotated around <001> axis by 30°. The calculated sputtering yield was more than ten times larger that with normal impacts and close to the empirical value.

In MD simulations of cluster impacts, on the other hand, channeling played a significantly smaller role due to the factors described above. This, however, does not explain the much larger simulated sputtering yield than that measured on an amorphous Si surface. The reason may be due to the fact that the MD model did not realistically represent a real Si surface. In the simulation model, the lattice periodicity was extended to the top surface. Due to the existence of unsaturated dangling bonds, interactions between the surface atoms and the bulk may be weaker and in the simulations the surface atoms could be sputtered more easily than in reality. The "ideal" surface, as modeled by the MD simulation, does not exist even in free space (or ultra high vacuum) because of surface reconstruction. A real surface that exists usually in sputtering experiment is covered by a thin amorphous native oxide layer. The presence of the oxide also saturates Si bonds and changes surface properties.

In general, experimental sputtering yields are not accurately simulated using MD, as was pointed out by Smith *et al* [34]. The simulations reported here, however, elucidate the effects of cluster and monomer impacts in the material, showing evolution of crystal damage, channeling and a reasonable implantation depth.

CHAPTER 8

SUMMARY AND CONCLUSIONS

The effects of implantation of decaborane ions ($B_{10}H_x^+$) into Si have been studied in this work using both experimental and computer simulation methods. All implantation experiments were performed on a research ion implantation system in the Ion Beam and Thin Film Research Lab at NJIT. $B_{10}H_x^+$ ions and B^+ ions were generated by energetic electron impact of $B_{10}H_{14}$ vapor or BF_3 gas, magnetically mass analyzed, and implanted into Si samples. A new electron impact ionization source was built for this system. The design of the source structure was optimized by simulations of electric field and ion trajectories using program SIMION. Higher beam currents at lower gas pressures were achieved with the new ion source, which was also more robust and easier to handle as compared to the initial source. In order to obtain the ion beam profiles at any time during an experiment, a beam profiler was constructed and mounted before the sample chamber and was controlled by using a LabVIEW application program. The beam profiler has been extensively used for system adjustment, for finding optimum system operating conditions, and for process monitoring during the implantation.

The depth distributions of B and H in Si implanted with 12 keV $B_{10}H_x^+$ ions were studied using SIMS analysis. The results show that shallow junction depths can be achieved with decaborane implantation. A junction depth of 57 nm at 1.0×10^{18} cm^{-3} concentration level was measured after rapid thermal annealing. Analysis of H profiles reveal that the H concentration was greatly reduced after annealing. At the junction depth, the H concentration was the same as that in the unimplanted control region. Therefore, no significant effect on the device properties is expected from H atoms co-implanted with $B_{10}H_x^+$ ions.

Transient Enhanced Diffusion (TED) of B in Si implanted with $B_{10}H_x^+$ ions was studied and compared with TED after monomer B^+ implantation of equivalent energy and dose. Boron diffusivity enhancements for B marker layers in implanted samples were used to indicate the extent of TED. The results show that B implantation with $B_{10}H_x^+$ ions and B^+ ions of equivalent energy and dose lead to essentially the same extent of enhanced diffusion of the dopants. This is in agreement with an earlier study, which used a beam extracted from ionized decaborane vapor without ion mass analysis [27]. The decrease of TED with decreasing $B_{10}H_x^+$ ion energy was observed and explained by the proximity of implantation damage to the surface at lower ion energy.

Sputtering yields of amorphous Si by 12 keV, 9 keV and 5 keV $B_{10}H_x^+$ ions were obtained by sputtered depth measurements using Rutherford Backscattering Spectroscopy. The number of ejected Si atoms per incident B was 0.41 at 12 keV, 0.28 at 9 keV, and 0.18 at 5 keV. The experimental values agree well with values estimated for sputtering yields of Si by B^+ ions of equivalent energies using an empirical formula [71, 72]. The sputtering yield was found to increase with increasing $B_{10}H_x^+$ ion energy, which is in agreement with the general understanding of ion energy dependence of the sputtering yield in the studied energy regime. These findings suggest that sputtering by B atoms within the decaborane molecular ion is similar to sputtering by individual monomer B atoms.

The effects of $B_{10}H_x^+$ ion irradiation on the morphology of amorphous Si, crystalline Si, and metal film (Ta) surfaces have been investigated using AFM imaging and Power Spectral Density (PSD) analysis. The results clearly show that $B_{10}H_x^+$ ions smooth rather than roughen these surfaces. The results of PSD analysis reveal the reduction of surface features of $\geq 10\ \mu m^{-1}$ spatial frequency, which is in agreement with the qualitative observations on the AFM images.

Molecular dynamics simulations of 5 keV B_{10} cluster impacts and 0.5 keV B monomer impacts on Si crystal were performed. The results showed that the mean depth of B atoms in Si after B_{10} cluster impact is close to that after impact by B monomers with equivalent energy. The depth distributions of B after 5 keV B_{10} cluster impact is very similar to that for 0.5 keV B^+ ions simulated by TRIM. Simulations carried out to 4.6 ps time scales, i.e., much longer than the ion stopping times, showed that a crater was formed on the Si surface impacted by a B_{10} cluster. Enhanced sputtering of Si with B_{10} clusters as compared to that with B monomers was observed, which was not found in the experimental study. The difference may be explained by limitations of the simulation program in representing the surface of the Si target. This difference is thought to be due to the fact that the Si surface is not simulated realistically, since it is represented by the abrupt ending of the ideal diamond lattice.

The results for this work demonstrated that the effects of implantation of decaborane cluster ions in Si, including depth profiles and TED, were the same as in the case of monomer B^+ implantation. Moreover, the results of the sputtering yield measurements and surface morphology study show that decaborane cluster ions will not remove more of the substrate surface material than B^+ ion implants and will leave a smoothed substrate surface. All these results indicate that decaborane implantation is a technically viable alternative to ultra shallow B doping in future generation of CMOS devices.

REFERENCES

1. "The International Technology Roadmap for Semiconductors", *Semiconductor Industry Association*, 1999.

2. "The International Technology Roadmap for Semiconductors", *Semiconductor Industry Association*, 2001.

3. S. Wolf and R. N. Tauber, "*Silicon Processing for VLSI Era – 2nd Edition*", Vol. 1-Process Technologies, Lattice Press, pp.372-373, 2000.

4. M. A. Foad, A. J. Murrell, E. J. H Collart, G de Cock, D. Jennings, and M. I. Current, "Practical aspects of forming ultra-shallow junctions by sub-keV boron implants", *Mat. Res. Soc. Symp. Proc.* 568, pp.56, 1999.

5. S. N. Hong, G. A. Ruggles, J. J. Paulos, J. J. Wortman, and M. C. Ozturk, "Formation of ultrashallow p^+-n junctions by low-energy boron implantation using a modified ion implanter", *Appl. Phys. Lett.* 53, pp.1741-1743, 1988.

6. Applied Materials, "Applied Materials xR80S, Xr120S and xRLEAP 300mm ion implant System", http://www.appliedmaterials.com/products/assets/ion_implant (August 9, 2002).

7. Ref. 3, pp.405-406.

8. Axcelis Technologies, http://www.axcelis.com/products, (August 9, 2002).

9. E. C. Jones and E. Ishida, "Shallow junction doping technologies for ULSI", *Mat. Sci. and Eng.* R24, pp.37-51, 1998.

10. K-J. Kramer, S. Talwar, I. T. Lewis, J. E. Davison, K. A. Williams, K. A. Benton, and K. H. Weiner, "Resistless, area-selective ultrashallow P^+/N junction fabrication using projection gas immersion laser doping", *Appl. Phys. Lett.* 68, pp.2320, 1996.

11. M. C. Ozturk, N. Pesovic, I. Kang, J. Liu, H. Mo, and S. Gannavaram, "Ultra-shallow source/drain junctions for nanoscale CMOS using selective silicon-germanium technology", *Extended Abstracts of the Second International Workshop on Junction Technology 2001,* Japan Society of Applied Physics, pp.77-82, 2001.

12. T. Aoyama, K. Suzuki, H. Tashiro, Y. Toda, T. Yamazaki, K. Takasaki, and T. Ito, "Effect of fluorine on boron diffusion in thin silicon oxide and oxynitride", *J. Appl. Phys.* 77, pp.417-419, 1995.

13. R. Keller, "Ion Extraction", in *The Physics and Technology of Ion Sources*, edited by Ian G. Brown, Wiley-Interscience, pp.25, 1989.

14. M. Sosnowski, R. Gurudath, J. M. Poate, A. Mujsce, and D. C. Jacobson, "Decaborane as ion source material for boron implantation", *Mat. Res. Soc. Symp. Proc.* 568, pp.49-54, 1999.

15. K. Goto, J. Matsuo, T. Sugii, H. Minakata, I. Yamada, and T. Hisatsugu, "Novel shallow junction technology using decaborane ($B_{10}H_{14}$)", *IEDM-96 Tech. Digest,* pp.435-438, 1996.

16. K. Goto, J. Matsuo, Y. Tada, T. Tanaka, Y. Momiyama, T. Sugii, and I. Yamada, "A High Performance 50 nm PMOSFET using Decaborane ($B_{10}H_{14}$) Ion Implantation and 2-Step Activation Annealing Process", *IEDM-97 Tech. Digest,* pp.471-474, 1997.

17. M. Sosnowski, M. A. Albano, V. Babaram, R. Gurudath, J. M. Poate, and D. C. Jacobson, "Ionization and Mass Spectrometry of Decaborane for Shallow Implantation of Boron into Silicon", *J. Electrochem. Soc.* 147, pp.4329-4332, 2000.

18. M. A. Foad, R. Webb, R. Smith, J. Matsuo, A. Al-Bayati, T. Sheng-Wang, and T. Cullis, "Shallow junction formation by decaborane molecular ion implantation", *J. Vac. Sci. Technol.* B18, pp.445, 2000.

19. A. S. Perel, W. Krull, D. Hoglund, K. Jackson, and T. Horsky, "Decaborane Ion Implantation", in *Proceedings of the 2000 International Conference on Ion Implantation Technology*, pp.304–307, 2000

20. M. C. Vella, R. Tysinger, M. Reilly, and B. Brown, "Decaborane Ion Source Demonstration", in *Proceedings of the 2000 International Conference on Ion Implantation Technology*, pp.527-529, 2000.

21. Http://www.semiconductorfabtech.com/site-waferprocessing/news/2001/03/06.02 axcelis.shtml, (August 9, 2002).

22. T. Horsky, D. C. Jacobson, and W. Krull, "SemEquip Ion Source Performance", Presented at the 14th International Conference on Ion Implantation Technology, Taos, New Mexico, September 2002.

23. X. M. Wang, J. R. Liu, S. Lin, H. Chen, and W-K. Chu, "Extraction of Boron Cluster Ions from Source of Negative Ions by Cesium Sputtering", Presented at the 14th International Conference on Ion Implantation Technology, Taos, New Mexico, September 2002.

24. A. G. Dirks, P. H. L. Bancken, J. Politiek, N. E. B. Cowern, J. H. M. Snijders, J. G. M. Van Berkum, and M. A. Verheijen, "Low-energy implantations of decaborane ($B_{10}H_{14}$) ion clusters in silicon wafers", *1998 International Conference on Ion Implantation Technology Proceedings* vol. 2, pp.1167–1170, 1998.

25. D. Takeuchi, N. Shimada, J. Matsuo, and I. Yamada, "Shallow junction formation by polyatomic cluster ion implantation", *Nucl. Instr. and Meth. in Phys. Res.* B 121, pp.345-348, 1997.

26. N. Shimida, T. Aoki, J. Matsou, I. Yamada, K. Goto, T. Sugui, "Reduction of boron transient enhanced diffusion in silicon by low energy cluster ion implantation", *Materials Chemistry and Physics* 54, pp.80-83, 1998.

27. A. Agarwal, H-J. L. Gossmann, D. C. Jacobson, D. J. Eaglesman, M. Sosnowski, J. M. Poate, I. Yamada, J. Matsuo, and T. E. Haynes, "Transient enhanced diffusion from decaborane molecular ion implantation", *Appl. Phys. Lett.* 73, pp.2015-2017, 1998.

28. H-J. Gossmann, C. S. Rafferty, H. S. Luftman, F. C. Unterwald, and J. M. Poate, "Oxidation enhanced diffusion in Si B-doping superlattices and Si self-interstitial diffusivities", *Appl. Phys. Lett.* 63, pp.639-641, 1993.

29. M. D. Giles, "Transient Phosphorus Diffusion Below the Amorphization Threshold", *J. Electrochem. Soc.* 138, pp.1160-1165, 1991.

30. D. C. Jacobson, Konstantin Bourdelle, H-J. Gossmann, M. Sosnowski, M. A. Albano, V. Babaram, J. M. Poate, A. Agarwal, A. Perel, and T. Horsky, "Decaborane, an Alternative Approach to Ultra Low Energy Ion Implantation", in *Proceedings of the 2000 International Conference on Ion Implantation Technology*, pp.300–303, 2000.

31. Maria A. Albano, "Low Energy Implantation of Boron with Decaborane Ions", *PhD thesis, May 2001,* Interdisciplinary Program of Materials Science and Engineering, New Jersey Institute of Technology, Newark, NJ 07102.

32. J. F. Ziegler, J. P. Biersack, and V. Littmark, "*The Stopping and Ranges of Ions in Solids*", Pergamon, 1985.

33. M. Nastasi, J. W. Mayer, and J. K. Hirvonen, "*Ion-Solid Interactions: Fundamentals and Applications*", Cambridge University Press, pp.247-250, 1996.

34. R. Smith, M. Shaw, R. P. Webb, and M. A. Foad, "Ultra shallow junctions in Si using decaborane? A molecular dynamics simulation study", *J. Appl. Phys.* 83, pp.3148-3152, 1998.

35. Z. Insepov and I. Yamada, "Computer Simulation of Decaborane Implantation into Silicon, Annealing and Recrystallization of Silicon", *Mat. Res. Soc. Symp. Proc.* 669, J.4.7.1, 2001.

36. Z. Insepov, M. Sosnowski, and I. Yamada, "Modeling of Boron Implantation into Si with Decaborane Ions", *Mat. Res. Soc. Symp. Proc.* 669, J.4.19.1, 2001.

37. T. Aoki, J. Matsuo, and G. Takaoka, "Characterization of Damage Induced by Cluster Implantation", *Mat. Res. Soc. Symp. Proc.* 669, J.4.5.1, 2001.

38. M. Dobeli, P. W. Nebiker, R. Muhle, and M. Suter, "Sputtering and defect production by focused gold cluster ion beam irradiation of silicon", *Nucl. Instr. and Meth. in Phys. Res.* B 132, pp.571-577, 2002.

39. J. Liu, X. M. Wang, L. Shao, X. Lu, and W-K Chu, "Non-linear effect on radiation damage of silicon by cluster ion bombardment", *Nucl. Instr. and Meth. in Phys. Res.* B 190, pp.787-791, 2002.

40. J. Liu, X. M. Wang, L. Shao, H. Chen, and W-K Chu, "Non-linear effect of gold cluster ion induced damage in silicon", *Nucl. Instr. and Meth. in Phys. Res.* B 197, pp.101-106, 2002.

41. X. M. Wang, H. Chen, L. Shao, J. R. Liu, and W-K Chu, "Non-linear effect of copper cluster ions induced damage in silicon", *Nucl. Instr. and Meth. in Phys. Res.* B 196, pp.100-104, 2002.

42. T. Seki, T. Kaneko, D. Takeuchi, T. Aoki, J. Matsuo, Z. Insepov, I. Yamada, "STM observation of HOPG surfaces irradiated with Ar cluster ions", *Nucl. Instr. and Meth. in Phys. Res.* B 121, pp.498-502, 1997.

43. L. P. Allen, Z. Insepov, D. B. Fenner, C. Santeufemio, W. Brooks, K. S. Jones, and I. Yamada, "Craters on silicon surfaces created by gas cluster ion impacts", *J. Appl. Phys.* 92, pp.3671-3678, 2002.

44. J-H. Song and W-K. Choi, "Isolated cluster ion impact on solid surfaces HOPG, Si and Cu(TiO_2)/Si surfaces", *Nucl. Instr. and Meth. in Phys. Res.* B 190, pp.792-796, 2002.

45. I. Yamada, J. Matsuo, N. Toyoda, and A. Kirkpatrick, "Materials processing by gas cluster ion beams", *Mat. Sci. and Eng.* R34, pp.231-295, 2001.

46. D. Fathy, O. W. Holland, R. Liu, J. Wosik, and W. K. Chu, "Cluster ion beam smoothing of SiC and YBCO surfaces", *Mat. lett.* 44, pp.248-252, 2000.

47. A. J. Perry, S. J. Bull, A. Dommann, M. Michler, B. P. Wood, D. Rafaja, and J. N. Matossian, "The smoothness, hardness and stress in titanium nitride following argon gas cluster ion beam treatment", *Surface and Coatings Tech.* 140, pp.99-108, 2001.

48. L. P. Allen, D. B. Fenner, V. Difilippo, C. Santeufemio, E. Degenkolb, W. Brooks, M. Mack, and J. Hautala, "Substrate smoothing using gas cluster ion beam processing", *J. Electron. Mat.* 30, pp.829-833, 2001.

49. G. Gillen, "Fundamental Studies of Mechanisms in Molecular SIMS Using Cluster Projectiles", http://www.cstl.nist.gov/div837/division/techac/2000/clusterionbeamsims.htm (September 26, 2002).

50. N. Toyoda, J. Matsuo, T. Aoki, I. Yamada and D. B. Fenner, "Secondary ion mass spectrometry with gas cluster ion beams", *Nucl. Instr. and Meth. in Phys. Res.* B 190, pp.860-864, 2002.

51. R. Gurudath, " Development of an Ion Source for Implantation of Decaborane", *Masters Thesis, January 1999*, Department of Electric and Computer Engineering, New Jersey Institute of Technology, Newark, NJ 07102.

52. Case Technology, http://www.casetechnology.com/implanter/magnet.html, (October 31, 2002).

53. V. Babaram, "Experimental Ion Implantation System for Decaborane Ions", *Masters Thesis, May 2000,* Department of Electric and Computer Engineering, New Jersey Institute of Technology, Newark, NJ 07102.

54. Service and Operation Manual, Digital Current Integrator, Model 439, EG&G Inc., Oak Ridge, TN 37831.

55. D. A. Dahl, "SIMION 3D Version 6.0 User's Manual", BECHTEL BWXT IDAHO, LLC, 1996.

56. D. A. Dahl, "SIMION 3D Version 7.0 User's Manual", BECHTEL BWXT IDAHO, LLC, 2000.

57. Applied Motion Products, "2035 Step Motor Driver User's Manual", 2001.

58. R. H. Bishop, "LabVIEW Student Edition 6i", Printice Hall, 2001.

59. R. Nix, "An Introduction to Surface Chemistry" http://www.chem.qmw.ac.uk/surfaces/scc (February 28, 2003).

60. R. Fleming, "Secondary Ion Mass Spectrometry Theory Tutorial", http://www.eaglabs.com/cai/simstheo (February 25, 2003).

61. D. E. Sykes, "Dynamic secondary ion mass spectrometry", in *Methods of Surface Analysis*, edited by J. M. Walls, Cambridge University Press, pp.227-230, 1989.

62. W. A. Grant, "Rutherford back-scattering spectrometry", in *Methods of Surface Analysis*, edited by J. M. Walls, Cambridge University Press, pp.299-304, 1989.

63. Computer Graphic Services, "Rump: Welcome and Introduction" http://www.genplot.com/doc/RUMP/intro.htm#top (November 12, 2002).

64. Digital Instrument, http://www.di.com

65. A. Roud, "Atomic Force Microscopy", http://spm.phy.bris.ac.uk/techniques/AFM (January 15, 2003).

66. D. J. Eaglesham, P. A. Stolk, H-J. L. Gossmann, and J. M. Poate, "Implantation and transient B diffusion in Si: The source of the interstitials", *Appl. Phys. Lett.* 65, pp.2305-2307, 1994.

67. H-J. L. Gossmann, F. C. Unterwald, and H. S. Luftman, "Doping of Si thin films by low-temperature molecular beam epitaxy", *J. Appl. Phys.* 73, pp.8237-8241, 1993.

68. M. Sosnowski, M. A. Albano, C. Li, H-J. L. Gossmann, and D. C. Jacobson, "Transient Enhanced Diffusion of B in Si Implanted with Decaborane Cluster Ions", *J. Electrochem. Soc.* 149, pp.G474-G476, 2002.

69. Ref. 33, pp.220.

70. M. Thompson and L. Doolittle, Computer Code RUMP, Computer Graphic Services, Ithaca, NY, 1999.

71. Y. Yamamura, M. Natsunami, and N. Itoh, "Theoretical Studies on an Empirical Formula for Sputtering Yield at Normal Incidence", *Radiat. Eff.* 71, pp.65-73, 1983.

72. N. Matsunami, Y. Yamamura, Y. Itikawa, N. Itoh, Y. Kazumata, S. Miyagawa, K. Morita, R. Shimizu, and H. Tawara, "Energy dependence of the ion-induced sputtering yields of monoatomic solids", *Atomic Data and Nuclear Data Tables* 31, pp. 1-14, 1984.

73. J. Lindhard and M. Scharff, "Energy Dissipation by Ions in the keV Region", *Phys. Rev.* 124, pp.128, 1961.

74. P. Sigmund, "Theory of Sputtering. I. Sputtering Yield of Amorphous and Polycrystalline Targets", *Phys. Rev.* 184, pp.383-416, 1969.

75. T. Aoki, "Molecular Dynamics Simulation of Cluster Ion Impacts on Solid Surface", *PhD Thesis, January 2000,* Kyoto University, Kyoto, Japan. http://nishiki.kuee.kyoto-u.ac.jp/~t-aoki/papers/doctor/doctor.pdf

76. F. Ercolessi, "A molecular dynamics primer", http://www.sissa.it/furio (September 18, 2002).

77. F. H. Stillinger and T. A. Weber, " Computer simulation of local order in condensed phases of silicon", *Phys. Rev.* B 31, pp.5262-5271, 1985.

78. J. F. Ziegler, Computer Simulation Code SRIM/TRIM http://www.srim.org/SRIM/SRIM2003.htm (February 10, 2003)

79. Z. Insepov, M. Sosnowski, and I. Yamada, "Simulation of cluster impacts on silicon surface", *Nucl. Instr. and Meth. in Phys. Res.* B 127/128, pp.269-272, 1997.

80. X. Hu, K. Albe, and R. S. Averback "Molecular-dynamics simulations of energetic C_{60} impacts on (2×1) - (100) silicon", *J. Appl. Phys.* 88, pp.51, 2000.